Prediction of Low-Frequency Sound-Pressure Fields in Fitted Rooms for Active Noise Control

by

Gary Ka-Yue Chan

B.Sc., The University of British Columbia, 2005

A THESIS SUBMITTED IN THE PARTIAL FULFILMENT OF
THE REQUIREMENTS FOR THE DEGREE OF

MASTER OF APPLIED SCIENCE

in

The Faculty of Graduate Studies

(Mechanical Engineering)

THE UNIVERSITY OF BRITISH COLUMBIA

December 2007

Abstract

Low-frequency noise is a health concern for workers in industrial workshops; rooms of highly varying size and dimensions, usually containing obstacles (the ‘fittings’). Low-frequency noise can be generated from sources such as reciprocating or rotating machinery, or ventilation systems. As the exposure time to the noise lengthens, workers are increasingly at risk to harmful effects such as hearing loss, communication difficulty, personal discomfort, and even nausea from induced body vibrations. Passive methods of noise control, such as absorption or barriers, generally perform better at high frequencies, but are inadequate at low frequencies. A proposed solution is active noise control, which relies on destructive interference of sound waves to reduce noise levels. However, this depends on phase, and how it is affected when sound waves encounter diffracting obstacles. In addition, the geometrical configuration of the active-control system must be optimized, which can be done using a prediction model. Sound-prediction models can also estimate the decibel level of sound within a given room configuration created by a source and the attenuation provided by the control system. Therefore, it is of interest to develop a model that predicts sound propagation in fitted rooms with phase. In this thesis, sound-pressure fields were investigated in rooms containing parallelepiped obstacles at low frequencies for which the wavelength is comparable to the obstacle dimensions. The geometric theory of diffraction (GTD) was used to model edge diffraction from an obstacle and, thus, the pressure field in shadow regions. A ray-tracing prediction model was improved to consider both the amplitude and phase of sound fields, and also the effects of edge diffraction. To validate the prediction model, experiments were performed in an anechoic chamber where a source and diffracting objects were located. In collaboration with Dr Valeau at the Université de Poitiers in France, a second model based on the finite element method (FEM) was used to compare prediction results. It was found that the phase depends mostly on the direct unblocked source-to-receiver distance. The FEM and experimental results showed that occluding objects cause phase shifts. The implementation of first-order diffraction into the ray-tracing program was successful in predicting shadow zones, thus producing a better prediction of realistic sound fields in rooms with obstacles.

Table of Contents

List of Tables

List of Figures

Acknowledgements

Thank you to all who have supported me during my two years as a graduate student. Murray, your guidance and mentorship throughout my masters is very much appreciated. I have learned much about not only acoustics, but also the world of academia and general research principles. Vincent and Matthieu, thanks for your time and effort with running simulations of my experiments. At the time, the confirmation of our results was very encouraging to me, and reassured me in my own work.

To the acoustics group, each of you has enriched my experiences in your own individual way. Galen, I regarded you as a role model, and I have been privileged to watch your transition from the research lab to beyond. Katrina, thanks for all your advice and continuing support. Wonyoung, I still know my Korean name is 7H21! Alireza, thanks for introducing us to Iranian culture, and motivating me to exercise at the gym. Owen, we struggled through our masters together and I am fortunate to have a colleague like you to share triumphs and frustrations. Thanks for your scintillating stories on just about every facet of life. Gavin, thanks for lending me all those Pratchett books and injecting some excitement (and analysis) into what was previously just a simple game of chess. To all the summer students, you have all made the strange windowless room in the Library Processing Center a better place, by removing me from it and having lunch outside!

Thank you to my family for their unconditional support and patience with everything I have decided to do. I really *am* doing work; you just aren't here at UBC to see it.

Gary Chan

December, 2007

Chapter 1

Introduction

1.1 Noise in Industrial Workrooms

Low-frequency noise is a problem in industrial workshops. These are rooms of highly varying size and dimensions, often containing obstacles (the machines, etc., called the 'fittings') and many noise sources. The sources of low-frequency noise range from machinery with rotating parts, or reciprocating engines, to air flow in ventilation systems. Even walls and flat, panel surfaces contribute to the problem, as mechanical vibrations can be transferred to the walls through acoustical coupling, causing them to radiate sound. Usually the noise source cannot simply be turned off, for practical reasons, so the generated noise must be endured by workers, possibly during their entire work shifts. As the exposure time to loud noises increases, the employees are more likely to experience hearing problems, difficulty in verbal communication, nausea from body vibrations, and overall general stress and uneasiness. Typical exposure-control measures are hearing protectors and sound absorption. These are effective for high-frequency noise, but their performance at low frequencies is inadequate due to the long wavelengths of sound involved. A proposed solution is active noise control (ANC). This technique uses destructive interference to cancel sound. The control system must be optimized given the room geometry, by means of a prediction model. Moreover, a thorough understanding of phase in the presence of large objects is an essential prerequisite. Therefore, it is of interest to develop a prediction model that predicts the sound field in a room with obstacles, including phase.

This work extends previous research by Wong [1] in his study of low-frequency noise in fitted rooms. Wong measured and predicted the effect of fittings on the modal characteristics of the room in terms of sound-pressure level, but with minimal attention to phase and diffraction. It also continues work done on active noise control by Guo [2] and Li [3]. Guo developed an image-phase model to predict the effect of active noise control in empty rooms. Li used the model to optimize the physical configuration of the control system to produce the largest zones of strong local sound attenuation.

1.2 Room Acoustics

1.2.1 Wave Theory

Sound is a compression wave traveling through air and, as a form of wave energy that propagates through a medium, it must obey the general wave equation,

$$\nabla^2 p - \frac{1}{c^2}\frac{\partial^2 p}{\partial t^2} = 0, \tag{1.1}$$

where $\nabla^2 = \frac{\partial^2}{\partial x^2} + \frac{\partial^2}{\partial y^2} + \frac{\partial^2}{\partial z^2}$ is the three-dimensional Laplacian operator in Cartesian coordinates and c is the wave speed. The general solution to this equation is a traveling wave of the form $f(x - ct + \phi)$, where ϕ is the phase of the wave. This functional form is characterized by harmonic oscillations of any frequency in both time and space. Note that the wave speed and frequency f are related by the wavelength λ in the equation $c = \lambda f$. Using a separation of variables, the time component of Eq. (1.1) can be solved independently. It has the form $\exp(-i\omega t)$ where $\omega = 2\pi f$, the angular frequency, relates to the frequency of the oscillations. The time-independent wave equation can be rewritten as the Helmholtz equation,

$$\nabla^2 p + k^2 p = 0, \tag{1.2}$$

where $k = \omega / c = 2\pi / \lambda$ is the wave number. The solution to this equation depends on the boundary conditions. In room acoustics, the boundaries of the domain are surfaces which can have a range of acoustical properties. The simplest surface is an ideal surface that is completely rigid. Conceptually, this means that the particle velocity of an incident sound wave at the wall is zero, and the sound pressure at the wall is a maximum. Mathematically, if the surfaces in the x-direction are located at $x = 0$ and $x = L_x$, the boundary condition at those locations is,

$$\frac{dp}{dx} = 0 . \tag{1.3}$$

Similar boundary conditions can be written for the y and z directions. Then solving the Helmholtz equation yields,

$$p_{n_x,n_y,n_z}(x,y,z) = A\cos(\frac{n_x\pi}{L_x}x)\cos(\frac{n_y\pi}{L_y}y)\cos(\frac{n_z\pi}{L_z}z) , \tag{1.4}$$

where n_x, n_y, n_z are positive integers known as mode indices and A is a generic constant representing the amplitude of the mode. Note that the lowest mode in any direction is zero, indicating no sinusoidal fluctuations in that direction. The higher the mode, the more oscillations exist in the given direction. Eq. (1.4) is often rewritten with the wave number $k_x = n_x\pi / L_x$, and similarly in the y and z directions.

Under a different set of boundary conditions, the solution to the Helmholtz equation changes. Another typical boundary condition in acoustics is that in a free field (or within an anechoic chamber, where wall reflections are negligible). In this situation, a radiative boundary condition is used, which states that, as the radial distance r increases, sound pressure approaches zero. This is represented by,

$$\lim_{r\to\infty} p(r) = 0 . \tag{1.5}$$

In these circumstances, the solution can be derived using cylindrical or spherical coordinates. Assuming isotropic conditions, the solution in cylindrical coordinates is,

$$p_n(r) = A \cdot J_n(kr) + B \cdot Y_n(kr) , \tag{1.6}$$

where $J_n(kr)$ and $Y_n(kr)$ are Bessel functions, while A and B are amplitude constants. For large values of r, the asymptotic behaviour of the Bessel functions is $\frac{1}{\sqrt{r}}$, thus obeying the radiative boundary condition in Eq. (1.5). Similarly with a spherical coordinate system, the solution at large r is,

$$p(r) = \frac{A}{r}e^{ikr} \tag{1.7}$$

which decays as $\frac{1}{r}$ at large distances. The significance of Eqs. (1.6) and (1.7) is that the sound-pressure field for a cylindrical source and a spherical point source will decay as $\frac{1}{\sqrt{r}}$ and $\frac{1}{r}$, respectively. Refer to [4] for further details on the solutions to wave equations.

1.2.2 Acoustic Theory

In acoustics [5], the fluctuations of sound pressure may be detectable by our ears. The typical human ear is capable of hearing amplitudes as quiet as about 20 μPa, and frequencies between 20 Hz and 20 kHz. The unit of decibel (dB) is a logarithmic scale used to measure the amplitude of sound, relative to a reference level of $p_0 = 2\text{x}10^{-5}$ Pa. p_0 is the minimum pressure of sound that an average person can hear. A change of less than 1 dB is considered inaudible. Sound pressure in Pascals is converted to a sound-pressure level L_p in decibels by,

$$L_p = 20\log_{10}(\frac{p}{p_0}). \tag{1.8}$$

Note that the characteristic decays of the solutions to the wave equation in the previous section can be described in terms of decibels. Since L_p is proportional to the square of pressure, the spherical source decay of $\frac{1}{r}$ corresponds to a drop of -6 dB per doubling of distance (-6 dB/dd), while the cylindrical source decay of $\frac{1}{\sqrt{r}}$ corresponds to -3dB/dd.

Sound can also be quantified in terms of energy and power. For a spherical source, the pressure amplitude relates to source power by,

$$p^2(r) = \frac{\rho c W}{4\pi r^2} \tag{1.9}$$

where W is the source power in Watts and ρ is the density of the medium. Both energy and power are proportional to pressure squared. Sound power can be expressed in decibels by,

$$L_w = 10\log_{10}(\frac{W}{W_0}) \tag{1.10}$$

where $W_0 = 10^{-12}$ W is the reference power level. In the case of a radiating sound wave, L_w and L_p have the same decay rates because $20\log_{10}(p)$ and $10\log_{10}(p^2)$ are equivalent. Note that the boundary conditions introduced in the previous section can be expressed in terms of energy using the law of conservation of energy. Upon striking any surface, incident sound energy can be reflected, absorbed, or transmitted through the surface. The proportion of the incident energy that is reflected is quantified by the reflection coefficient R, and similarly for the absorption coefficient α and transmission coefficient τ. The sum of the three coefficients must be one in order to conserve energy. For an individual room, energy is assumed to remain within the room, so $\tau = 0$. The boundary condition in Eq. (1.3) can therefore be expressed as R=1 and $\alpha = 0$. In an anechoic chamber, which has highly absorptive surfaces to approximate free-field conditions, the boundary condition in Eq. (1.5) can be written as R=0 and α=1, as no energy reflects back into the room.

1.2.3 Scattered Field Theory

Thus far, we have only considered the sound field in an empty room. For a room containing obstacles (a “fitted” room) like many industrial workshops, the contents of the room scatter the sound field. When an incident wave impinges on an obstacle, it is scattered by means of reflection or diffraction. The scattered wave interferes with the incident wave, creating complex amplitude and phase behaviour, in all directions around the obstacle. The scattering characteristics depend on the wavelength, and the size and shape of the obstacle. The ratio of wavelength to obstacle size is an important factor. In the extreme case of a large obstruction, or at high frequency, most of the sound would be reflected. This is equivalent to a large wall with some reflection and absorption coefficient. On the other hand, if the scattering object is small, or at low frequency, most of the sound would diffraction around it. In general, the smaller the wavelength (or the higher the frequency), the more directional the scattering becomes. Figure 1.1 illustrates this concept by showing the theoretical scattering pattern due to a cylinder of radius a [6]. The focus of the work reported in this thesis lies between these extremes, where the ratio of wavelength-to-obstacle dimension is close to unity. This is because low-frequency industrial noise is typically below 250 Hz, which corresponds to wavelengths greater than 1 m. The fitting dimensions in a workroom vary widely, ranging from human-sized machinery of about one meter, to large fixtures that span several meters.

A scattering problem can be approached from two perspectives: deterministic and probabilistic. The deterministic method seeks to calculate the scattered field analytically. However, this restricts the problem to simple geometric cases, such as a straight edge, sphere or cylinder, where boundary conditions can be easily represented. There are several sources in the literature that derive analytical solutions for such cases (Interestingly, scattering from squares or cubes was not readily found.) [6-8]. One could also characterize edges exactly by their impulse responses, which is another well-studied approach [9-12]. Deterministic methods generally work well for a large, individual obstacle of simple shape. Otherwise, this approach becomes mathematically cumbersome and difficult to implement. For example, in Kawai's study of multiple edges [13], the scattered wave produced by each edge must be considered as an input parameter with respect to every other edge, to compute higher-order effects on the total field. The random-scattering perspective is therefore adopted for arrays of scatterers [14]. Here, the exact boundary conditions imposed by each and every obstacle are ignored. Instead, the obstacles are modeled as dimensionless points that scatter sound omni-directionally. Their locations are described by a mean free path that governs the probability of sound encountering an object. Similar probabilistic parameters include the 'fitting density' (inverse of the mean free path) [15], and the 'diffusion coefficient' [16]. This method can more easily handle a random array of relatively small scatterers with any intrinsic shape. However, for large structures with simple geometry where the theoretical solution is known, the randomness may cause inaccuracies in regions close to boundaries. Furthermore, this approach works best at mid and high frequencies, but not for low frequencies.

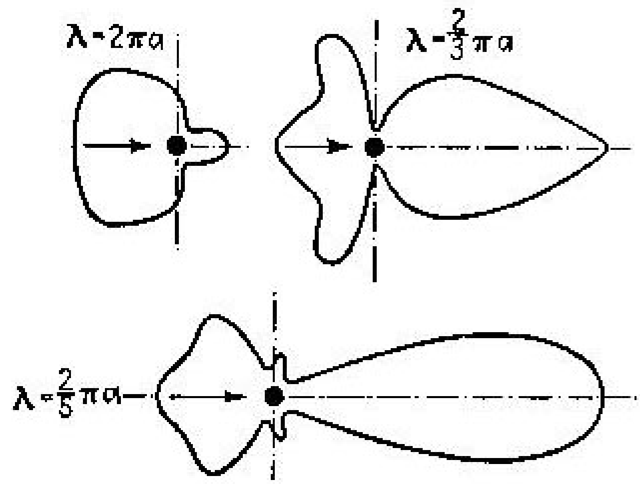

Figure 1.1 Polar diagrams of the scattered intensity pattern due to a cylinder of radius *a*.

1.3 Geometric Theory of Diffraction

A deterministic approach to the diffraction of electromagnetic waves around edges was introduced by Keller [17] in his Geometric Theory of Diffraction (GTD), and was extended to acoustic waves. Without diffraction, the domain in the presence of a wedge can be divided into three distinct regions, as seen in Figure 1.2. Region 1 contains the incident and reflected waves, Region 2 has only the incident wave, and Region 3 contains neither and is known as the shadow zone. The shadow region is unrealistic and contradicts real-life experience because sound diffracts into it; hence, a diffracted wave in that region was derived analytically by Keller. Briefly, Keller constructed diffracted rays by using laws of diffraction analogous to Snell's law of reflection (angle of incidence equal to angle of reflection in two homogeneous media) and Fermat's Principle (light traverses the path of least time between any two points). In the end, the diffracted ray has the following properties: its phase is proportional to its path length, and its amplitude depends on the incident field and a diffraction coefficient *D*. The diffraction coefficient is complex and depends on geometric factors such as the wedge angle, angle of incidence, angle of diffraction, source-to-wedge distance and wedge-to-receiver distance.

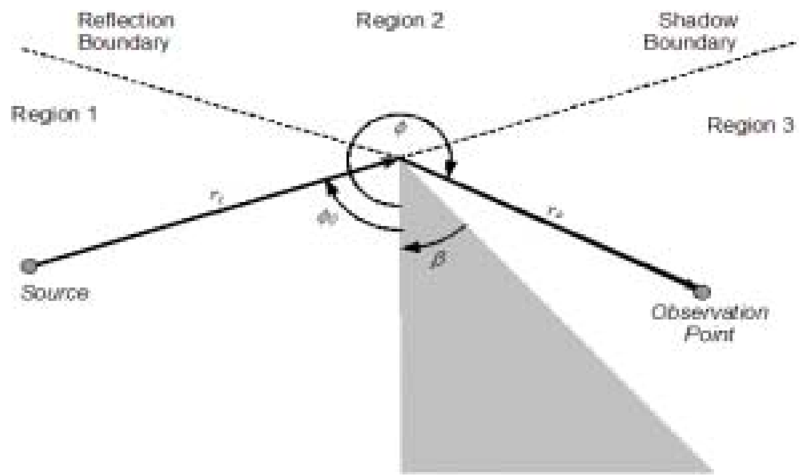

Figure 1.2 Three distinct regions that arise during diffraction.

Kouyoumjian and Pathak [18] noticed that the diffraction coefficient was ill-defined at the reflection and shadow boundaries. They developed a Uniform Geometric Theory of Diffraction, which modifies Keller's diffraction coefficient to address this issue. A full equation to compute the diffraction coefficient can be found in section 3.4.3, where the geometric parameters are pictured in Figure 3.4. Since then, this representation of diffraction has been successfully implemented in prediction models by Tsingos et al [19, 20], and Kawai [13]. Furthermore, it has been compared to the impulse-response approach to diffraction, with good results [12].

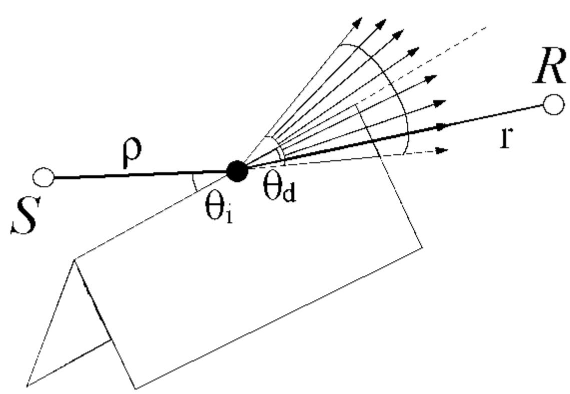

Figure 1.3 Edge diffraction gives rise to a cone of rays.

1.3.1 Edge Diffraction

The diffraction coefficient was used in this work, to diffract rays around edges into shadow regions. For an incident ray striking a single edge, a cone of diffracted rays emerges, as seen in Figure 1.3. The scattered wave has contributions in all directions, but our focus will be in the shadow region. Analytically, the shadow zone only contains a cylindrical wave [6]; hence the edge can be considered as a cylindrical sound source. This idea may be used as an alternative to the diffraction coefficient, if extra cylindrical sources are easily created in a prediction model. If not, it is still possible to approximate a cylindrical source by several point sources [12, 21], but an additional problem arises in determining their source strengths. This problem is nontrivial, and involves a known solution towards which the source amplitudes are tuned. In the present work, the diffraction coefficient was implemented.

1.4 Room-Prediction Models

There are several models that incorporate the theory discussed above, in order to predict sound in rooms. Each has its own way of handling the various features of a fitted room: sound-source characterization, wall reflection, modal behaviour (due to wave interference, from phase), and scattering from objects. The advantages and disadvantages of some of the relevant models will be outlined briefly in this section.

1.4.1 Sabine and Eyring Diffuse-Field Theory

The simplest model is the diffuse-field theory of Sabine / Eyring [5]. It calculates the steady-state sound field in a room, assuming the field is diffuse. The field is comprised of the direct-energy contribution from the sound source, and the reverberant energy due to the room. Wall reflections are accounted for by way of the total surface area *S,* and the average absorption coefficient of the walls, $\bar{\alpha}_d$. The Eyring expression for the sound-pressure level is,

$$L_p(r) = L_w + 10\log\left(\frac{Q}{4\pi r^2} + \frac{4(1-\bar{\alpha}_d)}{-\ln(1-\bar{\alpha}_d)\cdot S}\right) \tag{1.11}$$

where $L_w + 10\log(\frac{Q}{4\pi r^2})$ describes the direct contribution from a point source of sound power L_w with directivity factor Q, and $\frac{4(1-\bar{\alpha}_d)}{-\ln(1-\bar{\alpha}_d)\cdot S}$ is the room-effect term. For low average room absorption, the Sabine version is derived. This simple and explicit formula works best for empty, quasi-cubic rooms. For rectangular rooms with obstacles and non-uniform surface absorption, this formula does not perform well. Phase is also ignored, as the derivation is entirely in terms of energy. Refer to [22] for a discussion on using this room-prediction model.

1.4.2 Finite Element Method

Finite element methods (FEM) are numerical procedures that solve multi-dimensional differential equations in a domain with given boundary conditions. If a room is quasi-cubic with simple boundary conditions, this prediction method can give theoretically accurate results. However, once the room geometry becomes complex, and boundary conditions imposed by obstacles are introduced, the finite element method becomes increasingly difficult to implement. Also, the accuracy of the results depends on the mesh size and the frequency of the waves. The higher the frequency, the smaller the required mesh size to attain a sufficient number of nodes per wavelength. This imposes constraints on computer memory and runtime. In this research, the finite element method was used to solve the Helmholtz equation in a room with completely absorptive walls (free-field or radiative boundary conditions). Fittings were then added to the domain, which introduces reflective boundary conditions. Note that the FEM research was performed with the FEMLAB software, through the collaborative work of Dr. Vincent Valeau at the Université de Poitiers in France [23].

1.4.3 Ray Tracing

The focus of this work involves a ray-tracing model originally developed by Ondet and Barbry [24]. In this approach, a sound source emits spherical waves that are approximated by a large, user-defined number of infinitely thin rays. Each ray carries an equal portion of the total energy of the source. These rays are traced as they travel in straight lines through the room, reflecting from walls and obstacles as their trajectory dictates. Wall reflections may be specular (based on Snell's Law of Reflection) or diffuse (based on Lambert's Law of Diffuse Reflection). Scattering obstacles are modeled randomly via a fitting density, as explained previously in section 1.2.3, and an absorption coefficient. In particular, the probability of encountering an obstacle follows a Poisson distribution with the mean free path as its parameter. Energy is lost due to distance traveled, air absorption and surface reflections. When the ray crosses the location of the receiver, its energy is added, and the ray continues its trajectory. After a given number of reflections, the remaining energy of the ray is accumulated in a residual term, which is added to all receivers as a form of diffuse energy. Sound-pressure levels are calculated from the energy levels accumulated in each receiver cell after all rays are emitted.

The benefits of this method include the ability to model any polygonal room, randomized furnishings, and diffuse wall reflections. Some limitations of Ondet and Barbry's ray-tracing model are the lack of phase, and of deterministic diffraction for larger obstructions such as interior walls. The long runtime due to the tracking of a large number of rays and reflections is also a disadvantage. Also, the receiver cannot be a point; it must have some finite volume which the rays can intersect.

1.4.4 Other models

Beam tracing is another prediction model that runs in a similar fashion to ray tracing. Instead of tracing the trajectories of infinitely-thin rays, beams with non-zero cross-sectional area are tracked. The spherical wave emitted by the sound source is decomposed into, for example, triangular prisms that radiate outwards. The advantage here is that a point receiver is possible. However, a problem is that the beam widens as it travels, which leads to complications when the beam encounters a wall or obstacle. This may be solved by adaptive beam tracing. Note that Tsingos et al [20] implemented the diffraction coefficient into a beam-tracing model.

It was mentioned earlier that Guo [2] used an image-phase model to predict sound fields in empty rooms. This approach uses the method of images to model specular wall reflections. Fittings would be extremely difficult to implement, because each reflective surface would introduce additional image sources. Hybrid models exist that combine the method of images and diffuse-field theory [25]. Image sources are used to simulate the first few reflections, and then diffuse-field theory is used to account for the reverberant-room effect. In a sense, this is the same as ray tracing with a few reflections, but diffuse reflections and fittings will remain a challenge to implement with secondary sources.

Table 1.1 provides a summary of the room-prediction models. The ray-tracing and finite element models are used because of their ability to model diffracting obstacles within the room. We decided that improving the ray-tracing model to include phase and diffraction would be easier than implementing fittings and diffraction into the beam-tracing or image-phase model.

Table 1.1 Summary of room-prediction models.

Model	Conditions of applicability
Sabine / Eyring	Empty, quasi-cubic rooms with uniform surface absorption.
Finite Elements	Non-randomly fitted, quasi-cubic rooms with simple boundary conditions at low frequency.
Ray Tracing	Polygonal rooms with random or non-random fittings, specular or diffuse reflections, non-point receiver.
Beam Tracing	Empty polygonal rooms with specular or diffuse reflections.
Image-Phase	Empty parallelepiped rooms with specular surface reflections, with phase.

1.6 Research Objectives

With the theoretical background introduced, we now define the objectives of this research. The overall goal was to develop a method for predicting sound pressure in workshops with fittings. This involves investigating how diffracting obstacles influence the phase of the sound field, and improving an existing ray-tracing program to predict these effects. Our approach begins by first measuring the sound field around diffracting obstacles in an anechoic chamber. The detailed procedure and results of the experiments are discussed in Chapter 2. In the following chapter, the ray-tracing program is modified and tested extensively. Predictions of the experimental configurations are also presented in Chapter 3, along with data comparisons. Simulated sound fields in non-anechoic rooms are discussed in Chapter 4. Finally, Chapter 5 summarizes our findings and concludes the thesis.

Chapter 2

Anechoic-Chamber Experiment

2.1 Overview

In this chapter, the details of anechoic-chamber experiments are discussed. The goal is to perform simple tests that would reinforce our current understanding of phase, and investigate how it changes in the presence of fittings. We also aim to study diffraction in a systematic way. An anechoic chamber is used so that free-field conditions are simulated and room effects are negligible. Thus, any observed phenomena can be attributed to the fittings. Sound in rooms is discussed in Chapter 4. The next section describes the anechoic-chamber experimental setup, followed by specific test cases and their results.

2.2 Equipment Setup and Procedure

The dimensions of the anechoic chamber are 4.7 m by 4.3 m by 2.3 m. A picture of the anechoic chamber is seen in Figure 2.1. An acoustically transparent wire-mesh floor spans the chamber, on which objects may be placed. Experiments were done as close to the center of the chamber as possible, to minimize wall effects. A Stanford

Figure 2.1 Photograph of the anechoic chamber and the coordinate system.

SR770 signal generator was used to generate pure tones. Together with an Alesis RA-100 amplifier and a loudspeaker, the sound field was created in the test space. The diaphragm of the loudspeaker was 20 cm in diameter, mounted in a 30x20x30 cm^3 box. A Brüel and Kjær condenser microphone type 4135 was used to measure the sound field at various locations within the chamber. It was placed on the wire mesh, facing the loudspeaker. For configurations with a fixed coordinate system, tape measures were used to pinpoint the desired microphone location. The microphone was connected to a Nexus conditioning amplifier type 2690, predominantly for cable-adapting purposes. Finally the Nexus was connected to the second channel of an oscilloscope. Amplitude and phase data were taken from the oscilloscope display, in units of volts and seconds, respectively. Note that voltage was proportional to pressure, so Eqs (1.9) and (1.10) were applied to convert the voltages into pressure levels. The first channel of the oscilloscope was connected to the source of a reference signal, which was either the signal generator or a second (reference) microphone (via the Nexus) located directly in front of the speaker. The reference signal remained unchanged between test configurations, because the signal generator and speaker were not affected by the fittings. Phase was measured relative to the reference signal. In addition to the above setup, a stand-alone RION sound-level meter was used to measure the sound-pressure level in unweighted decibels. The apparatus were placed on one side of the anechoic chamber, where they had minimal influence on the sound field. Figure 2.2 shows a schematic diagram of the equipment.

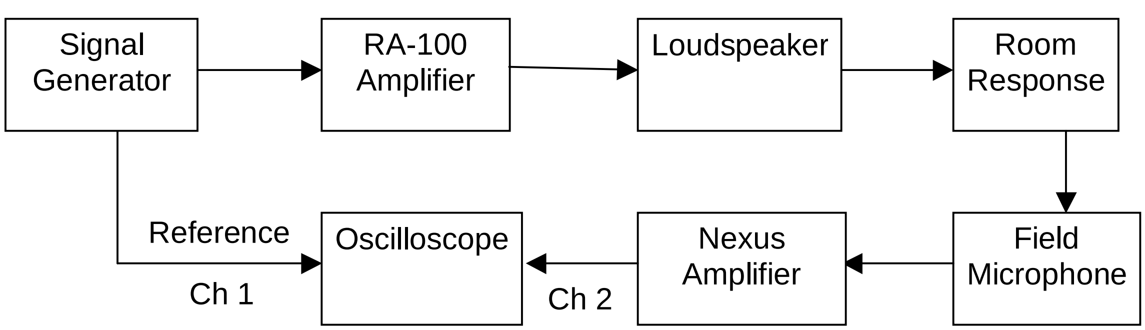

Figure 2.2 Equipment setup for anechoic-chamber experiments.

Obstacles were introduced to scatter the sound field. The first type of obstacle was a 6-mm-thick, rectangular wooden panel, with side lengths of 60 cm. It was used to create a reflecting plane, and also a diffracting edge. By placing several panels side by side, a wall with variable length was effectively created. The second type of object was a hollow, five-sided cube made from 10-mm-thick plywood, with a side length of 30 cm. Note that the surfaces of both these obstacles were varnished and considered to be highly reflective. With the dimensions of the obstacles in mind, a signal wavelength λ was chosen that is comparable in magnitude, so that the wavelength-to-obstacle size ratio would be close to unity. Hence a frequency of 1000 Hz (λ = 34.3 cm) was used. Note that, to relate the experiment to real industrial rooms, we have effectively designed a 1:n scale model. In scale models, all distances (including wavelength and obstacle dimension) can be considered as $1/n$ of their full size [26]. Conversely, frequency can be treated as n times higher. For n = 8, the side length of the cubic block becomes 2.4 m, which is not an unusual length for a workbench. Similarly the frequency scales to 125 Hz, which is clearly regarded as low-frequency sound.

Furthermore, some of the theoretically straightforward cases were simulated in the Matlab environment. Animations were created to mimic results observed on the oscilloscope. This was done because, otherwise, a large number of discrete data points would have been needed to fully capture the behaviour of the phase. A better approach was to do continuous experiments while watching the oscilloscope, and then reproduce the results with a Matlab animation. Afterwards, magnitude and phase were easily plotted from the Matlab variables.

2.3 Test Configurations

Several test configurations were considered, to analyze the behaviour of the sound field in both magnitude and phase. These included an empty anechoic chamber (free field), one reflecting plane, one diffracting edge, one cubic block, and multiple blocks. Each case will be described in the following subsections, and results shown.

2.3.1 Empty Anechoic Chamber

For the empty anechoic chamber (free-field) configuration, all blocks and panels were removed from the test area. The significance of this basic case is that when phase changes are determined in other room setups, the phase is compared to that of the empty room. Note that we were effectively characterizing the speaker's efficiency and directivity in this case. From a theoretical standpoint, sound pressure from a point source should decay as $1/r$, or SPL by –6 dB per doubling of distance in all directions. Furthermore, the phase should vary linearly with distance, since it is related to the time it takes for the wave to propagate to the microphone, and sound speed is constant. In fact, the slope of phase versus distance should be equal to the wave number $k = 2\pi / \lambda = 18.32$ rad/s. Measurements were recorded in 10-cm increments along two straight lines away from the speaker, at two different angles. Figure 2.3 shows the variation with distance of the measured sound field when the angle was 0^o, or along the axis directly in front of the speaker. It shows that the theoretical amplitude decay was indeed measured. The linearity of the phase measurements can be seen in Figure 2.3c. The slope was 17.46 rad/s, which is very similar to the theoretical value. When phase changes were later calculated, the actual phase values were normalized out. Similarly, the free-field case was remeasured at an angle of 18^o from the central axis of the speaker. Figure 2.4 summarizes the amplitude and phase results. The speaker radiated like a point source at both angles when the receiver was sufficiently far away. Near-field effects of the speaker may be the cause of the magnitude dips at the 18^o angle.

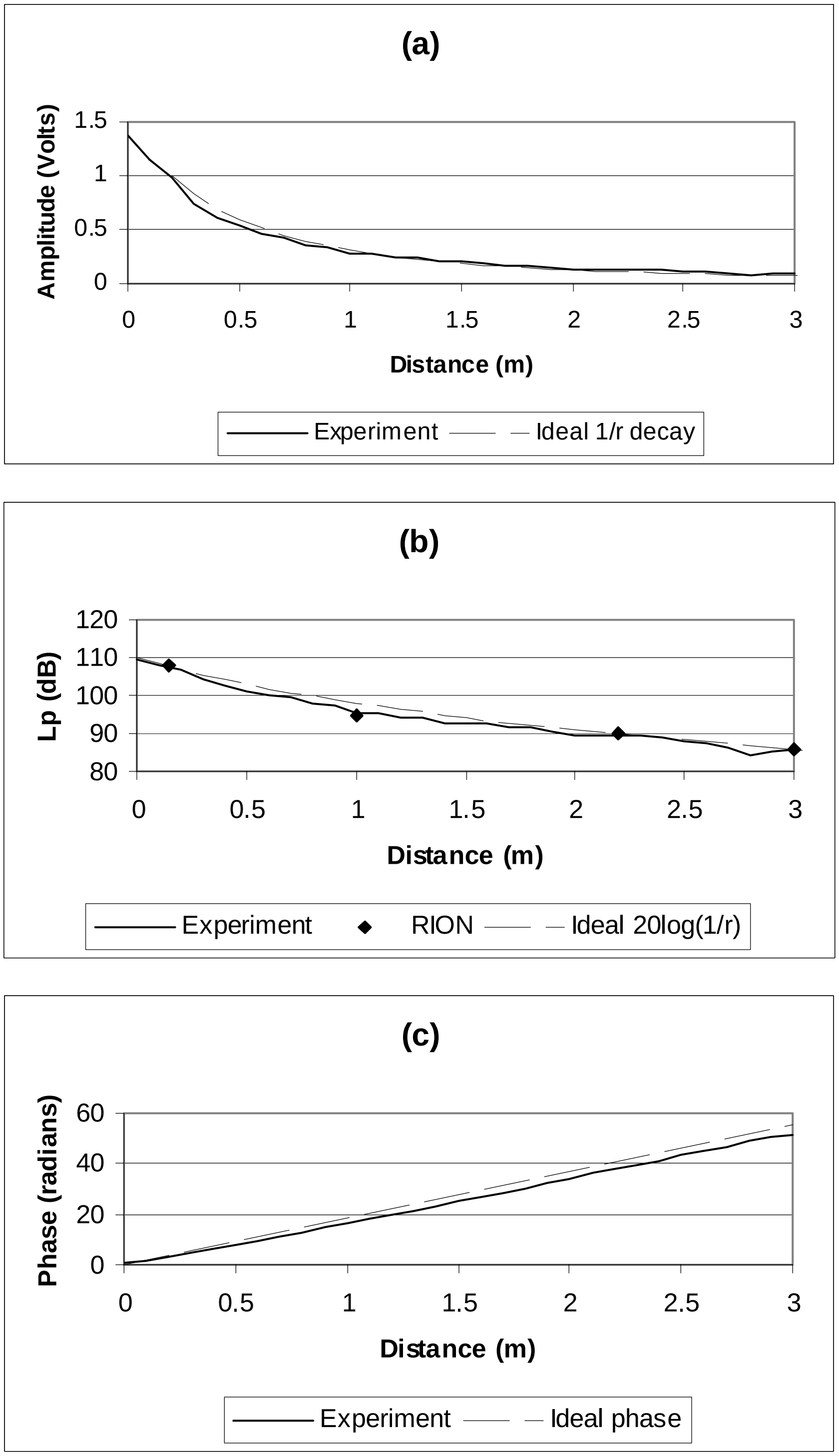

Figure 2.3 Free-field measurements along the 0^{o} axis in front of the speaker: (a) magnitude in volts, (b) magnitude in dB, (c) phase in radians.

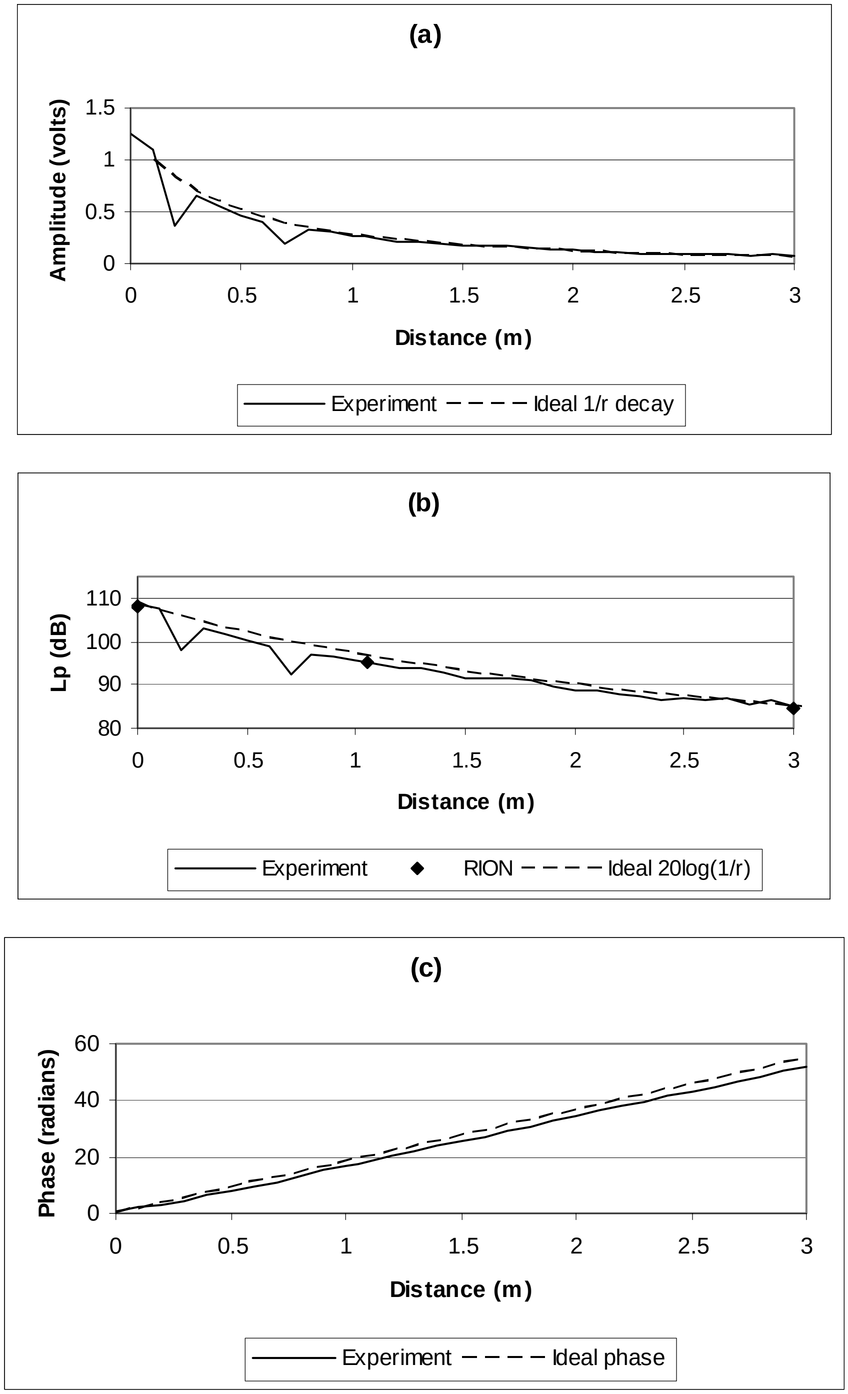

Figure 2.4 Free-field measurements along the 18^{o} axis from the front of the speaker: (a) magnitude in volts, (b) magnitude in dB, (c) phase in radians.

2.3.2 Reflecting Plane

In this test, one reflecting panel was introduced to the side of the 0^o axis, to create a reflected wave, in order to observe interference based on path-length differences. Instead of moving the field microphone, it was left stationary in front of the speaker, while the panel was gradually moved. In effect, this changed the distance that the reflected wave had to travel and, therefore, changed its phase at the microphone. Meanwhile the path length of the direct wave was kept constant. Therefore, when the direct and reflective waves combined at the microphone, we expected to see both constructive and destructive interference in the resultant wave. In terms of phase, the direct wave should have constant phase due to a constant path length, and the reflective wave should increase in phase. However, the expected behaviour of the phase of the resultant wave was unknown, hence the phase result of this test was of interest. Figure 2.5 displays predicted results that simulate those observed on the oscilloscope during the reflecting-plane experiment. Note that the *x*-axis on the figures was the path difference divided by the wavelength. The amplitude results in Figure 2.5a were as expected, since the direct wave stayed constant, the reflected wave decayed slightly due to the longer distance traveled, and the resultant wave alternately experienced constructive and destructive interference. In Figure 2.5b, the phases of the three waves are seen. The direct wave had constant phase and the reflected wave had linearly-varying phase. The phase of the resultant wave varied periodically. When the path difference was an integer multiple of the wavelength, constructive interference occurred, and the phase increased. At half-integer multiples of the wavelength, the waves interfered destructively, and the phase decreased sharply.

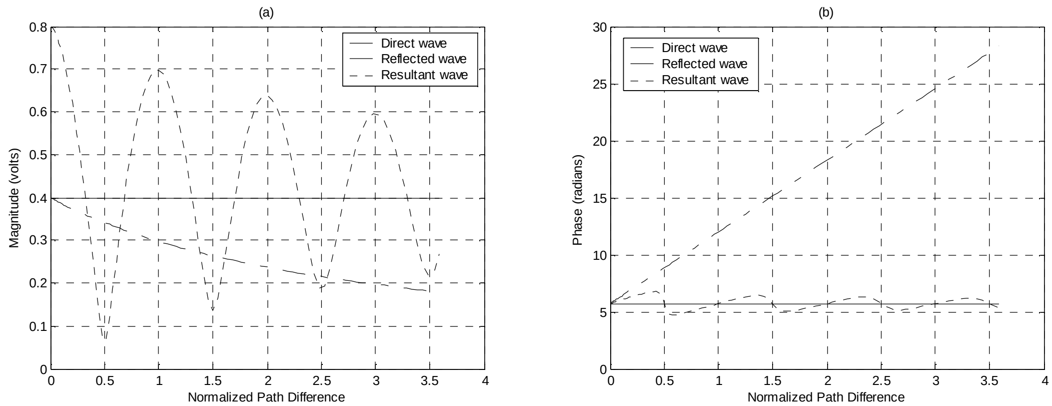

Figure 2.5 Measured sound pressures in an anechoic chamber with one reflecting plane: (a) magnitude and (b) phase.

2.3.3 One Edge

The next configuration tested was one diffracting edge in the anechoic chamber, to detect evidence of the cylindrical wave in the shadow zone, as theory suggests. A schematic of the setup can be seen in Figure 2.6 and photographs are included in Figure 2.7. Wooden panels were placed vertically in front of the speaker, forming a wall at a distance of 1.22 m away. The microphone locations were on the central axis of the speaker, behind the panels. Note that the edge of the wall protruded 15 cm from the central axis, so that all sound emitted from the diaphragm of the speaker had to diffract in order to reach the microphone. It was assumed that most of the sound reaching the microphone came from diffraction around the vertical edge at coordinates (1.22, 0.15). However, there were three other flanking paths to consider. The other vertical edge at coordinates (1.22, -1) was the farthest one and, therefore, was assumed to be negligible. The flanking path underneath the wall was significant and had to be dealt with. Otherwise, the path length to the microphone would have been equal to that around the edge of interest. Thus a reflecting ground was added between the source and the wall to block this path (Figure 2.7b). The contribution of the final flanking path, over the top of the wall, was also ignored. Since the panels were 60-cm tall, and the microphone was laid on the floor, the path length was more than a wavelength longer than the path of interest for short distances behind the wall. However, as the microphone was moved further behind the wall, this approximation broke down.

The locations of the maxima and minima were recorded, but not the absolute magnitudes. Phase was observed to vary linearly with distance; its direction did not reverse as in the reflecting-plane case. Data were predicted in Matlab, by treating the edge as a line source that radiates cylindrical waves into the region behind the panel. A complication arose here in picking the orders for the Bessel functions $J_n(kr)$ and $Y_n(kr)$. Through trial and error, we found that the inclusion of higher-order modes agreed better with our data. By summing the first three orders of $J_n(kr)$ and $Y_n(kr)$, we obtained the results seen in Figure 2.8. Notice that the minima and maxima of the cylindrical wave occur at roughly the same place as those observed. The difference could be because of experimental approximations discussed above, and also the choice of n in the Bessel functions.

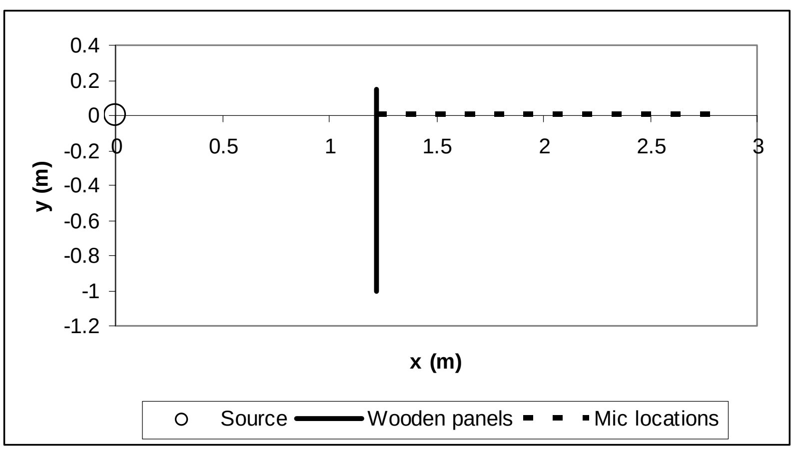

Figure 2.6 Schematic of the one-edge test, as seen from above.

(a) (b)

Figure 2.7 Photographs of the one-edge configuration from the view point of: (a) the receiver, and (b) the source.

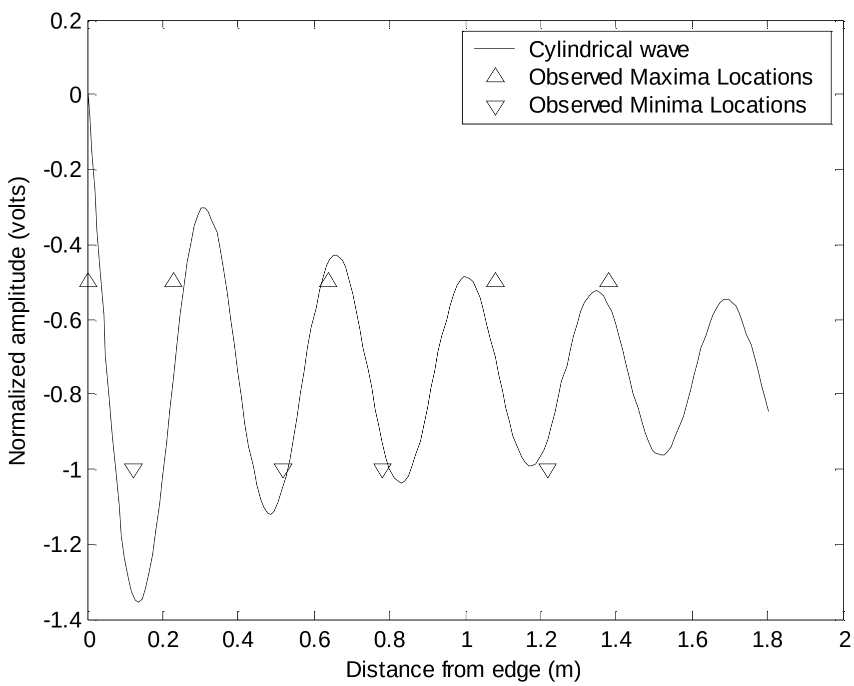

Figure 2.8 Measured and predicted pressure amplitudes behind one diffracting edge.

2.3.4 Edge Proximity

The configuration with one diffracting edge was revisited with the following goal: to determine how close to the edge a ray must strike for significant diffraction to occur. This has meaningful implications for implementing diffraction in the ray-tracing prediction model, because infinitesimally-thin rays have zero probability of arriving at a specific point in space. Hence, the edge tip must have some non-zero effective area around it, defined by some tolerance value. It is this value of tolerance that we seek. In the experiment, the same setup was used as for the one-edge test (Figure 2.6), except that additional panels were added or removed, and the microphone location was fixed. The idea was to extend or retract the edge from the central axis of the speaker, thus changing how close the sound strikes to the edge. We expected that, as the wall extended further off-axis, the path that the diffracting sound had to travel increases, so the measured sound-pressure level should decrease. We then compared the measured SPL to that when the diffracting path was blocked with a panel, to assess how much sound arrived via the edge..

However, some assumptions needed to be addressed. The first issue was the directionality of the speaker; this setup assumed that the speaker radiated predominately in front. As seen in the free-field results, this is not true; the loudspeaker radiated significant energy into other angles (for example, at an 18^{o} angle). Therefore, an additional panel was placed vertically next to the speaker to prevent sound from directly accessing the edge. The second approximation again involved the flanking paths. The vertical edge in the $-y$ region extended to the wall of the anechoic chamber and should be negligible. Flanking underneath the wall was dealt with as in the previous test. Flanking over the wall was more significant than before, since the path length around the edge of interest was increasing. Hence, another panel was placed above the microphone. Pictures of this experimental setup are included in Figure 2.9.

(a)

(b)

(c)

Figure 2.9 Pictures of the edge-proximity configuration: (a) before the edge is lengthened, (b) after the edge is lengthened, (c) with the flanking path over the wall blocked.

Figure 2.10 shows the SPL results for a lengthening edge at three frequencies: 500 Hz, 1 kHz and 2 kHz. Note that the normalized edge length on the horizontal axis refers to how far the edge protruded off-axis, divided by the wavelength. At 500 Hz, the sound did not decay uniformly until the edge lengthened by about half a wavelength, when the attenuation was -6 dB or more. Flanking was an issue at this frequency, and the additional panel above the receiver made a significant difference. The SPL at 1 kHz attenuated rather quickly, reaching the -6 dB mark when the edge lengthened by only a quarter of the wavelength. At 2 kHz, the sound decayed uniformly, albeit the slowest, reaching the -6 dB point at half a wavelength, as in the 500-Hz case. All three cases decayed as expected, and it appeared that diffraction occurring over half a wavelength away from the edge could be considered to make minor contributions.

The results of blocking the diffracting edge are displayed in Figure 2.11. The vertical axis is the difference between the sound-pressure levels measured before blocking the edge and after blocking the edge. In effect, this indicates the significance of the edge contribution. Note that the 500-Hz result was omitted because flanking was a problem. In some cases, blocking the edge with a panel decreased levels by 1-4 dB but, in other cases, it increased levels. At 1 kHz, the edge made a 10-dB difference until it lengthened by roughly half a wavelength, then levels began to drop off. The edge hardly made any difference to the sound field at 0.8λ. At 2 kHz, the edge diffraction became less significant more quickly, contributing over 10 dB at 0.4λ but nearly nothing at 0.6λ. This result makes sense, because higher frequencies of sound diffract less.

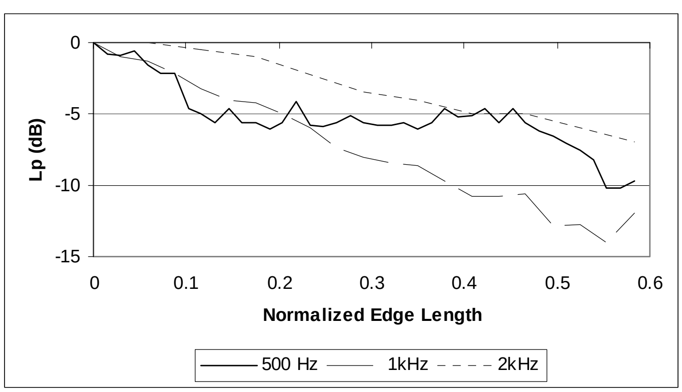

Figure 2.10 Normalized sound levels measured behind a lengthening edge.

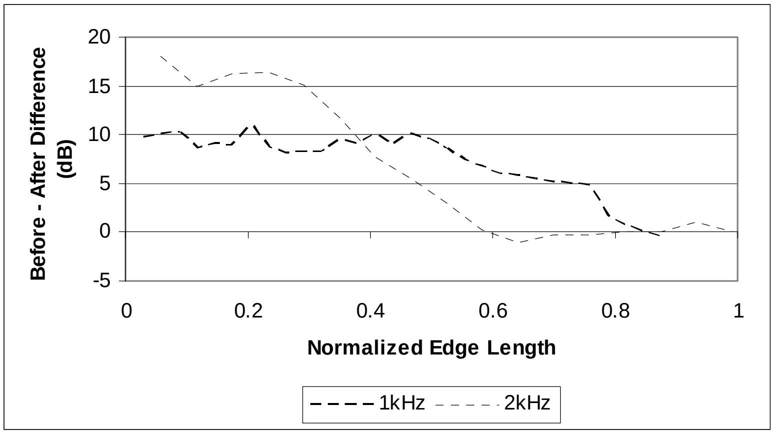

Figure 2.11 Difference in sound levels measured before and after blocking the edge.

Considering the results of Figure 2.10 and Figure 2.11, we selected a value for the edge-proximity tolerance, such that rays striking within this distance of an edge are considered close enough to the edge and are diffracted. It was clear that rays hitting more than 0.6λ away from the edge can be ignored for diffraction, while those within 0.4λ should be included. Hence we settled on the convenient ratio of 0.5λ as the value for the edge-proximity factor.

2.3.5 One Block

We next studied the configuration of a single cubic block at 1000 Hz. The block was placed such that its front face was 70 cm in front of the speaker, centered on the 0^o axis, and perpendicular to it. The sound field was explored on each face of the block, and detailed measurements were made in front of and behind the block along the central axis. In theory, the field in front of the block consisted of the direct wave from the speaker, and a reflected wave from the block. This was simulated in Matlab as verification. A photograph of the one-block configuration is shown in Figure 2.12.

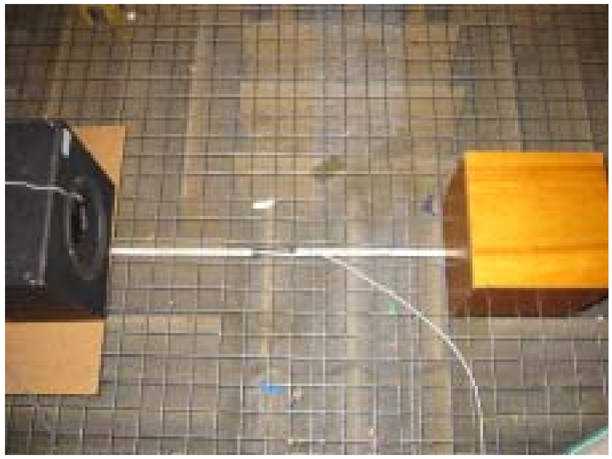

Figure 2.12 Photograph of the single-block configuration.

Qualitative results for the field on the block faces are as follows. For the front face of the block, the sound was loudest in the middle and decreased towards the edges. This was expected, since the source-to-receiver distance was shortest between the center of the loudspeaker diaphragm and the center of the front block face. Along the top and sides, similar behaviour was observed, due to symmetry. The sound decayed from front to back with linear phase. On the back face of the block, a local maximum was measured in the center of the face. Local maxima were also recorded at the back corners, while local minima were observed at the midpoints of the edges. However, all levels were much lower than at the front of the block. Clearly there were some complicated second-order diffraction effects occurring on the back face of the block.

Quantitative results for the region in front of the block are seen in Figure 2.9. For the amplitude results (Figure 2.13a), the interference pattern between the direct and reflected waves was evident in both measurement and prediction. Scaling the x-axis by the wavelength, the major dips at 43 cm and 60 cm correspond to $\lambda/4$ and $3\lambda/4$ away from the block (or $5\lambda/4$ and $7\lambda/4$ away from the source), respectively. Hence the path differences between the direct and reflected waves at those locations were $\lambda/2$, so the occurrence of destructive interference was not a surprise. Similarly, the peaks at 32 cm and 50 cm occurred when the path differences were 0 or λ, resulting in constructive interference. Note that the increase at 70 cm was due to the pressure-doubling boundary condition at the surface of the block. Phase behaved approximately linearly until 50 cm from the block, when it started to decrease. This was reminiscent of the reflecting-plane case (Figure 2.5b), because the phase decreased at half-integer multiples of λ. Thus, reflected waves due to block surfaces may cause phase changes in the nearby field. Agreement between experiment and prediction was surprisingly good for the amplitude and phase results in front of the block.

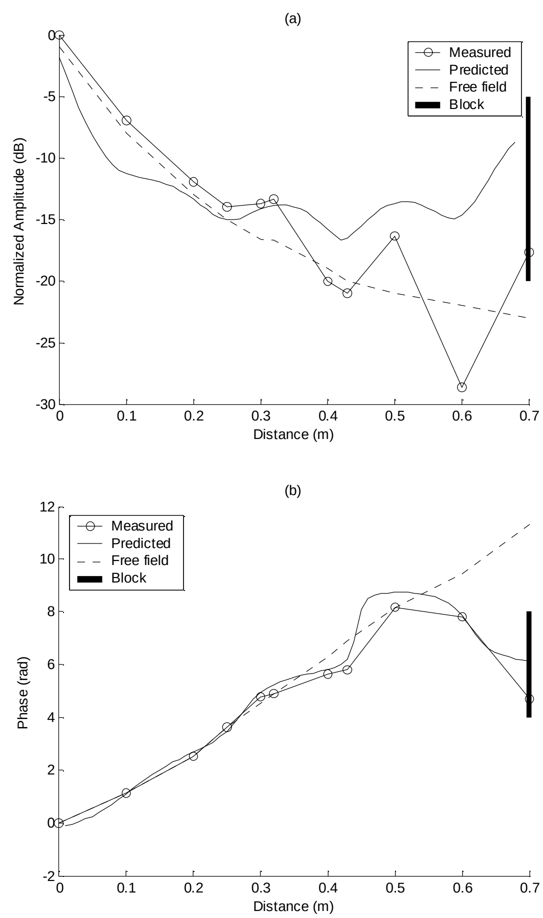

Figure 2.13 Measured and predicted sound field in front of a block in (a) amplitude and (b) phase.

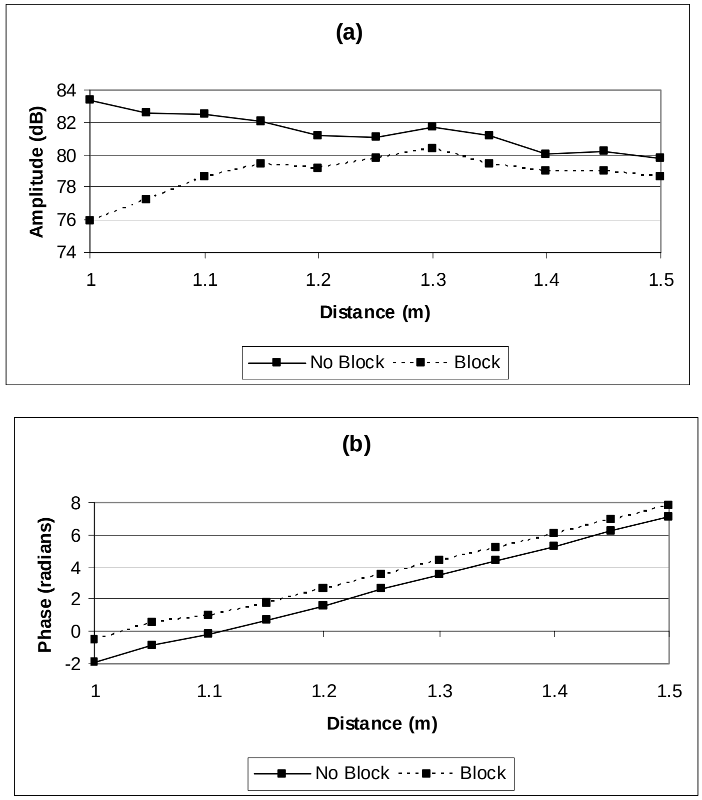

Figure 2.14 Measured sound field behind a block in (a) amplitude and (b) phase.

Behind the block, the measured amplitude data initially increased, and then it decayed with some oscillations, as seen in Figure 2.14a. Compared to the free field, the greatest difference occurred directly behind the block; at larger distances, the decay was similar, but lower in amplitude. As shown in Figure 2.14b, phase varied linearly despite the presence of the block, but it was consistently about one radian higher than the free-field phase. This was probably due to the longer path length caused by diffraction around the block; it also explains why the one-radian difference decreased as the distance grew. Matlab simulations did not agree with experimental results behind the block, however. It was conceivable that the field comprised a few edge sources or point sources, but our attempts failed to reproduce observed results.

2.3.6 Multiple Blocks

The final experiment was a case with multiple blocks, to investigate how an array of scatterers affect the phase of a sound field. We compared the sound pressure in the case with fittings to that in the free field, and investigated amplitude and phase changes. Note that there was an infinite number of ways to place multiple blocks in the anechoic chamber. Some parameters to consider were the number of blocks, the coordinate location of each block, the angular orientation of each block, the spacing between blocks, and the receiver locations among the blocks. Only a few constraints were imposed on the setup. One was to avoid near-field effects of the loudspeaker; thus, the nearest block could not be within 1 m of the source. The second restriction was that all blocks had to be within a 2x2 m^2 test area, to keep the block and microphone positions close to each other. In the end, nine cubes were placed randomly, with random rotations, and four series of receiver positions were selected. The receiver positions included along the central 0^o axis, along the $\pm 18^o$ directions (as in the empty anechoic chamber case), and along an arc of radius $\sqrt{5}$ m. A schematic of the configuration can be seen in Figure 2.15; pictures of the blocks are included in Figure 2.16. Keep in mind that, in the diagram, the block positions are approximate, and the random rotations are not depicted accurately. Note that a block crosses the measurement locations at about 2.5 m along the central axis, 2.1 m along the $+18^o$ direction, 2.0 m along the -18^o direction, and y=0.6 m along the arc. Note also that the $\pm 18^o$ directions were chosen to run from the loudspeaker to the back corners of the test area. The purpose of choosing a few directions other than along the central axis was to measure through a slightly different configuration of blocks, since the precise orientations of the blocks were different. Thus, it could also be thought of as rotating the room about the source. The reason for measuring along the $\sqrt{5}$ m arc was to fix the radial distance (hence the amplitude and phase in the free-field case), and investigate changes caused by the blocks. The measurements were done twice at 1 kHz to check the reproducibility of the results, and a third time at a lower frequency of 250 Hz. Only one set of 1 kHz results will be shown here, for the sake of brevity.

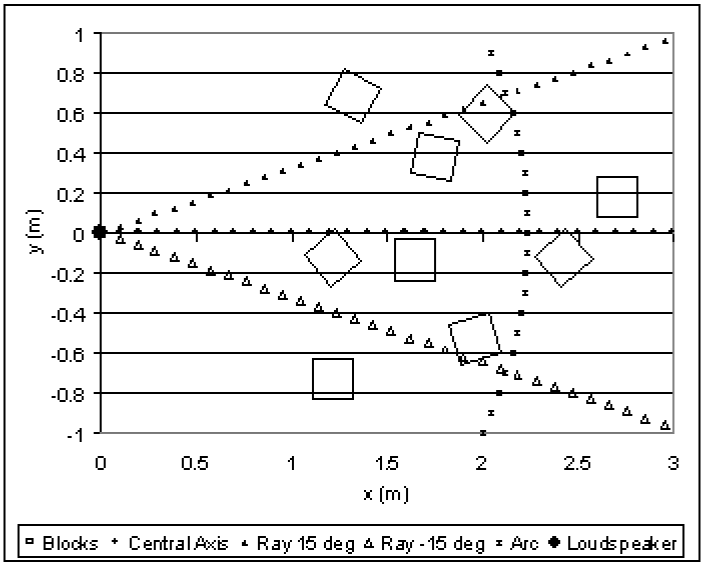

Figure 2.15 Approximate block and receiver locations for the multiple-block case.

Figure 2.16 Photographs of the multiple-block configuration as viewed from (a) a corner of the room, and (b) the source.

The amplitude and phase results for the central axis (0^o direction), $+18^o$ direction, -18^o direction, and the arc at 1 kHz are seen in Figures 2.17, 2.18, 2.19 and 2.20, respectively. Note that the phase is wrapped from $-\pi$ to π so that phase changes are not dwarfed by the scale of the axis. The three angular directions gave consistent amplitude results: L_p in the first 1.5 m of the test area could be louder or quieter than in the free-field by up to 5 dB, but L_p farther away was always less than that in the free field by 3-10 dB. This can be explained by a redistribution of energy due to the blocks. The blocks create reflections or back-scattering, which interferes with the incident field to cause the initial fluctuations. At the same time, this decreases the amount of sound reaching the longer-distance section of the test area, causing L_p to be lower. The three angular directions also had similar phase results. Agreement with free field was good except in the vicinity of a block. Minor phase changes were sometimes recorded in front of or beside a block, which could be explained by phase shifts caused by reflection, as seen previously in Figures 2.5b and 2.13b. The exact block orientation probably had a strong affect on these reflections. However, more significant phase changes were observed behind the blocks, which was in accordance with the results in the single-block case in section 2.3.5. Due to the added path length associated with diffraction around the block, the phase was roughly 2 rad higher than in the free-field case for the $\pm 18^o$ rays. The results along the arc were similar, despite the experimental error associated with difficulties in tracing a perfect arc. With most of the blocks positioned in front of the arc, the above argument explains the decrease in L_p. The observed phase was always greater than or equal to the free-field phase, which also agrees with previous statements about increases in path length. Similar results were found at 250 Hz, except that the phase changed by 0.5 rad. Note that symmetry was assumed in the free-field measurements, which is the reason why some of those results appear perfectly symmetrical.

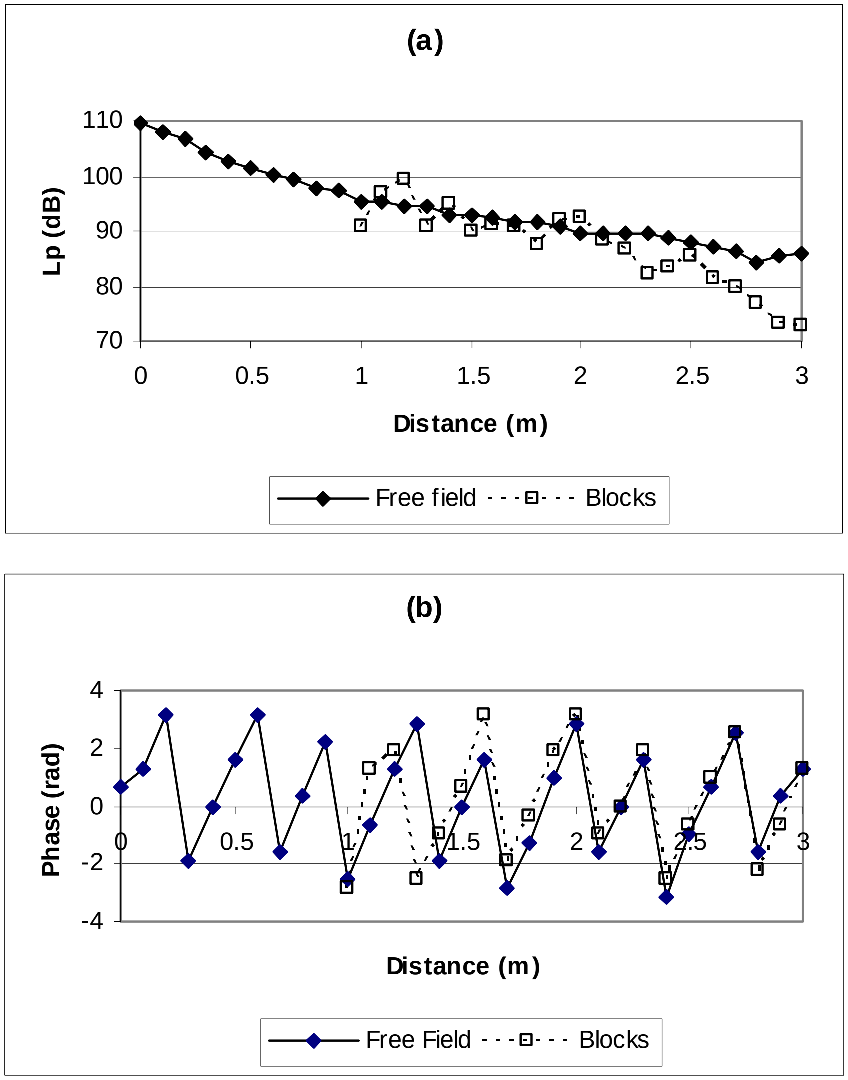

Figure 2.17 Measured pressures along the central axis for the multiple-block case: (a) sound-pressure level and (b) phase.

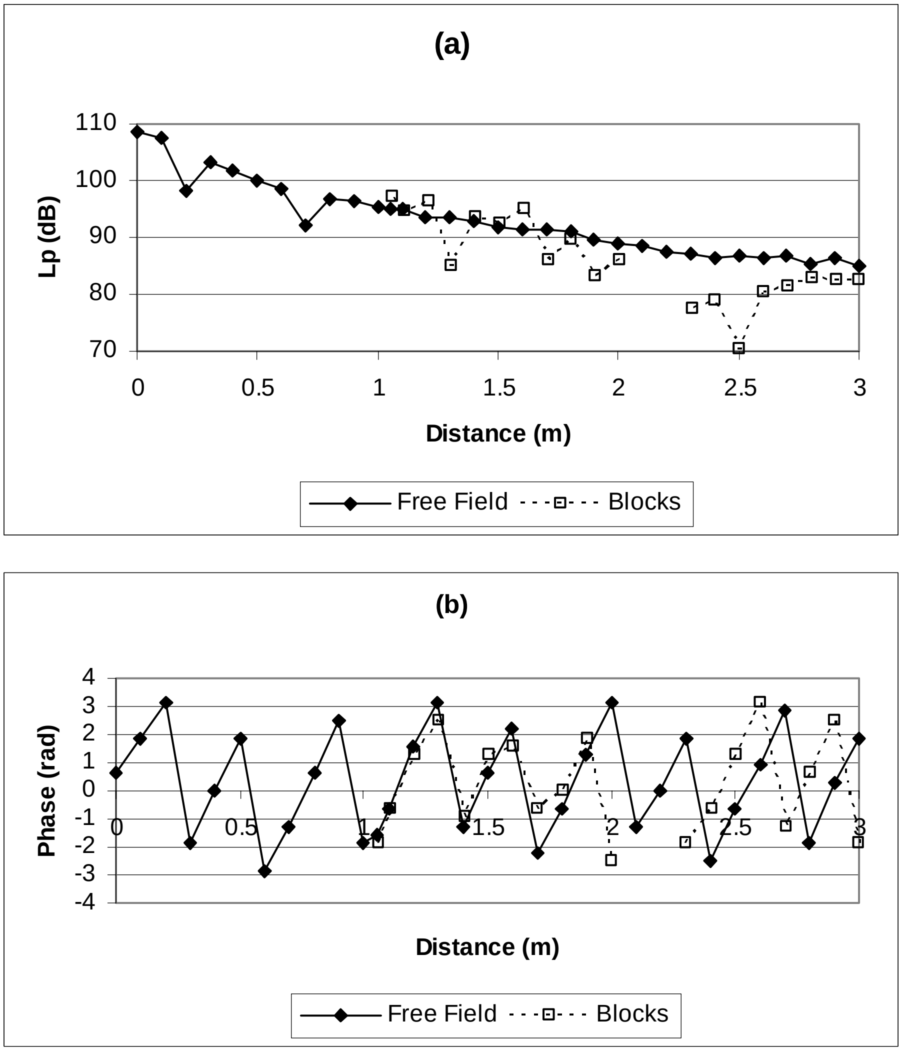

Figure 2.18 Measured pressures along the 18° direction for the multiple-block case: (a) sound-pressure level and (b) phase.

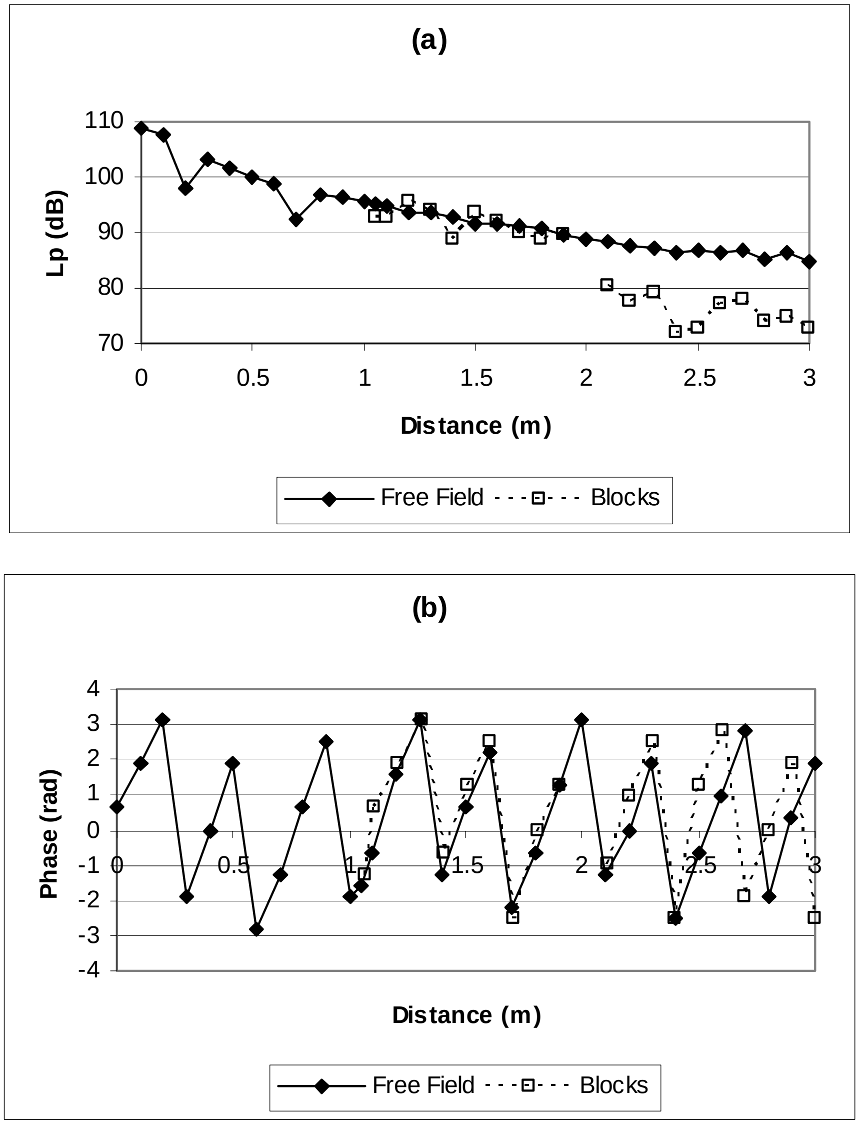

Figure 2.19 Measured pressures along the -18^{o} direction for the multiple-block case: (a) sound-pressure level and (b) phase.

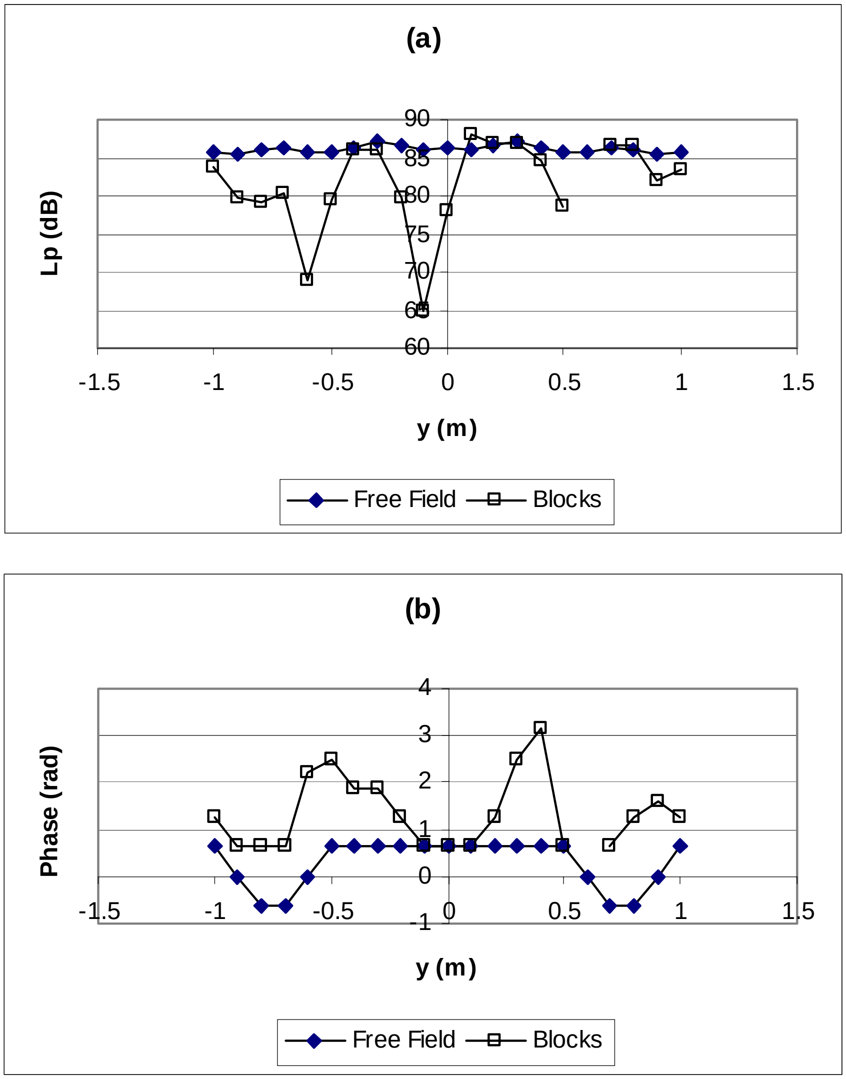

Figure 2.20 Measured pressures along the $r = \sqrt{5}$ m arc for the multiple-block case: (a) sound-pressure level and (b) phase.

2.4 Error Analysis

Experimental uncertainty in the results in this chapter will now be discussed. First, the loudspeaker was assumed to be a point source. Its precise location has some uncertainty, because the speaker box has finite volume, unlike a point source. Moreover, the diaphragm is a 20-cm disk. It was assumed that the location of the source was at the front face of the loudspeaker, at the center of the diaphragm. One could argue that the source was in fact in the middle of the loudspeaker, in which case all the source-to-receiver distances must be increased by 10 cm. The exact microphone location also has an uncertainty of a few centimeters, but no more than 3 cm. Tracing the $\sqrt{5}$ m arc in the multiple-block experiment gave the most difficulties in pinpointing the receiver locations. Also, the electronic devices may be a small source of uncertainty. Imperfections in the microphone, cable connections and various amplifiers could affect the magnitude and phase of the results. However, comparing the amplitude readings with the RION sound-level meter, the differences were usually within 0.5 dB, and at worst 1 dB. Reading the values from the oscilloscope had an error of 0.1 of a division. The time scale was set to 1 ms per division, which corresponds to a phase error of 0.63 rad. Hence, only phase changes of over 1.26 rad were considered significant, which was a conservative estimate. The voltage scale of the oscilloscope varied from 0.5 to 0.01 volts per division, so the error in measurement reading varied. However, this error was small compared to inaccuracies caused by low signal-to-noise ratios. When the receiver was over 2.5 m away, the signal was very weak and had to be amplified with the 0.01 volts per division setting. These measurements were highly sensitive to the surrounding conditions, including the movement of the experimenter. Weak signals were also distorted sometimes; the waveform was no longer sinusoidal. Hence, after converting to decibels, the amplitude data may have an uncertainty of less than 0.5 dB at close distances, and as much as 3 dB at the farthest distances.

2.5 Summary

In this chapter, we conducted several experiments to observe the sound-pressure field in the presence of obstacles. We verified that diffraction from edges can indeed be modeled by cylindrical sources. We found that sound incident on a wall within a distance of $\lambda/2$ from an edge should be considered for ray diffraction. Phase shifts were observed from interference between direct and reflected waves, and also from diffraction around the edges of a block. Both were explained by differences in path length caused by the blocks. In the following chapter, we turn our attention to sound-field prediction, with the goal of reproducing the characteristics observed in this chapter using a comprehensive model.

Chapter 3

Prediction

3.1 Overview

In the last chapter, we described anechoic-chamber measurements in which we observed phase and diffraction effects around single and multiple objects. We proceed in this chapter with the following objective: to upgrade a prediction model by implementing features that were observed in experiment. In the first chapter, we alluded to a ray-tracing model that would be our primary prediction model. Thus, we will begin this chapter by re-introducing the prediction model in its original state, followed by a lengthy discussion of the various changes and improvements that were made to the model. Next, we present simulations of the configurations studied in Chapter 2. At the end of this chapter, we will look briefly at another prediction model, the finite element method, and the results of its predictions.

3.2 Original Ray-Tracing Model

Recall from section 1.4.3 the description of the original Ondet and Barbry ray-tracing model - namely its mechanics, advantages and disadvantages. We will continue the description by presenting examples of predictions by the original ray-tracing program, and describe shortcomings that prompted our improvements. The first example consists of a source with a sound-power level of 100 dB, in the middle of an anechoic room, at 1000 Hz. This was chosen to demonstrate the accuracy of the model in predicting the ideal free-field decay from an omni-directional point source. The output – i.e. sound-pressure levels in 0.2 x 0.2 m^2 receiver cells located throughout the room - is shown in Table 3.1. The sound level is loudest in the cell containing the source and decays by about -6 dB/dd, as expected from a point source. Near the source, the decay rate appears slightly too fast. Also, the SPL in the receiver cell that contains the source is overestimated, due to how the ray-tracing algorithm handles such receiver cells. The second case shown consists of a 20 x 45 x 6 m^3 factory with a pitched roof. There are two noise sources at (5,5) and (5,15) with sound-power levels of 92 dB, and random fittings, at 1000 Hz. The fittings are defined by partitioning the domain into sub-volumes, and assigning a fitting density to each. In the region $0 < x < 20$ m and $z < 2$ m, the fitting density is 0.1 m^{-1}; in the region $z > 3$ m, the fitting density is 0.05 m^{-1}. Table 3.2 shows the predicted sound-pressure levels. The impact table (Table 3.2b) shows how often each wall and the obstacles are struck by rays. Notice that the SPL does not decay uniformly away from the sources, because of the fittings and reflections from the bounding walls. This time the sources are not inside receiver cells, so realistic levels are predicted in all cells.

A number of factors in the existing model provide incentive for an upgrade. Not only does the model lack phase and diffraction consideration, the model is also programmed in Fortran, which has its own drawbacks. For example, programming and debugging tools are limited, there are no visualization of results except text, as seen in Tables 3.1 and 3.2, and workspace variables are inaccessible and must be explicitly printed out to be retrieved. Also, the Fortran input file is nontrivial to prepare because the correct number of blank spaces and rows of zeros are required in some cases. In addition to these inconveniences, some serious technical problems arose that stifled our new work. One such case was when the program refused to compile, presumably because it was too long or took too much memory space. In a second case, variables would suddenly reset to zero partway through the simulation, for no apparent reason. With no clear solution to these technicalities, we opted to translate the entire code from Fortran into Matlab, which shall be discussed in the next section.

Table 3.1 Predicted SPL (dB) results from the original ray-tracing model, for an anechoic room with a point source at (2.0, 2.0).

x/y (m)	0.2	0.4	0.6	0.8	1.0	1.2	1.4	1.6	1.8	2.0	2.2	2.4	2.6	2.8	3.0	3.2	3.4	3.6	3.8
0.2	81	82	82	82	83	83	83	84	84	84	83	84	83	83	83	82	82	82	81
0.4	81	82	83	83	84	84	84	85	85	85	85	85	84	84	83	83	83	82	82
0.6	82	83	83	84	84	85	85	86	86	86	86	86	85	85	84	84	83	83	82
0.8	83	84	84	84	85	86	86	87	87	87	87	87	86	86	85	85	84	83	82
1.0	83	84	85	85	86	87	88	88	89	89	89	88	87	87	86	85	84	83	82
1.2	83	84	85	86	87	88	89	90	91	91	91	90	89	88	87	86	85	84	83
1.4	83	84	85	86	88	89	90	92	93	93	93	92	91	89	88	86	85	84	84
1.6	84	85	86	87	88	90	92	94	96	97	96	94	92	90	88	87	86	85	84
1.8	84	85	86	87	89	91	93	96	100	103	100	96	93	91	89	87	86	85	84
2.0	84	85	86	88	89	91	94	97	103	112	103	97	93	91	89	88	86	85	84
2.2	83	85	86	87	89	91	93	96	100	103	100	96	93	91	89	87	86	85	83
2.4	84	85	86	87	88	90	92	94	96	97	96	94	92	90	89	87	86	85	84
2.6	83	84	85	87	88	89	91	92	93	94	93	92	91	89	87	86	85	85	84
2.8	83	84	85	86	87	88	89	90	91	91	91	90	89	88	87	85	84	84	83
3.0	82	83	85	85	86	87	88	89	89	89	89	88	88	87	86	86	84	83	82
3.2	83	83	84	85	85	86	87	87	87	87	87	87	87	86	85	85	84	83	82
3.4	82	83	84	84	84	85	86	86	86	86	86	86	85	85	84	84	83	83	82
3.6	81	83	83	83	84	84	85	85	85	85	85	85	85	84	84	83	83	82	82
3.8	81	82	82	83	83	84	84	84	84	84	84	84	84	83	83	82	82	81	81

Table 3.2a Predicted SPL (dB) results from the original ray-tracing model for a factory.

x/y (m)	1	3	5	7	9	11	13	15	17	19
1	79.4	79.8	79.9	79.8	79.5	79.5	79.7	79.7	79.9	79.6
2	79.5	79.8	80.3	80	79.6	79.6	79.7	80	79.6	79.7
3	79.5	80.2	80.7	80.4	79.6	79.8	79.9	80.9	80.5	79.8
4	79.6	80.7	83	81.1	79.5	79.4	80.5	83.2	80.7	79.6
5	79.4	80.9	88.3	81.1	79.7	79.8	80.8	88.4	80.7	79.6
6	79.7	80.5	82.8	80.5	79.3	79.5	80.5	83	80.2	79.4
7	79.4	79.7	80.4	79.8	78.9	79.4	79.8	80.7	79.8	79
8	79.2	79.3	79.6	79.2	79	79	79.3	79.4	79.6	78.8
9	78.9	79.1	78.9	78.8	78.6	79.1	79	78.9	79	78.9
10	78.3	78.8	78.6	78.7	78.3	78.9	78.5	78.6	78.6	78.8
11	78.1	78.4	78.6	78.3	78.5	78.3	78.5	78.8	78.5	78.8
12	78.1	78.1	78.4	77.9	78.5	78.2	78.3	78.1	78.5	78.3
13	78.1	77.8	78.3	78.1	78.2	77.9	78.2	78.2	78.5	78.1
14	77.5	77.8	77.7	78	77.9	77.9	77.5	78.1	77.9	78.3
15	77.8	77.8	78	77.9	78	77.9	77.7	77.7	77.8	77.9
16	77.4	77.5	77.8	78.3	77.9	77.7	77.7	77.4	78.1	77.4
17	77.7	77.1	77.1	78	77.9	77.7	77.3	77.4	77.4	77.5
18	77.2	77.2	77.5	77.8	77.6	77.6	77.6	77.6	77.1	77
19	76.9	77.2	77.7	77.7	78	78.2	77.7	77.7	76.9	76.8
20	76.8	76.8	76.7	76.9	76.9	76.9	76.8	77.2	76.6	76.2
21	76.3	75.9	75.4	75.5	74.7	75.2	75.5	75.6	76.1	76
22	76.5	76.3	75.9	75.6	75.3	75.8	75.8	75.9	76.5	76.3
23	76.6	76.4	75.9	75.9	75.6	75.9	75.9	76.2	76.2	76
24	76.2	76.1	75.9	75.9	75.7	76.1	76	76.3	75.9	76
25	75.9	76	75.9	76.4	75.5	75.9	75.8	76.2	75.6	76.2
26	75.8	75.6	75.9	75.6	75.7	75.9	75.8	75.6	75.9	76
27	75.9	75.6	75.9	75.8	76.2	75.8	76	75.8	76.1	76.1
28	75.5	75.7	75.5	76.2	75.6	75.6	75.9	75.6	75.8	75.5
29	75.7	75.9	75.8	76.1	75.8	75.7	76	76	76.3	75.4
30	75.7	75.8	76	75.9	75.4	75.7	75.8	75.7	75.9	75.8
31	75.7	75.6	75.7	75.8	75.8	75.7	75.7	75.9	75.6	75.1
32	75.7	75.4	75.5	75.5	75.7	75.7	75.8	76.4	75.6	75.4
33	75.7	75.9	75.8	75.4	75.6	75.9	75.8	75.7	75.5	75.4
34	75.6	75.7	75.8	75.5	75.4	75.8	75.7	75.5	75.4	75.5
35	75.4	75.8	75.7	75.9	75.2	76	75.6	75.8	75.7	75.3
36	75.2	75.9	75.4	75.9	75.3	76	75.5	75.6	75.9	75.4
37	75.4	75.9	75.7	75.8	75.3	75.9	75.8	75.1	76	75.6
38	75.4	75.5	76	75.4	75.6	75.8	75.9	75.6	75.9	75.8
39	75.5	75.6	75.8	75.7	75.9	75.8	75.9	75.4	75.6	75.7
40	75.5	75.8	76.1	75.9	76	75.6	75.9	75.7	75.5	75.6
41	75.5	75.8	75.6	75.5	75.8	75.9	75.5	75.8	75.5	75.9
42	75.5	75.8	75.5	75.6	75.3	75.8	75.7	75.5	75.5	75.9
43	75.3	75.1	75.7	75.7	75.5	75.8	75.6	75.6	75.8	75.4
44	75.2	75.5	75.8	75.7	75.5	75.6	75.6	75.4	75.4	75.7

Table 3.2b Impact table for the factory.

Wall number	1st reflection	2nd reflection	3rd reflection	All reflections
1	26	82	123	10142
2	359	564	691	27801
3	304	546	631	28011
4	363	532	629	28142
5	346	590	643	27940
6	412	605	619	31103
7	390	615	619	31095
8	791	1209	1066	22398
9	1	33	79	15451
10	2639	2026	2295	105222
Obstacles	4369	3198	2605	72695

3.2.1 Matlab Ray-Tracing Model

The first improvement to the original ray-tracing program was simply a translation into Matlab. This addressed all the issues mentioned in the preceding section. The code was essentially copied line for line, with the exception of the “Go to line” command which was handled with a “while” loop. Hence we did not expect any major changes from the Fortran model. For verification, the two sample results (Tables 3.1 and 3.2) were rerun with the Matlab version of the model; the results are tabulated in Tables 3.3 and 3.4. Comparing the numbers, the empty anechoic room results are almost identical to the Fortran results, to the nearest decibel. The slight differences can be explained by the randomness of the ray-tracing algorithm; the direction of each ray is generated randomly. The sound levels for the factory results are about 1.5 dB lower, and the obstacles are hit more often, according to the impact table. The extra obstacle impacts likely caused the lower SPL’s, because energy is absorbed with every impact. It is not known how this change came about in the translation but, fortunately, our work on deterministic diffraction does not involve much use of random fittings. One downside to the upgrade is that the runtime lengthened substantially, because Matlab has far more functions loaded in the background than a command prompt running the Fortran model.

All in all, the Matlab version of the ray-tracing model increases the model's ease-of-use without many disadvantages, or introducing any new major problems.

Table 3.3 Matlab ray-tracing model results for SPL (dB) in an empty anechoic room with a point source at (2.0, 2.0).

x/y (m)	0.2	0.4	0.6	0.8	1.0	1.2	1.4	1.6	1.8	2.0	2.2	2.4	2.6	2.8	3.0	3.2	3.4	3.6	3.8
0.2	81	82	82	82	83	83	83	83	84	84	84	84	83	83	83	82	82	81	81
0.4	81	82	83	83	84	84	84	84	85	85	85	85	84	84	83	83	83	82	82
0.6	82	82	83	84	84	85	86	86	86	86	86	86	85	85	84	84	83	83	82
0.8	83	83	84	85	85	86	87	87	87	87	87	87	86	86	85	84	84	83	82
1.0	83	84	84	85	86	87	88	88	89	89	89	88	88	87	86	85	84	83	83
1.2	83	84	85	86	87	88	89	90	91	91	91	90	89	88	87	86	85	84	83
1.4	83	84	85	87	88	89	90	92	93	93	93	92	90	89	88	86	85	84	84
1.6	84	85	86	87	88	90	92	94	96	97	96	94	92	90	88	87	86	85	84
1.8	84	85	86	87	89	91	93	96	100	103	100	96	93	91	89	87	86	85	84
2.0	84	85	86	88	89	91	94	97	103	112	103	97	93	91	89	87	86	85	84
2.2	84	85	86	87	89	91	93	96	100	103	100	96	93	91	89	87	86	85	84
2.4	84	85	86	87	88	90	92	94	96	97	96	94	92	90	88	87	86	85	84
2.6	84	84	85	87	88	89	90	92	93	94	93	92	91	89	88	86	85	84	84
2.8	83	84	85	86	87	88	89	90	91	91	91	90	89	88	87	86	85	84	83
3.0	83	84	84	85	86	87	88	88	89	89	89	88	88	87	86	85	84	84	83
3.2	83	83	84	84	85	86	87	87	88	88	87	87	87	86	85	85	84	83	82
3.4	82	82	83	84	84	85	85	86	86	86	86	86	86	85	84	84	83	83	82
3.6	81	82	83	83	84	84	84	85	85	85	85	85	85	84	84	83	83	82	82
3.8	81	81	82	83	83	83	83	84	84	84	84	83	83	83	83	83	82	81	81

Table 3.4a Matlab ray-tracing model results in SPL (dB) for the factory.

x/y (m)	1	3	5	7	9	11	13	15	17	19
1	78.1	79.0	78.9	78.3	78.4	78.3	78.5	78.9	78.8	78.6
2	78.2	79.0	79.3	79.0	78.5	78.5	78.9	79.2	78.7	78.3
3	78.8	79.1	80.3	79.3	78.7	79.0	79.7	80.3	79.2	78.4
4	79.0	79.9	83.0	79.7	78.9	78.8	80.0	82.9	79.8	78.9
5	78.6	80.1	88.5	80.2	78.8	78.5	80.1	88.5	80.6	78.2
6	78.4	79.8	82.9	79.8	78.8	78.6	79.7	83.1	79.7	78.2
7	78.5	79.0	80.2	79.0	78.2	78.2	79.0	80.3	79.1	77.9
8	77.9	78.3	78.9	78.6	78.0	78.3	78.3	78.6	78.4	77.7
9	77.6	77.6	78.3	78.5	77.9	77.9	77.8	78.2	77.4	77.5
10	77.1	77.2	77.6	77.8	77.1	77.5	77.5	77.6	77.1	77.5
11	77.0	77.2	77.2	77.1	77.3	77.3	77.1	77.1	77.2	76.7
12	76.6	76.8	76.9	76.8	77.1	77.0	77.2	77.0	76.8	76.6
13	76.7	76.7	76.9	76.5	76.7	76.6	76.9	75.9	76.5	76.7
14	76.1	76.4	76.2	76.3	76.1	76.1	76.0	76.7	76.0	76.6
15	75.8	75.9	76.2	75.7	76.2	76.4	75.9	76.1	76.0	76.1
16	75.6	76.1	76.2	75.8	75.7	76.4	76.1	75.9	76.1	75.7
17	75.8	75.5	76.1	76.0	75.5	75.7	76.3	76.1	75.9	75.4
18	75.2	75.4	75.8	76.1	75.8	76.0	75.8	76.3	76.1	75.3
19	74.7	75.5	76.0	75.9	76.0	76.1	76.2	75.6	75.6	75.1
20	74.7	75.0	74.8	75.3	74.3	74.6	74.9	74.8	74.7	74.8
21	74.3	74.3	73.8	73.8	73.3	73.7	73.4	74.0	74.3	74.4
22	74.4	74.6	74.6	73.7	74.1	73.5	73.9	74.1	74.3	74.7
23	73.8	74.1	74.3	73.9	74.0	73.5	73.4	74.2	74.8	74.1
24	74.2	74.3	74.2	74.4	74.4	73.9	73.8	74.4	74.5	73.7
25	74.6	74.3	75.0	74.0	74.1	74.0	74.2	74.0	74.5	74.2
26	74.4	74.0	74.5	74.0	73.7	74.5	74.6	74.2	74.3	74.0
27	74.2	73.9	74.3	74.3	74.1	74.7	74.6	74.0	74.0	73.9
28	74.4	74.4	74.3	74.7	74.3	74.2	74.3	74.4	73.8	74.0
29	74.2	74.3	74.0	74.4	74.1	74.1	74.0	74.3	74.2	74.4
30	74.3	74.0	74.6	74.1	73.7	73.7	73.8	74.0	74.2	74.0
31	74.0	74.0	74.3	74.0	73.9	73.9	73.8	73.8	74.2	73.8
32	73.8	74.0	73.8	74.1	74.1	73.9	73.4	74.2	74.0	74.5
33	73.9	74.5	73.7	73.8	74.4	74.4	74.0	74.1	74.0	74.3
34	74.1	74.3	73.9	74.2	73.6	74.1	73.7	73.7	74.2	73.8
35	73.8	74.2	73.8	73.8	73.9	74.1	74.0	74.1	74.1	73.8
36	73.7	74.0	73.8	74.2	73.9	73.6	73.8	74.0	73.8	73.8
37	73.8	73.9	73.8	74.0	73.9	73.9	73.3	73.9	74.3	73.8
38	73.9	74.2	73.8	73.8	73.9	73.3	73.9	73.6	74.4	73.5
39	73.6	73.7	74.3	74.0	74.0	73.3	74.0	73.6	73.4	73.4
40	74.3	73.7	73.8	73.6	73.9	73.8	73.7	73.7	74.0	73.5
41	73.9	73.8	73.5	73.9	74.0	74.2	74.0	73.8	73.6	73.3
42	73.7	74.3	73.8	73.8	74.2	73.9	73.8	73.7	73.6	73.2
43	73.7	73.6	73.9	74.0	74.0	73.6	73.6	73.9	73.6	73.5
44	73.9	73.8	73.8	74.1	74.0	73.9	73.9	73.8	73.4	73.7

Table 3.4b Matlab ray-tracing model impact table for the factory.

Wall number	1st trajectory	2nd trajectory	3rd trajectory	All trajectories
1	2	19	33	7206
2	167	357	435	22338
3	149	355	488	22285
4	135	383	480	22166
5	138	387	429	22036
6	170	351	416	24461
7	147	363	386	24398
8	341	748	807	19310
9	2	6	21	10727
10	1707	1454	1675	83874
Obstacles	7042	5577	4830	141199
Diffractions	0	0	0	0

3.2.2 Parameters and Optimum Settings

The following sections present many ray-tracing results; thus a brief summary of the inputs is outlined here. The parameter values listed in this section were used for all predictions shown later; optimization of some parameters are discussed in the next paragraph. The room size was similar to the dimensions of the anechoic chamber (except rounded to the nearest meter, for convenience), so that the results could be compared to experiment. Absorptive walls had reflection coefficients of 0.01 and reflective walls had reflection coefficients of 0.9. Diffuse reflections were not considered. Phase changes upon reflection were also ignored. Air absorption was set to a negligible value of 0.0001 Np/m. Fitting zones, fitting density, and absorption from fittings were not used unless explicitly stated otherwise. The frequency was set to 1000 Hz. The position of a single source varied, but its power was set to L_w = 100 dB. The receiver height was 0.02 m above the ground for predictions of the experimental configurations, to approximate placing the microphone on the wire-mesh floor of the anechoic chamber. For all other configurations, the receiver height was fixed at 1 m. The cells of the receiver spanned the entire length and width of the room at that height. Hence, all figures will show results over a plane in the room. These ray-tracing parameters describe the basic characteristics of the anechoic chamber, and did not need to be changed throughout the tests.

Certain parameters required optimization in order to achieve high statistical accurate of the prediction results. These include the number of rays, the number of trajectories, and the size of the receiver cells. Increasing the number of rays renders the source more omni-directional, increases the number of rays striking each receiver cell, and makes the results more continuous between adjacent receiver cells, but at the cost of runtime. If an inadequate number of rays is used, some receiver cells are missed completely and show a quiet spot in the domain, which is an inaccuracy. We found that the minimum number of rays is 300,000 to achieve acceptable results. The number of trajectories refers to how many re-directions (reflections and diffractions) a ray is traced for. For the anechoic-room setup studied in this chapter, this parameter makes little difference, because reflections are strongly absorbed. Since diffractions count towards this number, we used three trajectories. Note that runtime increases with the number of trajectories. Finally, the receiver-cell size (or mesh size) defines how finely the receiver area is partitioned. A smaller cell size can resolve finer detail, such as edges of diagonal walls, and phase. The drawbacks are the need for more computer resources to store and plot results; also some cells may be missed entirely if insufficient rays are used. We found that six receiver points per wavelength worked well; this corresponded to a 5-cm mesh at 1000 Hz. A finer mesh produced figures that do not display well; the images appear solid black as the colour of each cell could not be resolved in a Matlab surface plot. However, this could be alleviated by shrinking the maximum receiver area. A coarser mesh gave suboptimal phase results.

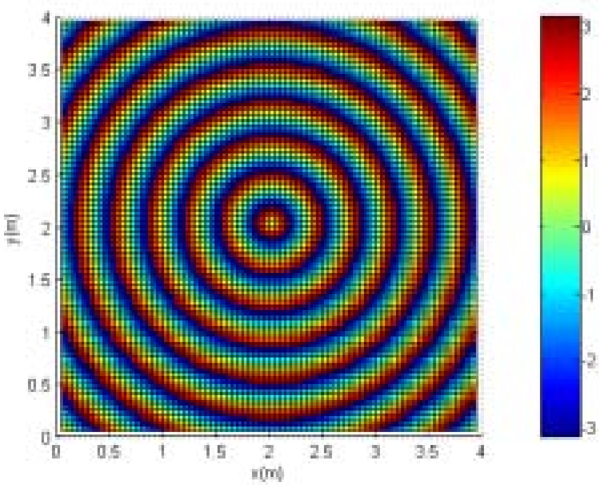

Figure 3.1 Phase in radians of a source along a plane in an anechoic room; the source is at (2,2).

3.3 Phase Implementation

Phase was added to the model by considering the total distance traveled by the ray from the source to the receiver. The ray's energy contribution was multiplied by $\exp(ikr)$, and then added to the cumulative pressure at the receiver. As a result, rays with different total path lengths interfere properly. Figure 3.1 shows the phase plot of the field due to an omni-directional source in an empty anechoic room. As expected, it consists of concentric circular rings around the source, because phase varies linearly with distance, with no angular dependence.

3.4 Diffraction Implementation

The last major addition to the ray-tracing model was diffraction. Without diffraction, unrealistic shadow zones are predicted behind interior surfaces, which reflections alone cannot account for. An example of such a case can be seen in Figure 3.2; it has two angled walls which intersect, forming a V-shaped wedge in an anechoic chamber that creates a shadow region. From Figure 3.2, the maximum SPL predicted in the shadow zone is 55 dB, which is too low compared to reality.

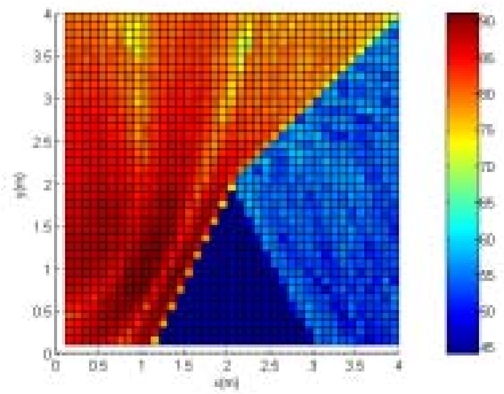

Figure 3.2 Predicted SPL (dB) in an anechoic chamber with a V-shaped wedge, without diffraction; the source is at (1,1).

Therefore, the objective was to diffract sound around the edges of the interior surfaces as our experiences in physical reality suggest. This was accomplished by re-directing rays that impinge on the interior surface towards the shadow zone, and adjusting their amplitude and phase by the diffraction coefficient *D,* as defined by the Uniform Geometric Theory of Diffraction [18]. The algorithm is summarized as a flowchart shown in Figure 3.3. When a ray strikes an interior surface, a decision is made on whether to diffract the ray or not. If the ray is not diffracted, it is simply reflected as in the original model. If the ray is diffracted, all angles are calculated from the room geometry, including a random angle that determines the direction that the ray propagates into the shadow zone. The starting point of the ray's next trajectory is moved to the edge of the interior wall. Note that if a particular three-dimensional direction is unaffected by bending the ray around the edge, then that component of the ray's direction does not change. Next, the angles and distances are used to calculate the diffraction coefficient. After the ray's pressure is adjusted by the diffraction coefficient, the current trajectory of the ray ends, and the next one begins. It is during the next trajectory that the ray travels through the shadow zone, starting at the edge of the interior surface. Each of these steps will be explained in more detail in the following subsections.

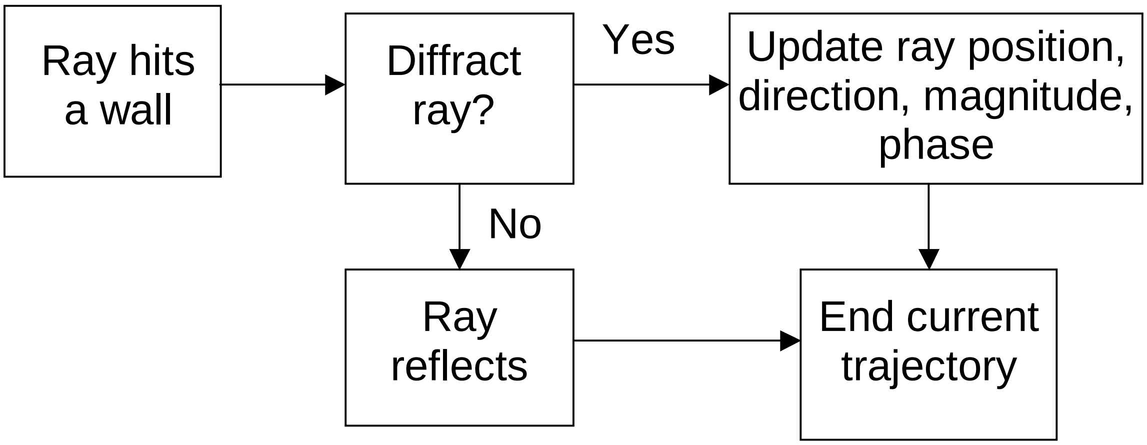

Figure 3.3 Implementation of diffraction into the existing model.

3.4.1 Diffraction Conditions

The decision whether or not to diffract a ray is based on a few factors. The first is simply a user-defined flag, named DFRCT, to give the user the option to turn all diffractions on or off. It has been added to the last line of the input file. Secondly, only first-order rays are diffracted. This means that diffracted rays must encounter the interior wall on their first trajectory; that is, they must come directly from the source. Diffraction of reflected rays and second-order diffraction are not considered. Next, the ray is only diffracted if it hits close enough to the edge of the interior wall. The $\lambda/2$ criterion from section 2.3.4 is applied here. Note that rays that do not hit the interior wall, but pass within $\lambda/2$ of its edge, are not diffracted. The next two conditions are purely technical ones to quickly screen out rays that could not be diffracted. The ray must have last struck an interior, or "constrained" wall. This is common sense, because a ray cannot bend around an outer wall; otherwise it would go outside the domain. Finally, if the ray strikes near an edge of the interior wall, that edge cannot be connected to an outer wall. It may be joined to another interior wall, in which case the two walls form a wedge. Alternatively, it may be connected to nothing ("hanging" walls), as in the case of diffraction over a fence. A variable called WALREL ("wall relationships") is created to serve as a quick look-up table to find what each edge of the interior walls is connected to.

Implementing this variable involved inputting the edge points into the plane equations of the other walls to check for intersections. Thus the limits of the constrained walls should not overshoot the coordinates of the outer walls, otherwise an intersection may not be found. In effect, we are searching for all diffracting edges and storing them this data structure. In any case, once the decision to diffract the ray has been made, the wedge angle, incident angle and diffracted angle must be calculated.

3.4.2 Angle Calculations

Three angles are needed to calculate the diffraction coefficient: the angle of the wedge, the incident angle of the incoming ray, and the diffracted angle of the outgoing ray. Figure 3.4 shows the definitions of these angles. Of the three required angles, the wedge angle is easiest to find. The dot product between two normalized vectors gives the cosine of the angle between them. Next, calculating the incident angle simply involves finding the slope between the starting point of the ray and the edge of the interior wall. Lastly, for the diffracted angle, two slopes are needed to create upper and lower limits for the randomly-generated diffracted angle. One limit is the slope used to find the incident angle; the other limit is imposed by the slope of the connecting wall. Once the slopes are found, the inverse tangent function converts them to angles between $-\pi/2$ and $\pi/2$. With the two angles that bound the shadow region, a random angle of diffraction is chosen in between them, so that the ray is guaranteed to travel into the shadow region. However, this may not be the suitable angle, given the configuration of the source and diffraction point. Hence a large (and computationally inefficient) set of if-statements is used to distinguish between all source and edge-tip position combinations and their diffracting paths. This way, the angles are correctly placed in their appropriate quadrants, and the program is robust enough to handle diffraction from any direction. Figure 3.5 shows a polar plot of the diffracted rays emerging from the V-wedge seen in Figure 3.2. Notice that all the rays enter the shadow zone, without accidentally passing through the wedge itself.

Some complications arose that increased the complexity of the code; they will be listed here without extensive discussion. For a particular interior wall, its position could be rotated to symmetric locations in the room, so extra care is needed to identify which coordinate directions take part in the diffraction, and which angle is really the azimuthal or elevation angle. Also, diffracting edges formed by certain types of interior walls are handled differently. Between combinations of wedges formed by two interior walls as compared to one (hanging) interior wall, and walls parallel to the coordinate axes as compared to inclined walls, the amount of code effectively doubles. In the end, the case of inclined hanging walls was not successfully coded. Furthermore, a ray could strike close enough to more than one edge of an interior wall. In this case, one of the possible edges is chosen randomly. Finally, vertical diffractions have a separate section of code because only the *z*-component of the ray's direction changes.

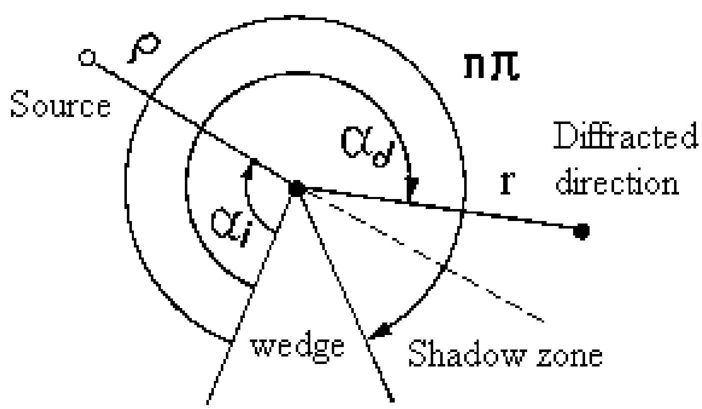

Figure 3.4 Geometry and angles involved in diffraction.

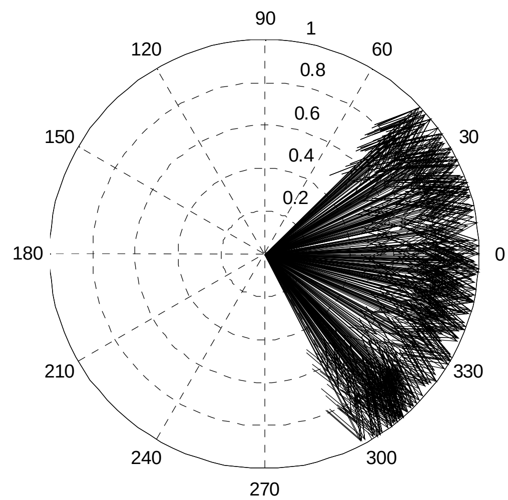

Figure 3.5 Predicted angles of diffraction for rays entering the shadow zone behind a V-wedge. The center of the polar plot represents the tip of the wedge.

3.4.3 Diffraction Coefficient

Having calculated all the angles and geometrical parameters, we compute the diffraction coefficient D. The following equations are from Kouyoumjian and Pathak's Uniform Geometric Theory of Diffraction [18]:

$$D(n,k,\rho,r,\theta_i,\alpha_i,\alpha_d) = -\frac{e^{i\frac{\pi}{4}}}{2n\sqrt{2k\pi}\sin\theta_i} \bullet \left[\begin{array}{l} \tan^{-1}(\frac{\pi+(\alpha_d-\alpha_i)}{2n})F\left(kLa^{+}(\alpha_d-\alpha_i)\right) \\ +\tan^{-1}(\frac{\pi-(\alpha_d-\alpha_i)}{2n})F\left(kLa^{-}(\alpha_d-\alpha_i)\right) \\ +\tan^{-1}(\frac{\pi+(\alpha_d+\alpha_i)}{2n})F\left(kLa^{+}(\alpha_d+\alpha_i)\right) \\ +\tan^{-1}(\frac{\pi-(\alpha_d+\alpha_i)}{2n})F\left(kLa^{-}(\alpha_d+\alpha_i)\right) \end{array}\right] \tag{3.1}$$

where (see Figure 3.4):

k is the wave number, $k = 2\pi / \lambda$,

n (also called the wedge index) is such that the exterior wedge angle is $n\pi$, $n \in (0,2]$,

ρ is the source to diffraction point distance,

r is the receiver to diffraction point distance,

θ_i is the azimuthal angle between the edge vector and the incident direction $\theta_i \in [0, \pi]$,

α_i is the elevation angle between the wall vector and the incident direction $\alpha_i \in [0, n\pi]$,

α_d is the elevation angle between the wall vector and the diffracted direction $\alpha_d \in [0, n\pi]$,

and where *F(X)* is the Fresnel integral given by:

$$F(X) = 2i\sqrt{X}e^{iX} \int_{\sqrt{X}}^{+\infty} e^{-i\tau^2} d\tau \tag{3.2}$$

and

$$L = \frac{\rho r}{\rho + r} \sin^2 \theta_i , \tag{3.3}$$

$$a^{\pm}(\beta) = 2\cos^2 (\frac{2\pi n N^{\pm} - \beta}{2}), \tag{3.4}$$

$N^{\pm}$ is the integer that satisfies more closely the relations:

$$2\pi n N^{+} - \beta = \pi \text{ and } 2\pi n N^{-} - \beta = -\pi \tag{3.5}$$

Several approximations exist in the related literature, useful for implementing the above equations. In particular, Eq. (3.5) reduces to:

$$N^{+} = \begin{cases} 0 \, for \beta \le \pi(n-1) \\ 1 \, for \beta > \pi(n-1) \end{cases} , \tag{3.6}$$

$$N^{-} = \begin{cases} -1 & for \quad \beta < \pi(1-n) \\ 0 & for \quad \pi(1-n) \le \beta \le \pi(1+n) \\ 1 & for \quad \beta > \pi(1+n) \end{cases}. \tag{3.7}$$

Kawai [13] gives an approximate rational expression for the Fresnel integral in Eq. (3.2):

$$\begin{aligned} &for\ X < 0.8: F(X) = \sqrt{\pi X}\left(1 - \frac{\sqrt{X}}{0.7\sqrt{X} + 1.2}\right)\exp\left(i\frac{\pi}{4}\sqrt{\frac{X}{X+1.4}}\right) \\ &for\ X \ge 0.9: F(X) = \left(1 - \frac{0.8}{(X+1.25)^2}\right)\exp\left(i\frac{\pi}{4}\sqrt{\frac{X}{X+1.4}}\right) \end{aligned} \tag{3.8}$$

Eq. (3.1) is still singular at a reflection or shadow boundary and cannot be evaluated numerically at these boundaries. However, near the boundaries, we can express the terms $\alpha_i \pm \alpha_d$ as $\beta = 2\pi n N^{\pm} \mp (\pi - \varepsilon)$. The coefficient is then continuous and its value can be computed using [18]:

$$\tan^{-1}\left(\frac{\pi \pm \beta}{2n}\right)F\left(kLa^{\pm}(\beta)\right) \approx ne^{\frac{i\pi}{4}}\left(\sqrt{2\pi kL}\,\mathrm{sgn}(\varepsilon) - 2kL\varepsilon e^{\frac{i\pi}{4}}\right) \tag{3.9}$$

where $\mathrm{sgn}(\varepsilon) = 1$ if $\varepsilon > 0$ and -1 otherwise.

Note that, in our implementation of the above formulae, the edge-to-receiver distance was set to 0.01 m because the current trajectory of the ray ends. Magnitude attenuation with distance occurs in the ray's next trajectory. This completes the discussion of the diffraction additions to the ray-tracing model.

3.5 Validation Tests

Several configurations were predicted to test that the improved ray-tracing model worked properly. The goal was to ensure that the model is robust enough to handle diffraction around any physical placement of constrained walls within the domain. This included situations such as a fence, a screen, a doorway, a right-angle corner, a V-shaped wedge, or a square pillar. Each of those configurations could be rotated a number of times, and also could have different wall heights and sound frequencies. This set of obstacles and their permutations were chosen to involve all the complications discussed previously, such as inclined walls, hanging walls, and rotations. Results will not be shown for all of the cases; only a few sample cases are shown in Figures 3.6, 3.7 and 3.8. Overall, the model produces similar results for rotated rooms, and it handles well wedges formed by both inclined and straight interior walls. It also handles hanging straight walls, but not hanging inclined walls, as expected, since they were omitted from the implementation. Figures 3.2 and 3.6 share the same room configuration (a wedge created by two intersecting inclined walls), but with and without diffraction. The results with diffraction are clearly better, because the shadow zone is traversed by diffracted rays instead of only strongly attenuated reflected rays, creating sound-pressure levels of at least 70 dB, which is more realistic.

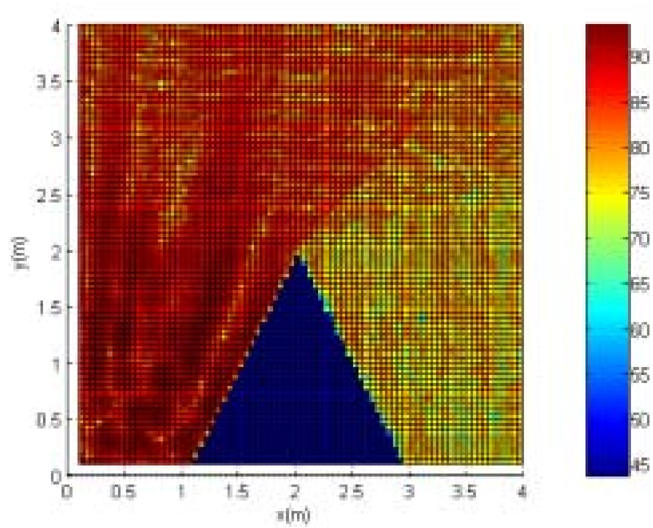

Figure 3.6 Predicted SPL (dB) in an anechoic room showing diffraction around a V-wedge formed by inclined walls for a source at (1,1).

We also tested some configurations that were studied in the literature. Figure 3.7 shows predicted results for the configuration used in [27], which also serves as an example of a right-angle wedge formed by two straight walls. Note that the results in this figure are normalized by the free-field SPL. The field in front of the block should contain zones of +6 dB and -6 dB relative SPL, due to interference between the direct and reflecting waves. However, this is not predicted near the edge, because rays striking near the edge are diffracted instead of reflected. Far away from the corner, the difference in SPL relative to free field should be 0 dB, because the wedge has minimal effect. The ray-tracing prediction has differences of up to ±4 dB, likely due to randomness and variability between predictions. Along the x=0.3 m line, ray-tracing predictions agree well with the literature near the vertex of the edge, but are several decibels lower in the shadow zone.

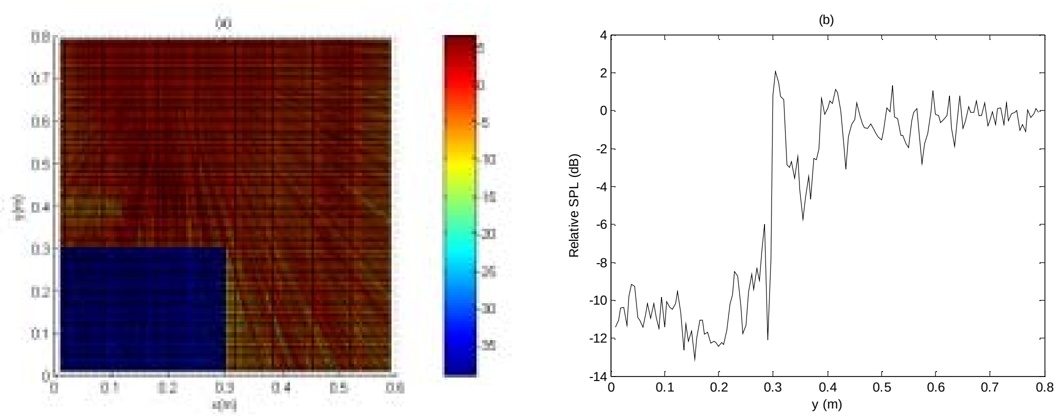

Figure 3.7 Predicted pressure field showing diffraction around a wedge formed by straight walls for a source at (0.2,0.8). SPL relative to free field is plotted in dB (a) for the whole surface and (b) along the x=0.3 m axis.

Another example that was predicted is that of one interior wall, parallel to a coordinate axis, connected to nothing, as seen in Figure 3.8. It is located at y=2.5 m, extending from x=0 m to x=2.5 m. A similar configuration is presented in [28], except that the distances are not the same, the relative source and edge positions are different, and the room is rotated. In both set of results, the SPL in the shadow zone is 10-20 dB lower than at the tip of the wall. The biggest difference between our results and the literature is for the continuity at the boundary, where the ray-tracing data provided a smoother transition into the shadow region. The phase results are very good, because the wave fronts in the shadow zone matched up with those in the direct field. Also, the phase is shifted on one side of the wall due to reflections. Notice that, in all of these cases, the shadow zones are not uniformly quiet as in the non-diffractive results. Sound decays gradually as the receiver moved deeper into the shadow zone. SPL's are smallest at the deepest corners within the shadow zone and largest at the boundary. In the phase plots, the wave fronts could be seen propagating into the shadow region. At the zone boundary, there is a slight discontinuity in some cases, but otherwise the wave fronts appear well aligned.

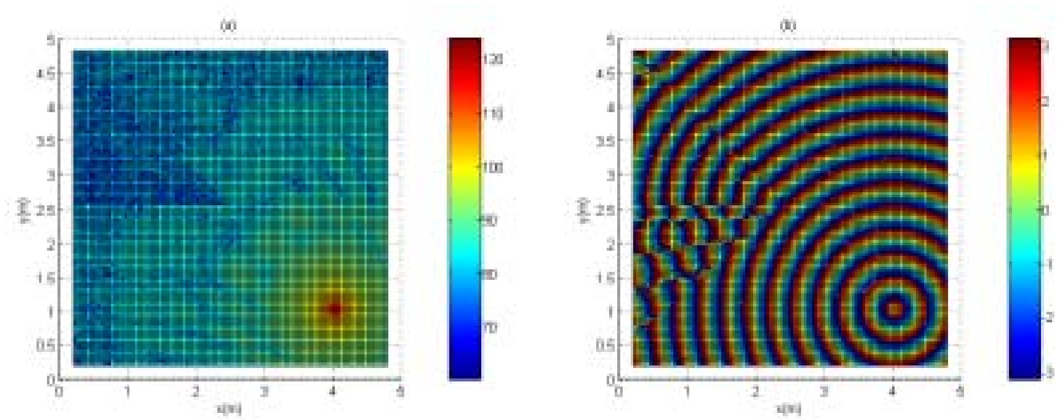

Figure 3.8 Predicted pressure field showing diffraction around a hanging straight wall for a source at (4,1): (a) amplitude in dB and (b) phase in radians.

3.6 Prediction of Experimental Configurations

Recall that in Chapter 2, we presented experimental results for an edge, a block and multiple blocks. We can simulate the same experimental configurations with the improved ray-tracing model to predict the sound field and test the accuracy of the predictions.

3.6.1 One Edge

The single diffracting-edge result predicted by ray tracing is plotted in Figure 3.9, along with the previous results from Figure 2.8. The ray-tracing results show less smooth variations than do those for the cylindrical wave. Although the oscillations do not completely coincide with those of the cylindrical wave, they peak and dip at nearly the same locations. This makes sense, because the experimental imperfections are modeled in ray tracing. That is, the flanking path over the top of the wall exists in ray tracing as in experiment. Recall that, as the distance from the edge increases, the flanking path becomes more significant. This is a reasonable explanation for why the ray-tracing and theoretical results match close to the edge, but deviate further away. Surface plots of magnitude and phase are shown in Figure 3.10. The magnitude decays as expected outside the shadow zone, but the decay is not uniform in the shadow region. Instead, it shows random fluctuations at a SPL lower than that in the non-shadow region. Phase varies linearly with distance in both regions. At the boundary between the direct and shadow zones, the amplitude is 10 dB lower in the shadow zone, and the phase is slightly mismatched. The wave fronts are not as sharply defined (compared to the similar configuration in Figure 3.8), probably because of interference with the flanking rays over the top of the wall.

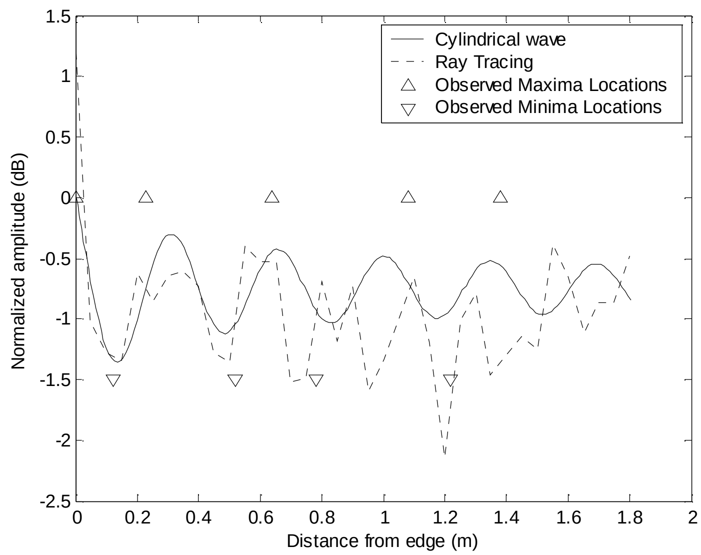

Figure 3.9 Comparison of ray-tracing results to experiment and theory for one edge.

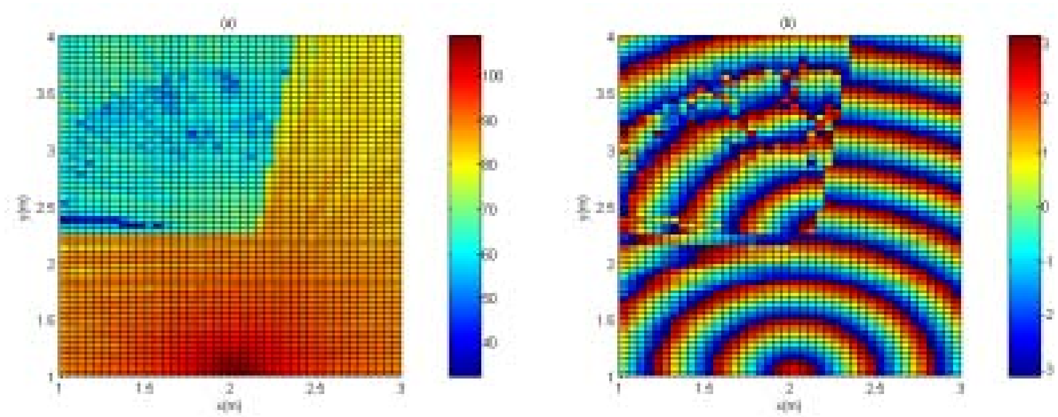

Figure 3.10 Predicted pressure field for the one-edge configuration; the source is at (2,1): (a) amplitude in decibels and (b) phase in radians.

3.6.2 One Block

Using six intersecting straight walls, a square block is modeled in the center of an anechoic room. Ray-tracing results for this case are plotted in Figure 3.11 along with experimental results from Figure 2.13, showing the pressure in front of the block. The agreement is not great, but the ray-tracing results still have the measured features. Interference effects are seen close to the block – in particular, the maximum at x=0.5 m between two minima at x=0.43 m and x=0.6 m. However, their locations are not exactly the same, and the predicted relative amplitudes do not vary as strongly as the measured amplitudes. This inaccuracy in front of the block could be attributed to the lack of reflected rays. Most of the rays that strike the front surface of the block are diffracted into the shadow zone, instead of reflected. Hence, there is insufficient interference in front of the block to reproduce the experimental results accurately. However, the traces of the correct interference pattern are predicted, despite the lack of reflected rays. As for the results in Figure 3.12 showing the corresponding surface plots, the predicted sound field on either side of the block is realistic. The shadow zone behind the front corners of the block is continuous in both amplitude and phase. However, the shadow zone behind the block is not reached by any rays, due to the lack of second-order diffraction.

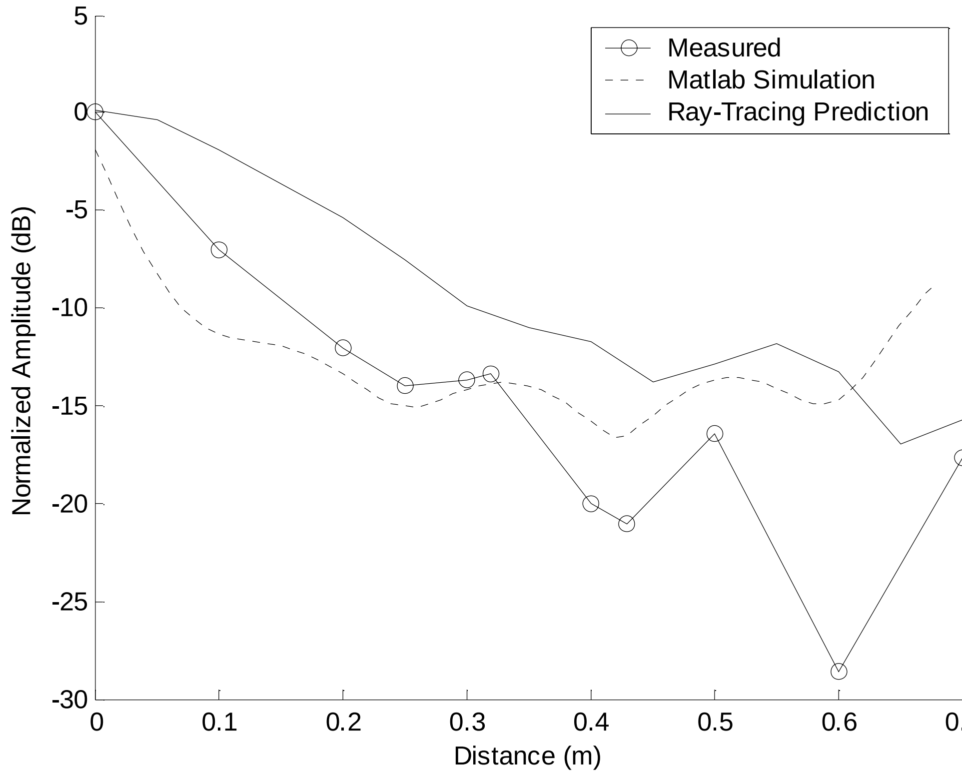

Figure 3.11 Comparison of ray-tracing results with experiment and theoretical simulation in front of one block.

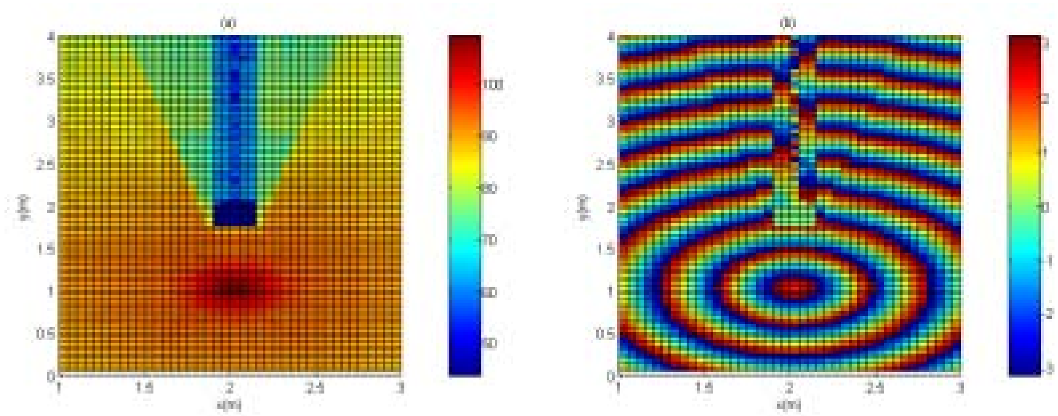

Figure 3.12 Predicted pressure field for the one-block configuration; the source is at (2,1): (a) amplitude in decibels and (b) phase in radians.

3.6.3 Multiple Blocks

To predict the multiple-block configuration from Figure 2.15, the fitting-zone feature of the original ray-tracing model was used. Hence, the new diffraction algorithm took no part in generating these results. The domain was split into four volumes by two fitting zone planes, z=0.3 m and x=2.0 m. Obstacles were placed into the region x>2 m and z<0.3 m as in the experimental setup. Their reflection coefficient was set to 0.9, which was the same as the other varnished wooden surfaces. A mean free path of 0.9966 m was calculated from the block positions, so a fitting density of 1/0.9966 = 1.0034 m^{-1} was used. Figure 3.13 plots the experimental results, along with the prediction along the central axis. The ray-tracing results follow the free-field levels until several centimeters into the fitting zone, where they begin to drop off due to scattering from the blocks. However, the experimental result did not drop off as much. Figure 3.14 shows the surface plots in amplitude and phase. Again, the amplitude decays in general, but the randomized scattering creates oscillations about the main downward trend. Phase behaves linearly, but the obstacles randomly scatter the wave fronts in the fitting zone. Note that the phase changes are due to interference between rays of different path length; no phase shifts occur when objects are encountered.

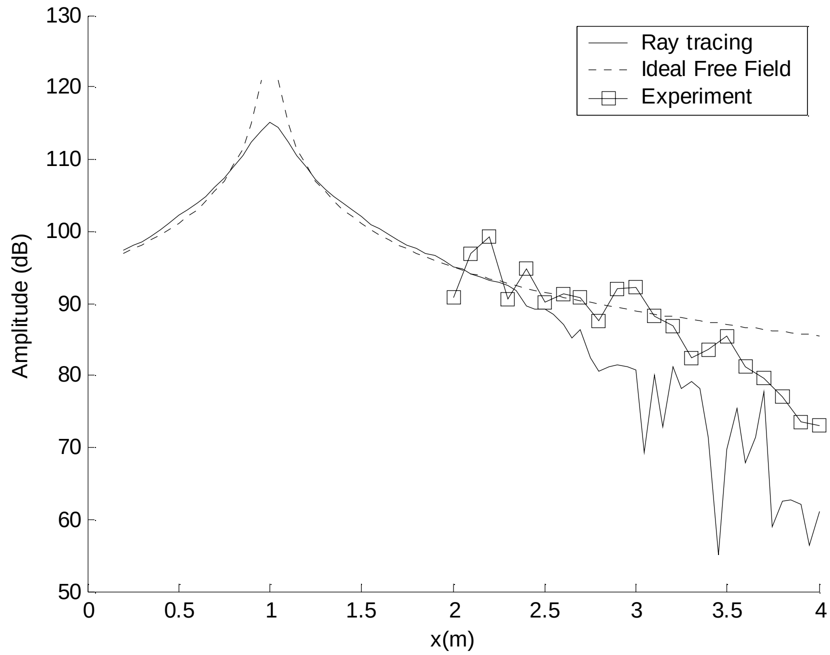

Figure 3.13 Comparison of ray-tracing results with experiment for the multiple-block case using random fittings, along the central axis.

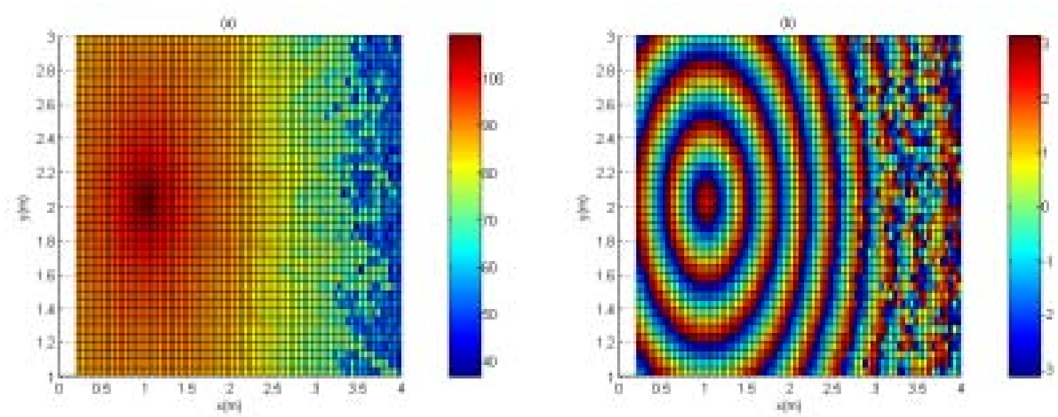

Figure 3.14 Predicted pressure field for the multiple-block configuration with random fittings; the source is at (1,2): (a) SPL in dB and (b) phase in radians.

The multiple-block configuration was predicted again using the diffraction algorithm rather than the random fittings. Using six intersecting interior surfaces to construct each of the nine blocks, the setup seen in Figure 2.15 was modeled. This was a cumbersome process because the planar equation and the limits of the range of the coordinates (x,y,z) had to be specified for each of the block's six sides. For simplicity, all blocks were rotated such that their surfaces were parallel or perpendicular to the coordinate axes. Figure 3.15 plots the experimental results, along with the prediction along the central axis. Compared to the prediction using the fitting-zone feature in Figure 3.13, the agreement with experimental results is better since the curves are closely matched until x=3.3 m. The presence of a block near x=3.5 m causes the SPL to drop significantly, since sound does not penetrate into the block. Behind the block, levels remain low because there is no second-order diffraction. Figure 3.16 shows the surface plots in amplitude and phase. Predicted sound-pressure levels in shadow zones are noticeably lower (by about 10 dB) than in direct regions. The SPL in shadow zones that were reached by single-order diffractions is at least 65 dB. Due to the lack of higher-order diffraction, the predicted SPL in several shadow regions behind the blocks is 50 dB or lower. This is too low because in the experimental results, the lowest SPL measured was about 70 dB. The predicted phase varies linearly in direct regions and shadow regions reachable by first-order diffraction. In shadow zones that could not be accessed by first-order diffraction, the phase results are difficult to interpret. The phase is composed of reflected rays, and it appears scattered and nonlinear.

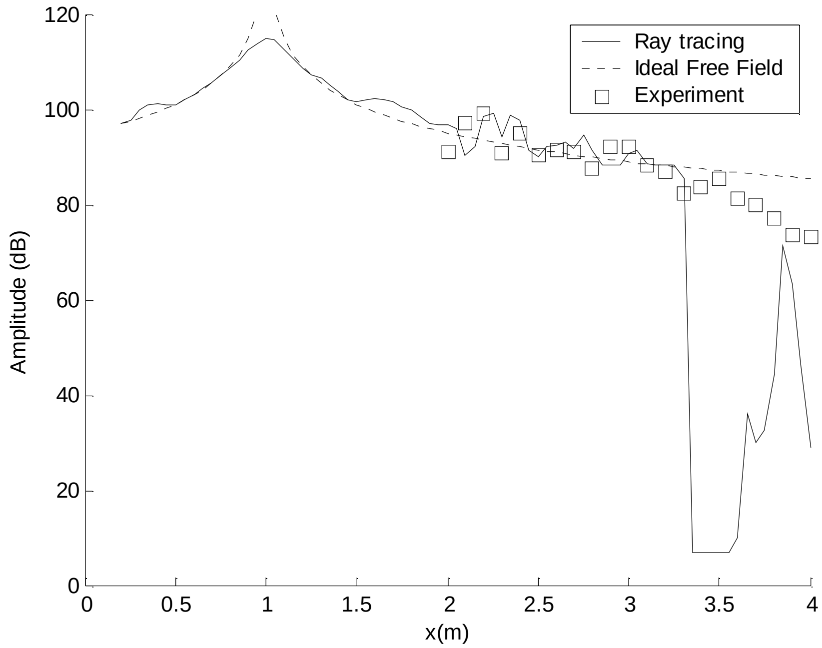

Figure 3.15 Comparison of ray-tracing results with experiment for the multiple-block case using the diffraction algorithm, along the central axis.

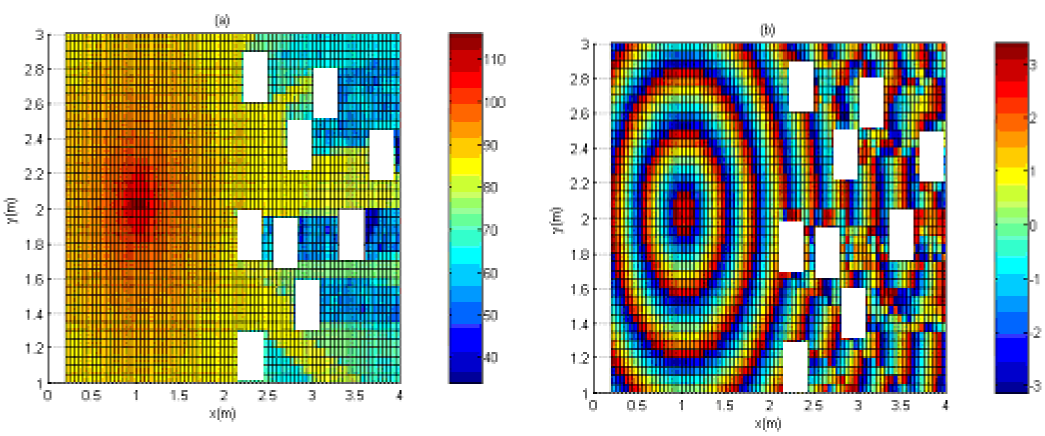

Figure 3.16 Predicted pressure field for the multiple-block configuration using the diffraction algorithm; the source is at (1,2): (a) SPL in dB and (b) phase in radians.

3.7 Known Problems

To conclude the section on the ray-tracing model, we first summarize the known problems and inaccuracies, and then finish with some suggested improvements in the next section. First we review previously-stated problems. In both the original and improved ray-tracing models, sound levels are overestimated for receiver cells that contain the source. Thus, for neighbouring receiver cells, the decibel levels appear to decay too quickly. Fittings are encountered more often in the improved model. In our implementation, hanging inclined walls and second-order diffraction are omitted. Note that, although the region behind a square obstacle cannot be predicted, the model still succeeds when the square is rotated. Also, in our approach to diffraction, we reduced the number of reflections in favour of diffraction into the shadow zone. Hence the sound field near an edge on the incident side no longer contains a reflected wave, which may be inaccurate if the reflected wave is significant. However, the accuracy behind the edge is an adequate compromise for the slight inaccuracy in front of the edge. Diffraction could be implemented differently to avoid this problem, but at the cost of other complications.

As an aside, we tried a smoothing technique that was intended to assign missed receiver cells an average value depending on its neighbouring cells. The origin of this procedure came from image-processing masks, used to filter out salt-and-pepper noise in a picture, or increase contrast by emphasizing edges, for example. We intended to reduce the runtime of the ray-tracing model by decreasing the number of rays, and compensating the inaccurate receiver cells by applying the smoothing mask, which is a computationally simpler post-processing maneuver. It succeeded in blurring discontinuities, but it affected all the receiver cells and erased some of the positive features. For instance, sharp edges became blurry, and the -6 dB/dd decay rate was reduced. Therefore, the smoothing the results was omitted from our results; increasing the number of rays was the preferable way to eliminate singularities.

3.8 Suggested Changes

Some changes could be made to the ray-tracing model to increase its efficiency and accuracy. The most important improvement would be to include second-order diffraction. The difficulty with this is that the rays of neither the source nor the first-order edge source can physically contact a point on the wall near the second corner. The rays would have to stop in mid-trajectory when a second corner is found, and make the turn. This is difficult to implement, because either the secondary edge must be assigned a finite volume, or decisions must be made along the trajectory to check if the ray should suddenly make a turn. Another possibility is to position the first-order source such that it protrudes from its actual location, so that a small range of angles will hit close to the second edge. Either way, care must be taken to avoid introducing new shadow zones that could arise when bending certain rays. Furthermore, the implementation has to realistically model diffraction.

The suggestions for efficiency improvements are minor. One is to eliminate the upper limits on parameters such as the number of walls, constrained walls, sources, etc. These are required in the Fortran model because all variables and array sizes must be declared at the beginning. In Matlab, there is no such constraint and declaring variables this way makes them bigger than needed, which is a waste of memory. However, upper limits would still be useful for the number of receiver cells, since figures with too many receiver cells display poorly. Also, while the multiple-frequency capability is handy, it does not work with diffraction, since the ray's trajectory depends on frequency. Thus, only one frequency can be studied at a time. Although the program does not crash, the downside with having more than one frequency is that displaying the multi-dimensional array becomes slightly inconvenient. An extra loop is required to convert the incompatible n-dimensional matrix to a 2D matrix.

3.9 Finite Element Method

The finite element method (FEM) is a second prediction model used to generate sound fields around cubic obstacles. It was briefly introduced in section 1.4.2. Predictions with this model were done by collaborators Matthieu Boirlaud and Vincent Valeau at the Université de Poitiers, France. The objective of the FEM work was to confirm and validate the experimental work and ray-tracing predictions. The model was used to simulate two of the experimental configurations: the anechoic chamber with the single block and with the multiple blocks. According to [29], the prediction domain was partitioned into a mesh with six points per wavelength. The whole domain had 153653 elements for the single-block case, and 791547 elements for the multiple-block case. Runtimes were only a few minutes, which is much faster than ray tracing. Furthermore, it is noted in [29] that the FEM phase results are slightly inaccurate for large distances due to a dispersion phenomenon. Compared to the ideal phase of the Green's function (the mathematical analogy of a point source), the phase seems to be about half a radian lower that the exact phase, for x>1.5 m.

3.9.1 Single-Block Results

Results with a single block can be seen in Figures 3.17, 3.18 and 3.19. In the plots of FEM prediction results, the source is always at x=0 m and the spaces between data points indicate the presence of a block. In the single-block results, the block occupies the space between x=0.7 m and x=1.0 m. In Figure 3.17, experimental results are compared to FEM, with good agreement. In front of the block, the fluctuations in the sound-pressure level agree very well, with perhaps a slight shift which is more evident in the phase results. Behind the block, the two phase results overlap, while the magnitude results for the FEM are higher immediately behind the block. Figure 3.18 compares FEM simulations with and without the block; refer to Figures 2.13 and 2.14 for the same experimental comparison. The amplitude results are as expected and they confirm the

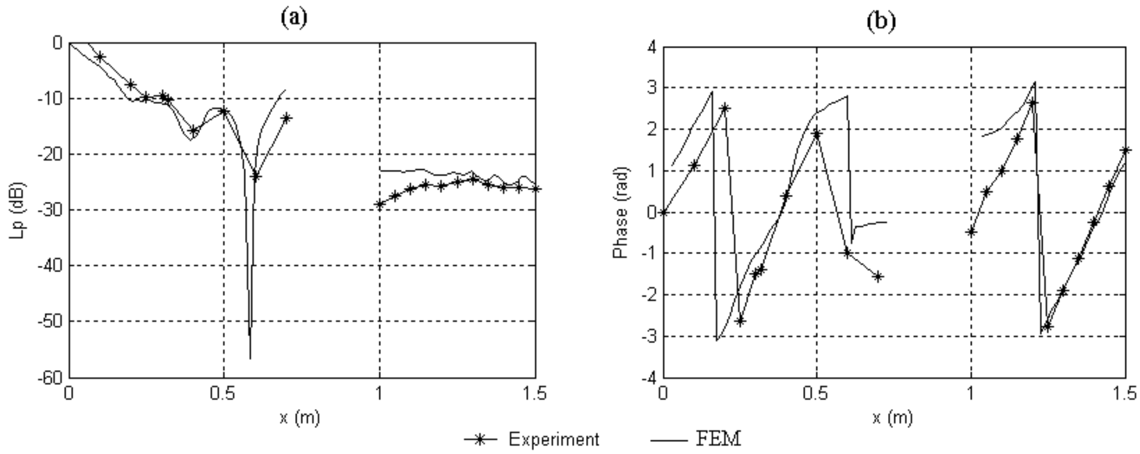

Figure 3.17 Comparison of pressure predicted by FEM and experiment for the one-block case: (a) normalized amplitude in decibels and (b) phase in radians.

experimental results. The phase results also agree with experiment, since the phase changes relative to free field occur most noticeably near the front of the block (due to the reflected wave) and behind the block (due to increased path length from diffraction).

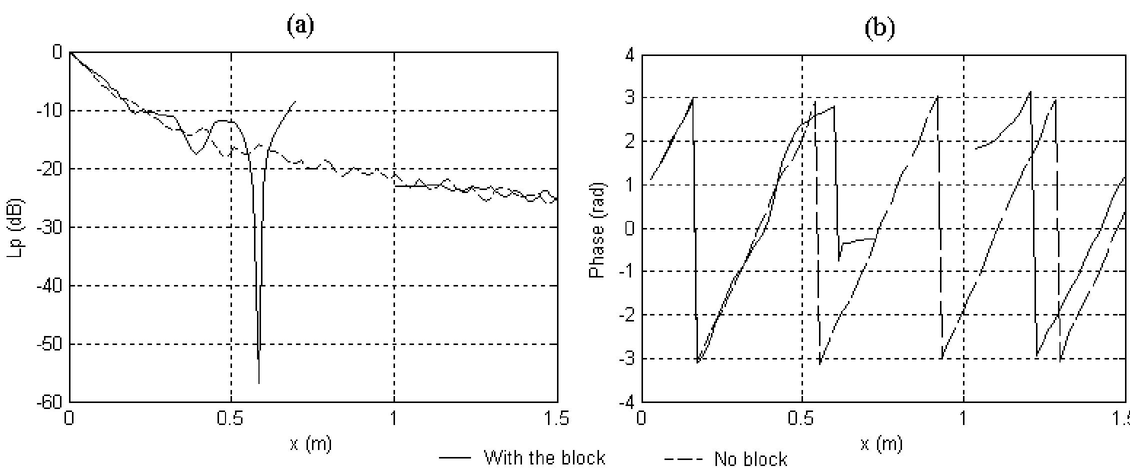

Figure 3.18 FEM prediction comparing SPL with and without a block: (a) normalized amplitude in decibels and (b) phase in radians.

The final graph for the single-block results, Figure 3.19, shows the sound field over the z=0.15 m plane. However, the block is moved to a different position. It occupies the space between x=0.3 m and x=0.6 m. These results can be compared to the ray-tracing results in Figure 3.12. The biggest difference is behind the block, where the lack of second-order diffraction causes a shadow zone in the ray-tracing results. With FEM, there is an interesting local maximum behind the block, which was observed in experiment. Phase also shifts the most behind the block, as the pattern of concentric circles is perturbed. At the back corners of the block, a slightly quieter zone emerges from both ray tracing and FEM. In front of the block, the sharp interference dip is more visible in FEM than in ray tracing. This is likely because of the decision to diffract rays, rather than reflect them, in the ray-tracing algorithm.

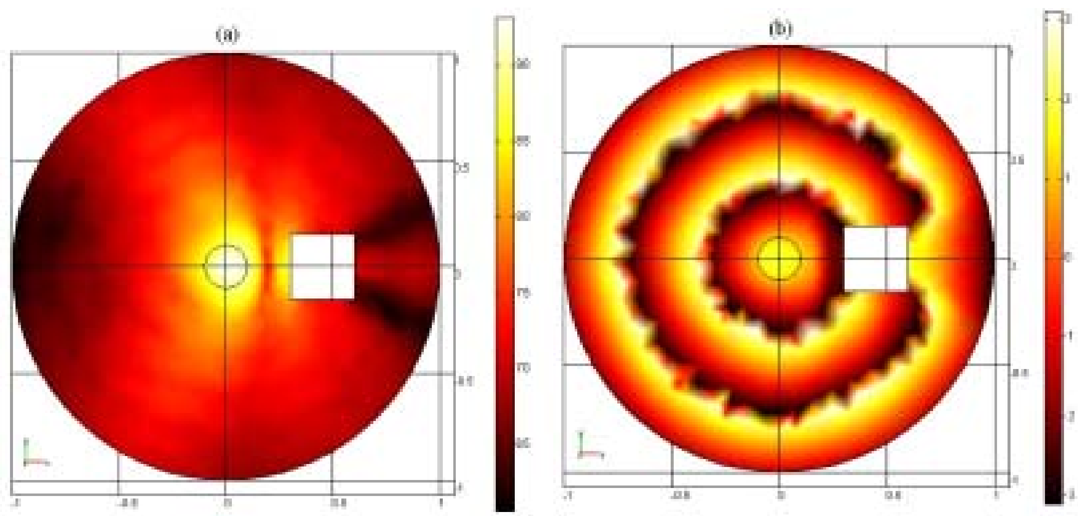

Figure 3.19 FEM prediction of the sound field around a block:
(a) amplitude in decibels and (b) phase in radians.

3.9.2 Multiple-Block Results

The multiple-block configuration in Figure 2.15 was modeled with the FEM. The positions and rotations of the blocks were approximated from the photographs of the experiment, Figure 2.16. We will compare the simulation and experimental results along the central axis, the +18^o direction, the -18^o direction, and the $\sqrt{5}$ m arc, in magnitude and phase. We will also compare the free-field (no-block) case with the multiple-block configuration, to investigate phase changes predicted by the FEM.

Figure 3.20 compares the FEM results along the central axis with measured data. In general the FEM amplitude and phase results match the experimental data reasonably well. The FEM amplitude prediction oscillates more, but it follows the downward trend of the experimental data. The phase agreement is worst near the blocks at x=1.3 m and x=1.6 m. In Figure 3.21, the results with multiple blocks are compared to free field to detect phase changes. The phase begins to behave nonlinearly around x=1.6 m, presumably because of reflections from a nearby block. After x=2.5 m, the phase is again linear, but seems to be displaced vertically. This is likely because of a block at that location, which sat along the central axis, obscuring the direct path. Thus it appears that the sound diffracted around the block, and the increased path length caused the phase shift.

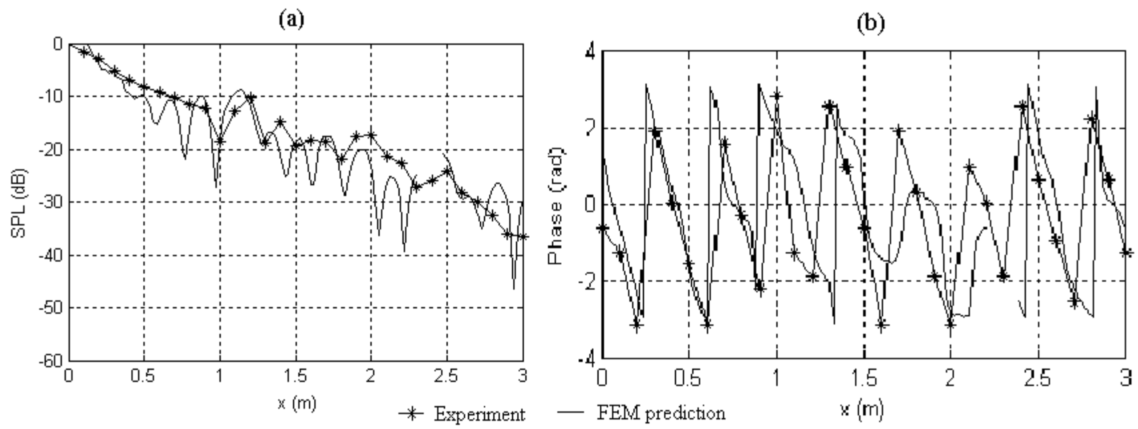

Figure 3.20 Comparison between FEM prediction and experiment for the multi-block case along the central axis: (a) amplitude in decibels and (b) phase in radians.

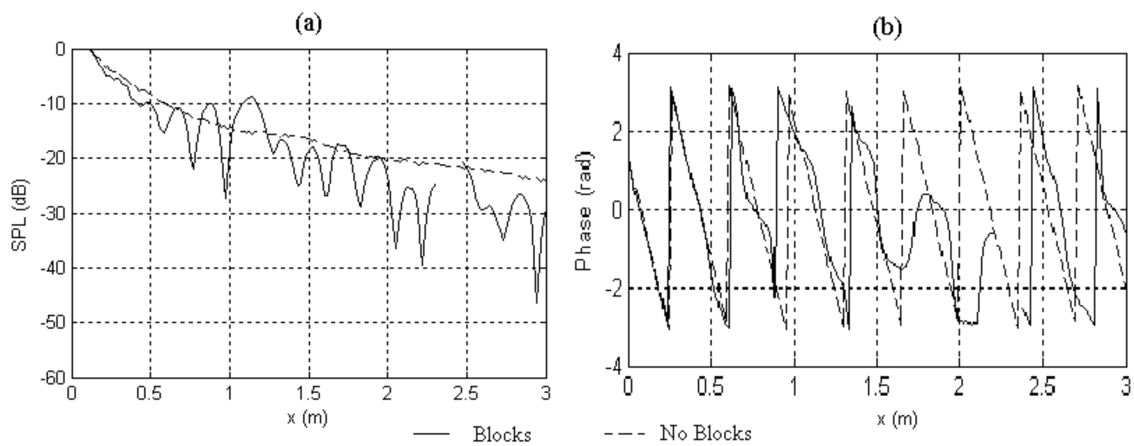

Figure 3.21 FEM prediction for the multi-block case along the central axis: (a) amplitude in decibels and (b) phase in radians.

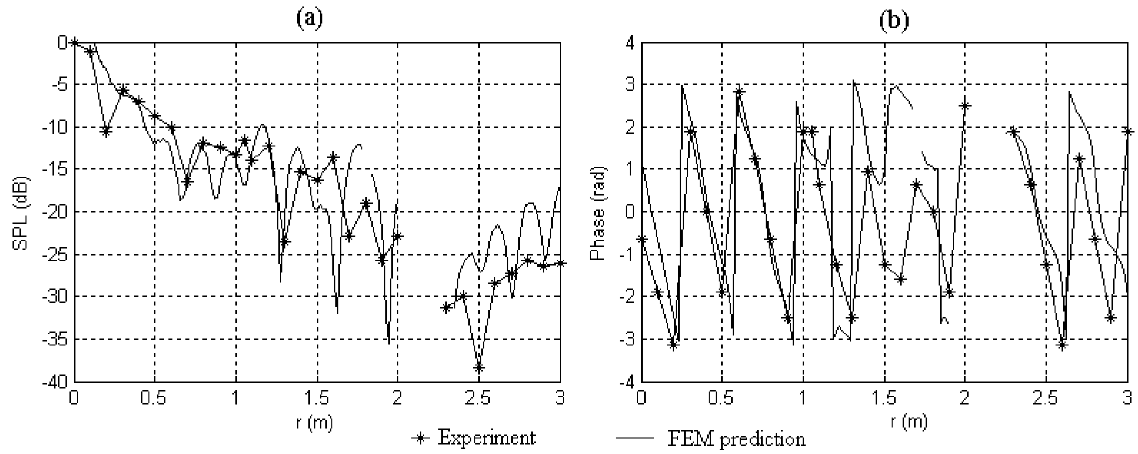

Figure 3.22 Comparison between FEM prediction and experiment for the multi-block case along the $+18^{o}$ direction: (a) amplitude in decibels and (b) phase in radians.

Along the $+18^{o}$ direction, the comparison to experimental data can be seen in Figure 3.22. Note that the gap in the data points indicates the presence of a block. The agreement is better in some places and worse in others, but overall it is satisfactory. FEM predicts higher levels behind the block, at r>2.3 m. In the comparison with free field from Figure 3.23, the phase nonlinearity is seen again in front of a block. Behind the block, phase changes are predicted, but the difference is, surprisingly, in the opposite direction.

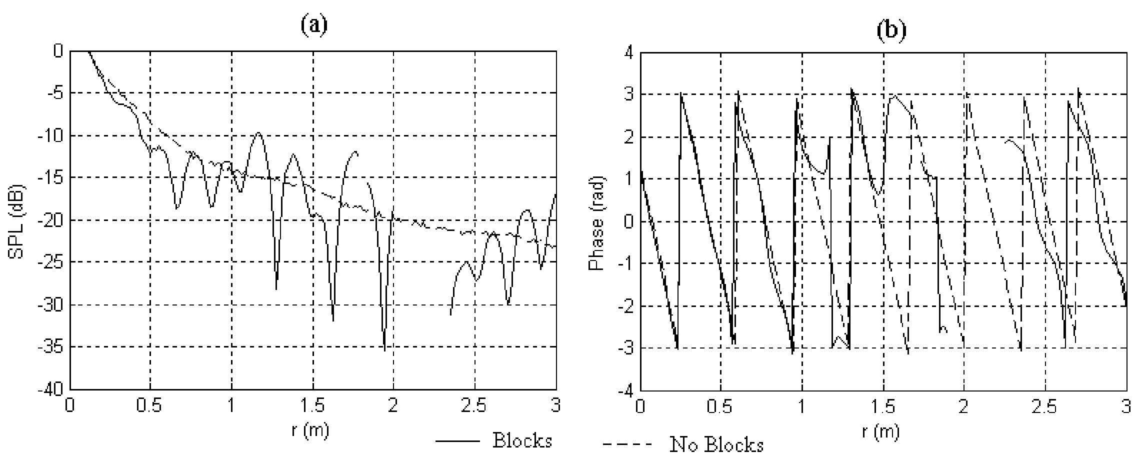

Figure 3.23 FEM prediction for the multi-block case along the $+18^{o}$ direction: (a) amplitude in decibels and (b) phase in radians.

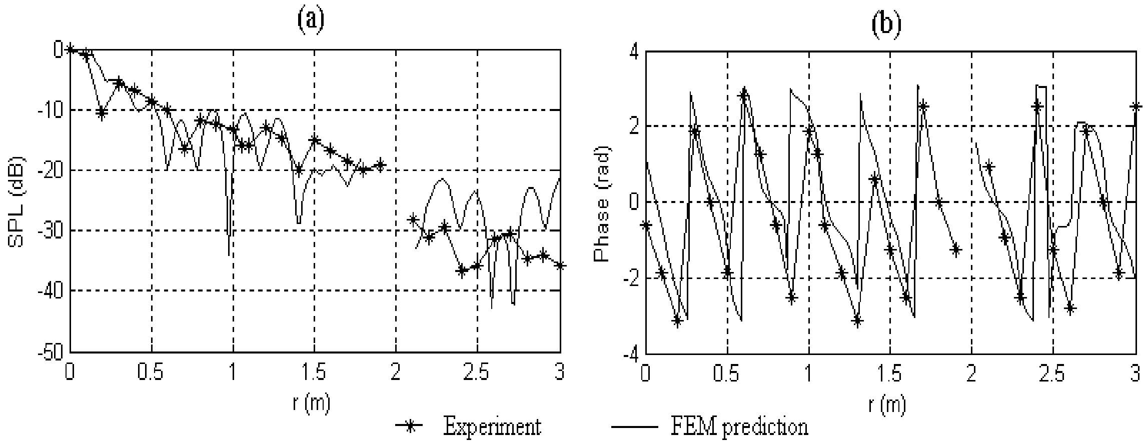

Figure 3.24 Comparison between FEM prediction and experiment for the multi-block case along the -18^o direction: (a) amplitude in decibels and (b) phase in radians.

For the results along the -18^o direction, the FEM predictions are plotted along with experimental data in Figure 3.24. The amplitude data compare well, and FEM again predicts higher levels behind a block. Phase results agree better. For phase changes, Figure 3.25 compares the FEM predictions with the blocks to the free-field case. The phase exhibits some strange behaviour beyond the block at *r*>2.3 m. The phase shift is probably due to diffraction.

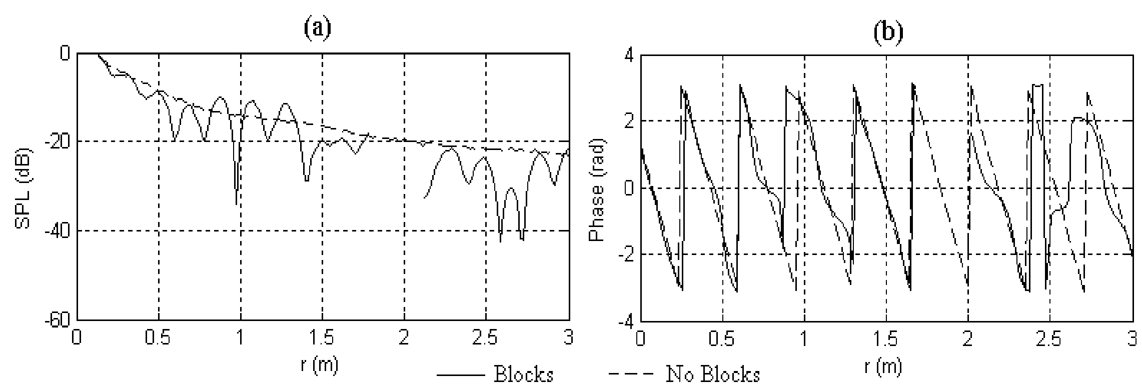

Figure 3.25 FEM prediction for the multi-block case along the -18^o direction: (a) amplitude in decibels and (b) phase in radians.

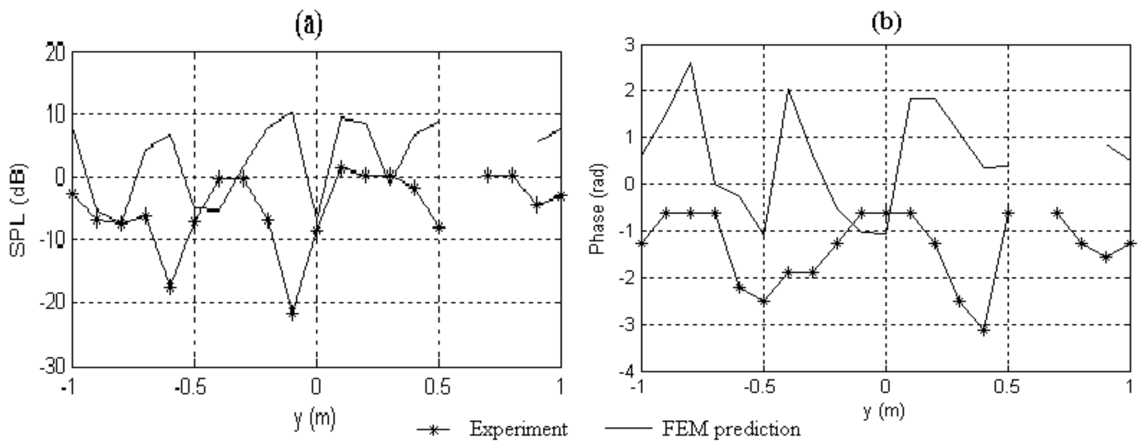

Figure 3.26 Comparison between FEM prediction and experiment for the multi-block case along the $\sqrt{5}$ m arc: (a) amplitude in decibels and (b) phase in radians.

Finally, the results along the $\sqrt{5}$ m arc are shown in Figure 3.26 and 3.27. The agreement with experiment is not good, likely because the block locations and rotations were all approximated in the FEM. The amplitude data show some evidence of similarity, but the phase does not. Phase changes are both above and below the free-field phase. Solid conclusions could not be drawn from this set of measurements.

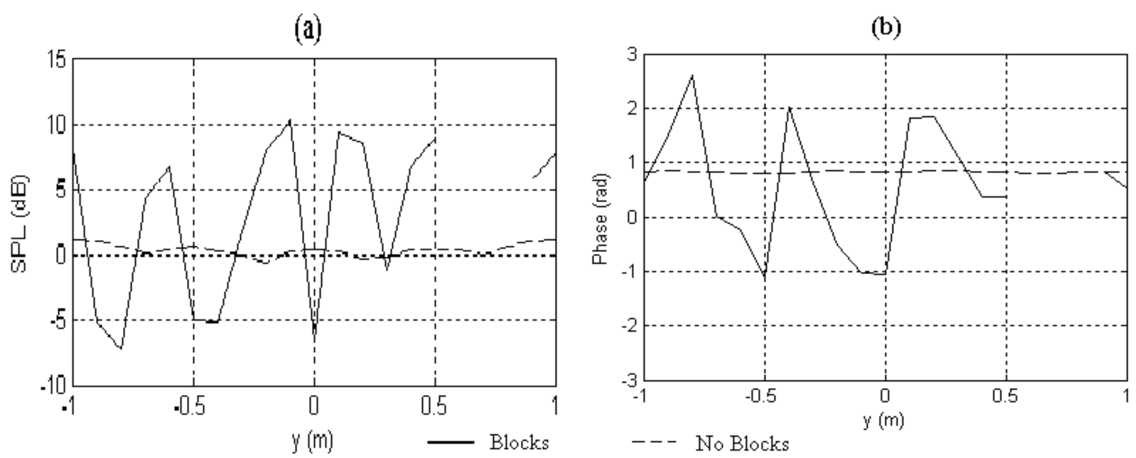

Figure 3.27 FEM prediction for the multi-block case along the $\sqrt{5}$ m arc:
(a) amplitude in decibels and (b) phase in radians.

3.10 Error Analysis

While some of the theoretical inaccuracies were discussed before, the numerical inaccuracy of the prediction results will now be discussed. In ray tracing, there is error associated with the mesh size, number of rays, number of trajectories, and randomness. Optimizing for statistical accuracy with the first three of these parameters was discussed in section 3.2.2. Increasing the number of rays and trajectories, and decreasing the mesh size decreases the prediction error. The error from these parameters can be very significant, depending on their settings. For our settings, we estimate the error to be a few decibels. Increasing the number of rays also decreases the error due to randomness, since the initial direction of the ray from the source is chosen randomly. As an example, refer to the results from Table 3.3. If the source is in the middle of a square room, each quadrant should exhibit symmetrical results. With 300,000 rays, the symmetry is respected to within 1 dB.

There are also errors from modeling that lead to differences between real-life measurements and ray-tracing results. For example, values for the reflection coefficient and source power are approximate, which affects the amount of residual energy added to all receiver cells. This results in an offset of several decibels, which leads to inaccuracies in the absolute sound-pressure levels. However, the proper decay rates are preserved, so the relative magnitude of the sound levels may be more accurate than the absolute values.

3.11 Summary

In Chapter 3, we improved a ray-tracing model to include phase and deterministic diffraction. Several test cases were presented to show the robustness of the algorithm. We then simulated the experimental configurations from Chapter 2 with both the ray-tracing and finite element models. Results were compared between experiment and the two prediction methods, with overall satisfactory agreement. Ray-tracing predictions were inaccurate in front of obstacles in some cases, due to a lack of reflected rays. Behind one edge, the agreement was better. Around two edges, no comparison was made because second-order diffraction was not implemented. Phase changes were predicted in front of objects due to reflection, and in behind objects due to diffraction. The next step, to be taken in the following chapter, is to perform diffraction predictions for non-anechoic boundary conditions – that is, in an actual room.

Chapter 4

Application

4.1 Overview

In the previous chapter, a diffraction algorithm was implemented and tested with several obstacle configurations in a free-field environment. In this chapter, we present ray-tracing predictions of the same obstacles, but this time in non-free-field conditions – in particular, in rooms. The motivation is to determine how phase behaves around diffracting objects in conjunction with wall reflections. Some amount of phase change is expected from interference with reflected waves, depending on their magnitudes. The idea is that, if the phase becomes overly randomized, it becomes difficult to match the phase at any point in space, and the application of active noise control, which relies on this principle for the cancellation of sound, may not be feasible or effective. We complete the chapter with preliminary predictions of active noise control.

4.2 Room Predictions

We begin with an outline of the ray-tracing inputs that were used to perform the room predictions. Most of the parameter settings from the free-field predictions were retained (see section 3.2.2), but the following inputs were changed. The reflection coefficient R of the exterior walls that bound the domain was raised from 0.01 to 0.9, creating a highly reverberant room. An intermediate value of R=0.5 was also studied. The number of trajectories was increased to 20 from 3. A frequency of 1000 Hz was again studied, but a lower frequency of 250 Hz was also investigated. Note that this is of interest since the corresponding wavelength (1.36 m) is larger than the obstacle dimensions. The room geometry, including the relative locations of the source, receiver and the interior surfaces, was not altered. However, different room configurations from in the previous chapters will be presented. Results will be shown first for 1000 Hz, for both reflection coefficients for comparison purposes, followed by 250 Hz. Amplitude results are suppressed, because the focus here is on phase. Note that, with the increased number of trajectories, the runtime lengthened to 1.5-2 hours.

4.2.1 Results at 1000 Hz

The first result is for an empty, reverberant room. In Figure 4.1, the phase of the sound field with R=0.9, R=0.5 and R=0.01 can be compared. Near the walls of the room, the outermost concentric rings show signs of phase shifting. The phase of the anechoic results is less scattered at the corners of the room. As the reflection coefficient decreases from 0.9 to 0.5 to 0.01, the phase becomes progressively less scattered, as expected.

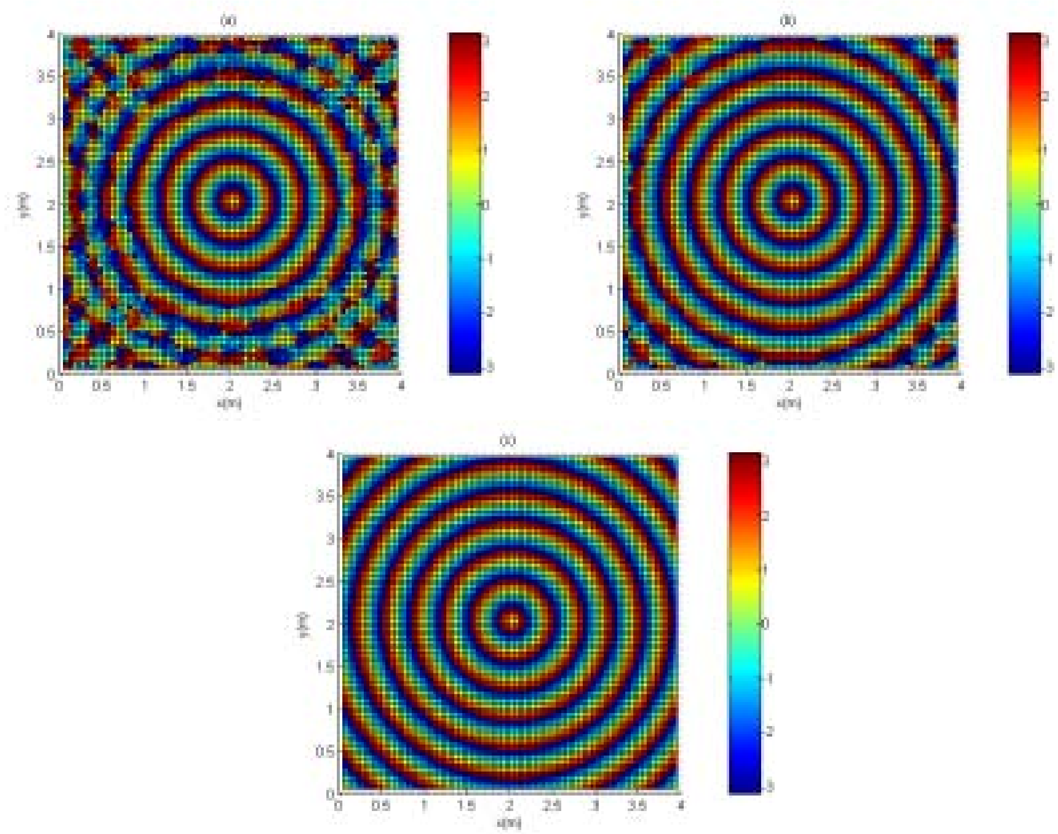

Figure 4.1 Phase in radians of a source in an empty reverberant room;
the source is at (2,2): (a) R=0.9 (b) R=0.5 (c) R=0.01.

Figures 4.2, 4.3 and 4.4, show phase predictions around various configurations of interior walls. In Figure 4.2, a wedge is created from two straight walls, resembling the configuration from Figure 3.7, but with a more prominent shadow zone. For R=0.9, the phase of the sound along the furthest walls from the source is strongly scattered by the reflected waves. The wave fronts are clearly resolved up to 3 m away from the source. In contrast, the phase of the R=0.5 case continues its linear pattern up to the exterior wall. Within the shadow zone, the phase appears more random in the more reflective case. Wave fronts are still identifiable in the shadow zone of the R=0.5 results.

In Figure 4.3, a new configuration is shown, consisting of two hanging straight walls at that form a doorway. Both walls are located at y=2.5 m, and extend 2 m into the room from the outer walls. Hence, there is an opening of 1 m between the walls, and shadow zones exist behind both walls. The wave fronts of the direct sound are visibly propagating through the opening between the two walls and into the shadow zones. As in the previous configuration, the phase of the R=0.9 case seems to be randomly diffused deep in both shadow zones, and in the far corners of the room. In comparison, the phase of the R=0.5 case is still sharply defined in the farthest corner of the direct field, and also in parts of both shadow zones. Interestingly, parts of the wave fronts near the shadow boundary are still identifiable in the R=0.9 case, and they are aligned continuously with the wave fronts of the direct sound.

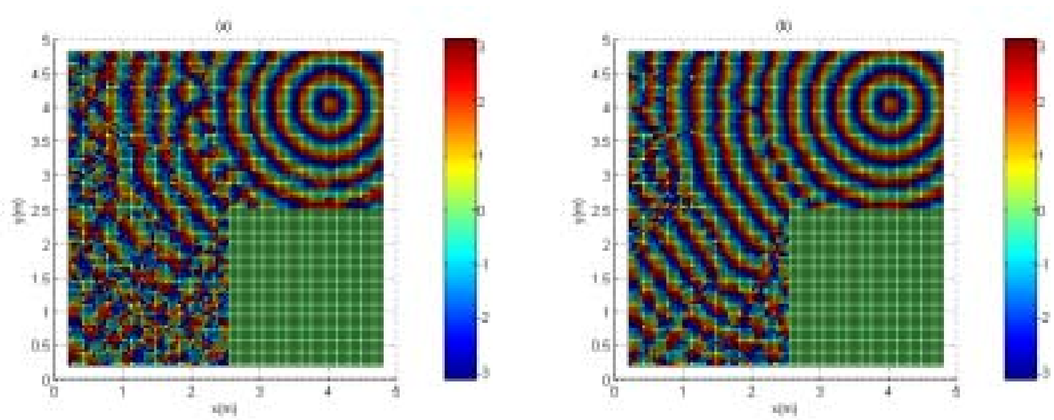

Figure 4.2 Phase in radians of a source in a reverberant room with a wedge; the source is at (4,4): (a) R=0.9 (b) R=0.5.

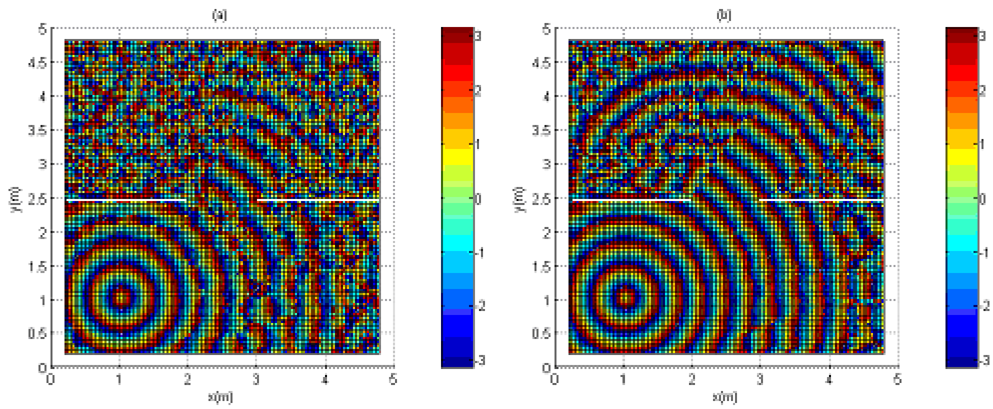

Figure 4.3 Phase in radians of a source in a reverberant room with a doorway; the source is at (1,1): (a) R=0.9 (b) R=0.5.

Finally, in Figure 4.4 a square pillar is placed in the middle the room, similar to the previous block configurations. The shadow zone that could only be illuminated with second-order diffractions is filled in by rays reflecting from the bounding surfaces of the room. This can be seen in the phase plots, as the wave fronts appear V-shaped instead of circular behind the square. This suggests that, when there are many reverberant reflections, second-order diffraction may not be important. Another consequence is that the magnitude (not shown) is reasonably continuous behind the obstacle. Comparing the two reflection coefficients, the same pattern is observed, in that the phase is clearer in the less reverberant room. Notice again that, in all these figures, the physical alignment of the source, diffraction point and shadow zone are different from previously shown results, demonstrating that the diffraction implementation correctly bends rays into the appropriate directions.

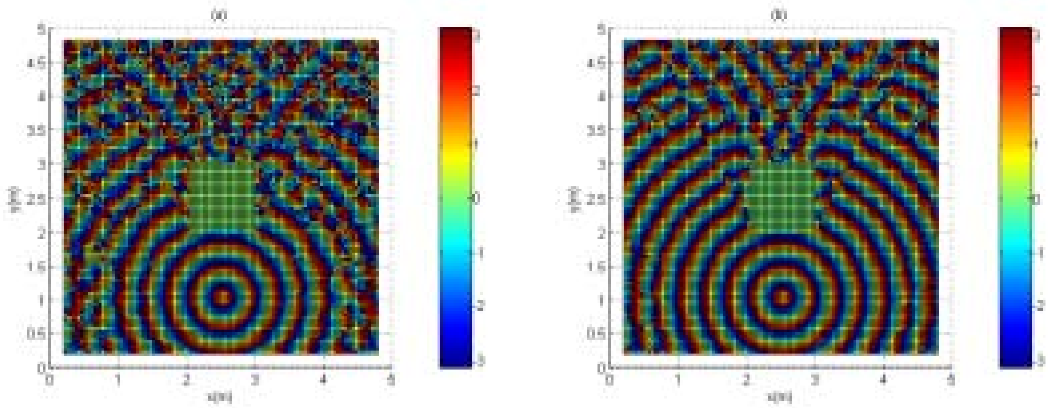

Figure 4.4 Phase in radians of a source in a reverberant room with a square pillar; the source is at (2.5,1): (a) R=0.9 (b) R=0.5.

4.2.2 Results at 250 Hz

At a lower frequency of 250 Hz, the main difference from the 1000 Hz predictions is an increase in the number of diffracted rays. This is because the edge-proximity tolerance of $\lambda/2$ is greater, allowing more rays to satisfy the diffraction conditions. Ray-tracing predictions at 250 Hz for exactly the same room configurations are shown in Figures 4.5, 4.6, 4.7 and 4.8. For the empty, reverberant room in Figure 4.5, the phase contours appear to lose their circular shape and became slightly square, near the reflective room boundaries. As in the 1000-Hz case, there is less scattering when the reflection coefficient of the walls decreases.

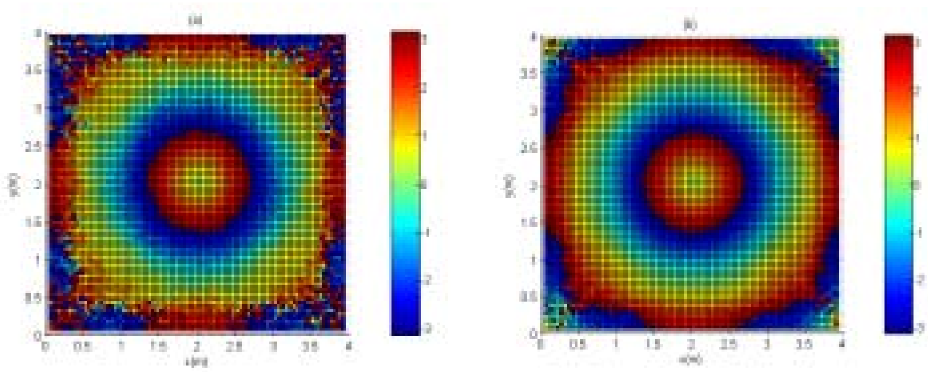

Figure 4.5 Phase in radians of a source in an empty reverberant room at 250 Hz; the source is at (2,2): (a) R=0.9 (b) R=0.5.

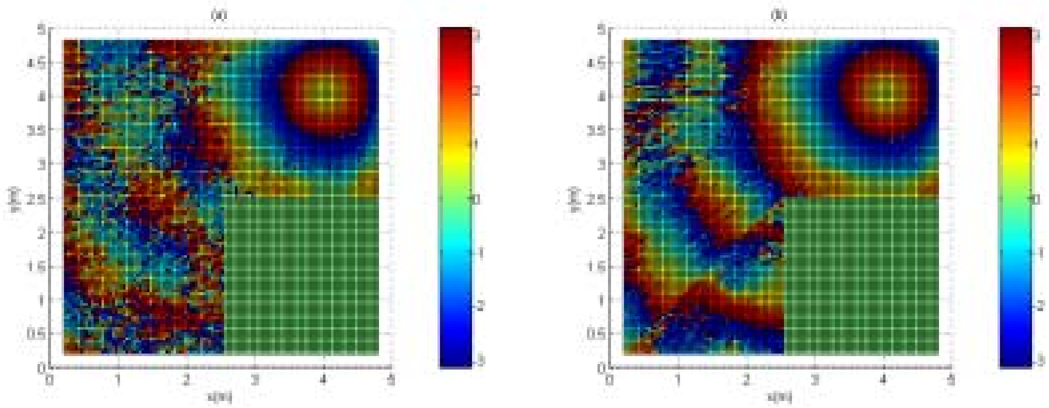

Figure 4.6 Phase in radians of a source in a reverberant room with a corner at 250 Hz; the source is at (4,4): (a) R=0.9 (b) R=0.5.

In Figure 4.6, the presence of a diffracting corner does not scatter the sound as strongly as in the 1000-Hz case. The wave fronts in the shadow zone remain quite distinguishable and circular, even with R=0.9. This result makes sense because more diffraction occurs at a lower frequency, allowing the diffracted rays to better dominate the scattering caused by reflected rays. The results of the doorway configuration in Figure 4.7 reinforce the previous two results. The phase scatters less at the lower frequency, and also for the lower reflection coefficient. The continuity of the wave fronts is not good at the left shadow-zone boundary, but is better at the right shadow-zone boundary.

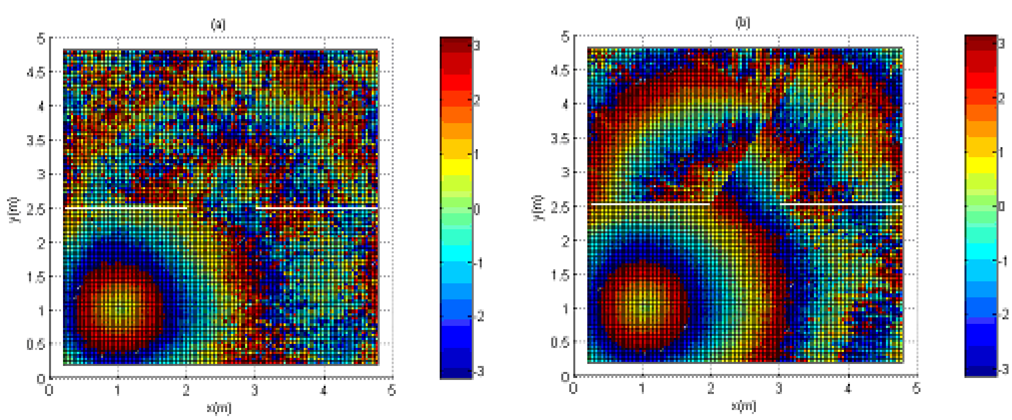

Figure 4.7 Phase in radians of a source in a reverberant room with a doorway at 250 Hz; the source is at (1,1): (a) R=0.9 (b) R=0.5.

In Figure 4.8, the phase around the square pillar has both similarities to and differences from that of the 1000-Hz case. At the boundary between the first-order shadow region and the direct region, the wave fronts at 250 Hz appear V-shaped in the R=0.9 results, but not in the R=0.5 results. Within the shadow region, the phase of both 250-Hz results is circular, while that of the 1000-Hz results is still V-shaped. The explanation for these predictions lies in the relative strengths of the reflected and diffracted rays. Since more diffraction occurs at lower frequency, the diffracted rays dominate the reflected rays within the shadow zone, creating the circular wave fronts. However, when the reflection coefficient of the wall increases, the reflected rays dominate the diffracted rays, causing the V-shaped wave fronts. At 250 Hz, both of these cases are observed but, at 1000 Hz, the reflected rays always dominate. Again, this suggests that for room predictions where the reflection coefficient is high, the prediction of second-order diffraction around obstacles may be unnecessary.

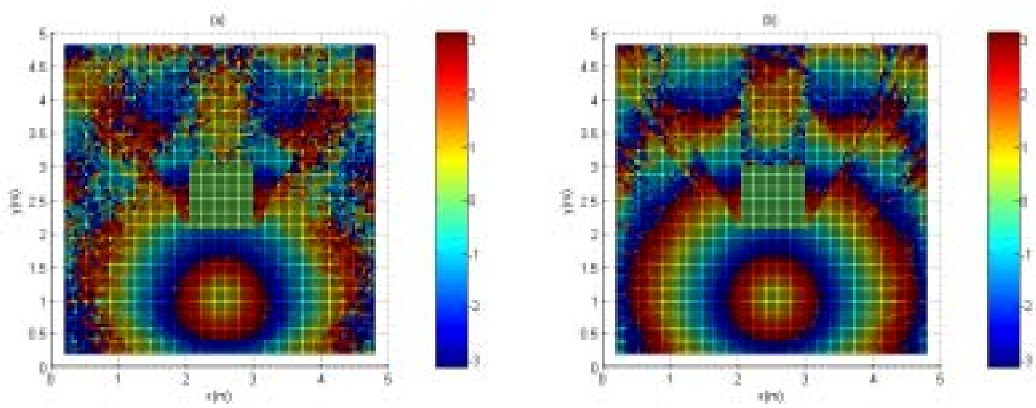

Figure 4.8 Phase in radians of a source in a reverberant room with a square pillar at 250 Hz; the source is at (2.5,1): (a) R=0.9 (b) R=0.5.

We now compare the 1000-Hz and 250-Hz results in the context of active noise control. In theory, active noise control should perform better when the phase of the sound field is better defined. This is because it is easier to match phase to achieve destructive interference when the phase behaves in an orderly fashion. From the room predictions, the phase is always clearest close to the source. Far away from the source, a smaller value of the reflection coefficient produces sharper wave fronts, at both frequencies. Also, the lower frequency seems to generate better defined wave fronts in the shadow zones. In these regions, reflected rays tend to scatter the phase, so the presence of stronger diffracted rays is beneficial. Hence, active noise control should work better at lower frequencies in less reverberant rooms.

4.3 Active Noise Control Prediction

In this section, we used the improved ray-tracing model to predict the effects of active noise control (ANC). ANC predictions have been done in the past using the Image-Phase model [2, 3]. We studied the case of a single-channel ANC system, which consists of two sound sources - one primary noise source and one secondary control source. Only a few adjustments had to be made to the program, because the original code already supported multiple sources, even though the feature was not intended for ANC prediction. The main modification was to address the issue of the sources originally always being in phase; thus, an additional variable, ϕ, was added to account for a phase difference between the sources. The phase difference between the sources was then added to the phase difference due to path length as $\exp[i(kr+\phi)]$, when calculating the SPL at the receiver. We will show results of this implementation, but optimization of the control system will not be included; refer to [2] for a detailed discussion of optimizing the effectiveness of the ANC system. Instead, the noise and control source were simply placed at the same location, with $\phi = \pi$, or a relative 180° phase shift between the source outputs. In theory, this should create global control, resulting in destructive interference and strong sound attenuation over the entire room [3].

4.3.1 Results at 1000 Hz

Figure 4.9 shows the attenuation of SPL achieved by active control, for an empty 4 m by 4 m anechoic room with R=0.01 at 1000 Hz. Note that sound attenuation is defined as the SPL with active control (i.e. with the secondary control source operating) minus the SPL without. This means that a negative value of attenuation is a desirable reduction of SPL, while a positive value of attenuation is an unfavourable increase of SPL. The predicted amplitude in Figure 4.9a shows greatest attenuation close to the source. Far away, there are some regions of sound increase. On average, the attenuation is -8.4 dB. In Figure 4.9b, the resultant phase field due to the two sources shows faint traces of the concentric circles around the source. Interference with the control source appears to randomize the phase. Note that subsequent result figures will not show phase, since the sound attenuation provided by active noise control is the focus here. In Figure 4.10, the reflection coefficient of the walls of the same room is increased to 0.5 and then 0.9. The average attenuation is -6.9 dB for R=0.5, and +3.8 dB for R=0.9. For R=0.5, most of the receiver locations show sound reduction. However, for R=0.9, attenuation is only achieved within 1 m of the source. Beyond that, the control source either has no effect or increases the total sound level. As expected, the effectiveness of the control source increases with decreasing reflection coefficient. Note that runtimes were about one hour in the anechoic case, and about three hours in the non-anechoic cases; the second source doubles the complexity of the algorithm.

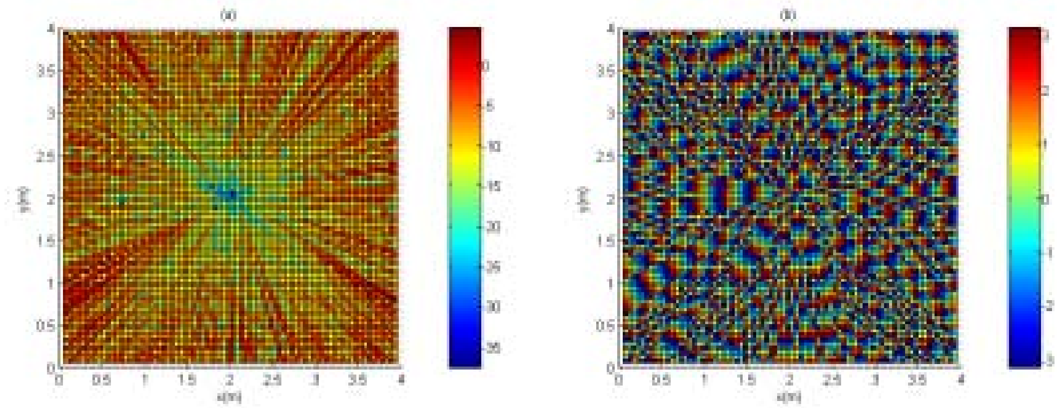

Figure 4.9 Noise-control prediction for an empty anechoic chamber at 1000 Hz; the source is at (2,2): (a) amplitude attenuation in dB, (b) phase in radians.

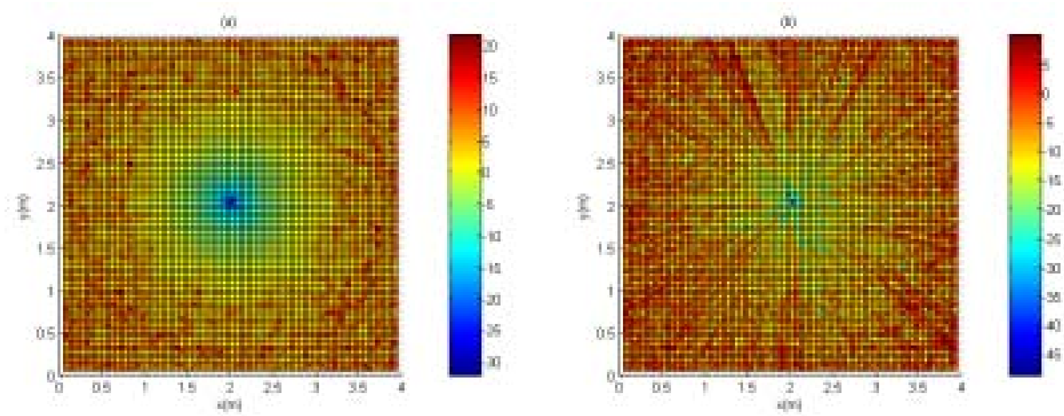

Figure 4.10 Predicted amplitude attenuation in dB for an empty room; the source is at (2,2): (a) *R*=0.9 (b) *R*=0.5.

The next set of predictions, in Figure 4.11, is for a room with the same geometry as for Figure 3.8 - namely, a room with one hanging straight wall. Attenuation is best in regions close to the source. It is worse in some areas within the shadow zone, where sound levels increase. The average attenuation for the entire room is -4.8 dB for *R*=0.01, -3.3 dB for *R*=0.5, and +6.5 dB for *R*=0.9. If the average is calculated within the shadow zone only, the attenuation is -1.4 dB for *R*=0.01, +0.36 dB for *R*=0.5, and +10.6 dB for *R*=0.9. Again, increased surface reflection results in worse sound cancellation. The poor performance in the shadow zone is not surprising because the phase was strongly scattered (see Figure 4.3).

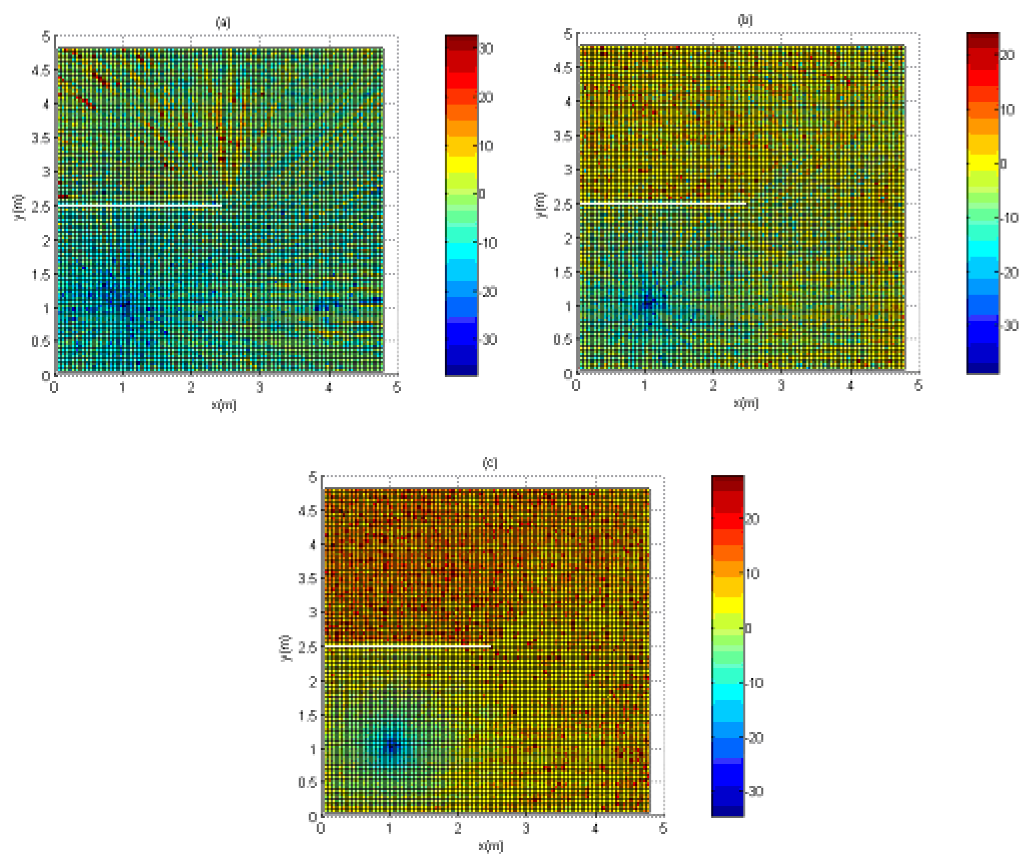

Figure 4.11 Predicted amplitude attenuation in dB for a room with a hanging straight wall; the source is at (1,1): (a) *R*=0.01 (b) *R*=0.5 (c) *R*=0.9.

The last two sets of predictions in Figures 4.12 and 4.13 pertain to a room with fittings (see section 3.6.3). In Figure 4.12, the fittings are random, using the fitting-zone feature of the original ray-tracing model (see Figure 3.14). In Figure 4.13, the fittings are well-defined blocks, as seen in Figure 3.16. Comparing these two cases, we can evaluate the prediction of active noise control with random scattering versus deterministic diffraction. For the random fittings, the average attenuation is +3.5 dB for R=0.01, -1.5 dB for R=0.5, and +10.0 dB for R=0.9. The trend between attenuation and reflection coefficient is not consistent, although the most reverberant case still produces the worst sound attenuation. This may be because of the randomness in the model for fittings, since precise phase matching is required in active noise control.

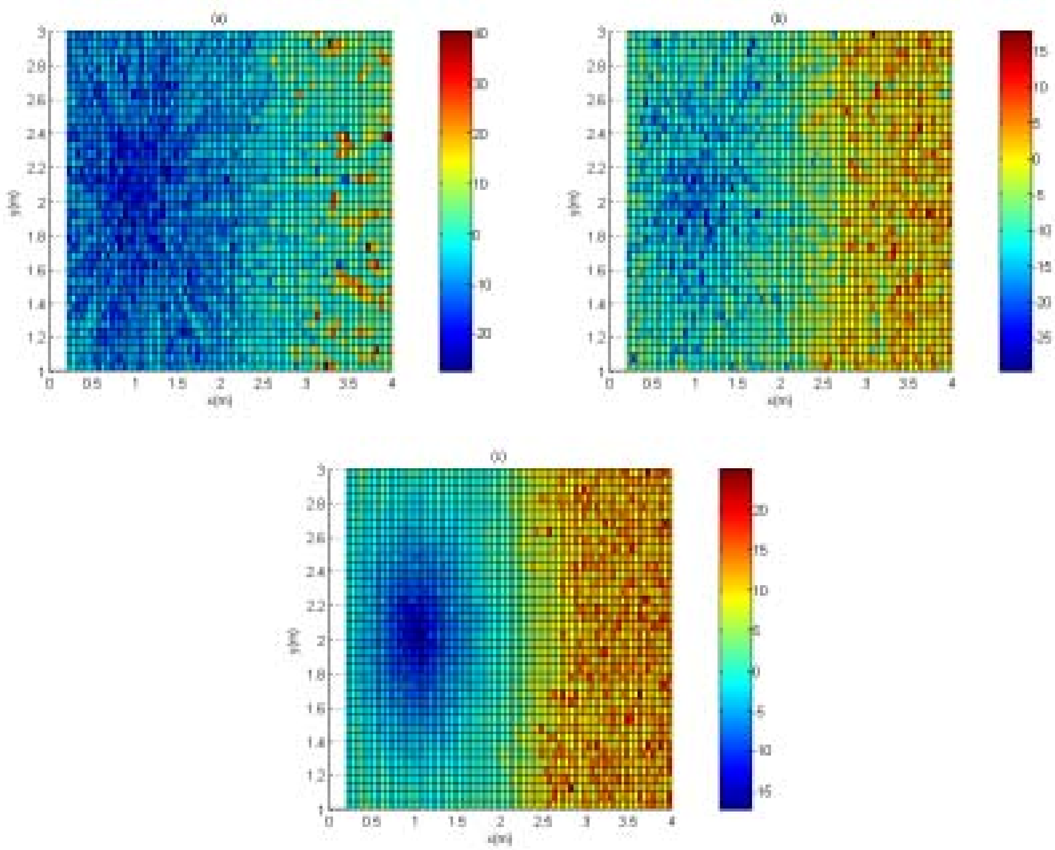

Figure 4.12 Predicted amplitude attenuation in dB for a room with random fittings; the source is at (1,2): (a) R=0.01 (b) R=0.5 (c) R=0.9.

For the non-random fittings with deterministic diffraction, the average attenuation is -3.8 dB for R=0.01, -3.5 dB for R=0.5, and -1.8 dB for R=0.9. The trend of increasing attenuation with decreasing reflection coefficient is again obeyed. Also, attenuation is always achieved, unlike the previous results using random scattering. The difference between the results suggests that the method of modeling diffraction around fittings (i.e. randomly or deterministically) has a significant impact on ANC predictions.

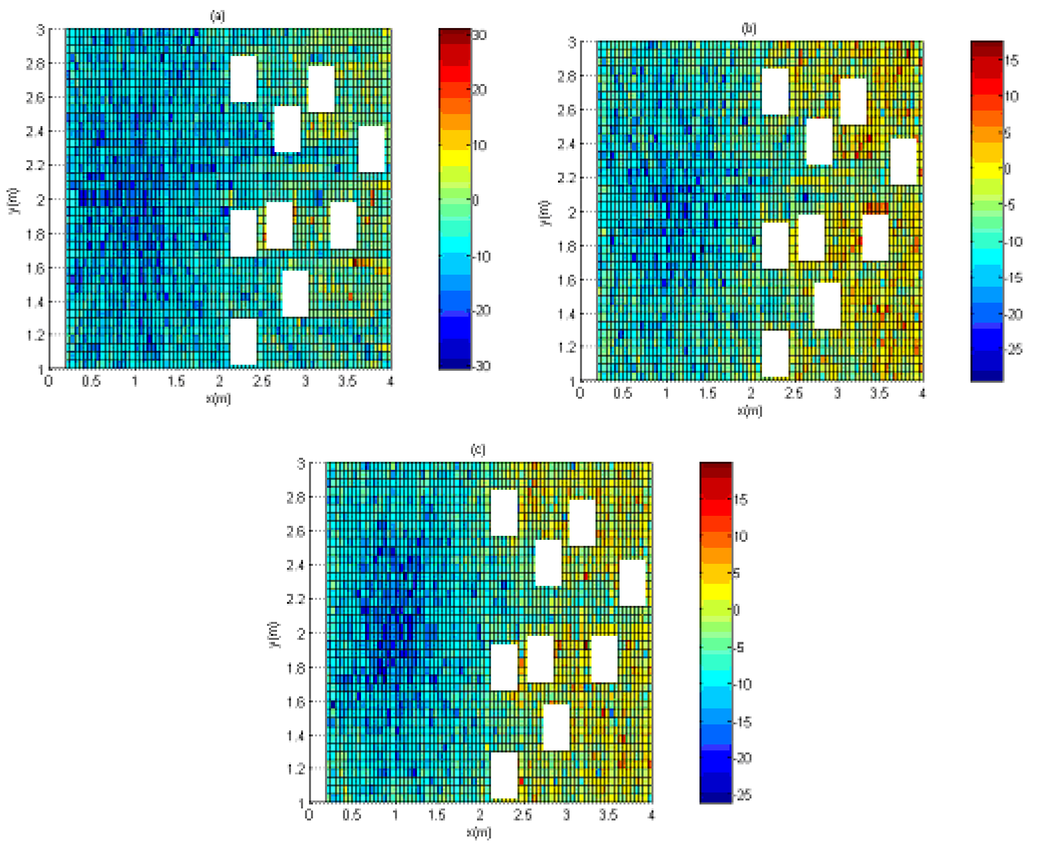

Figure 4.13 Predicted amplitude attenuation in dB for a room with non-random blocks; the source is at (1,2): (a) R=0.01 (b) R=0.5 (c) R=0.9.

4.3.2 Results at 250 Hz

The same room configurations from section 4.3.1 were re-predicted at 250 Hz. Since the frequency is lower, we expect active noise control to perform better. Results for the empty-room case are shown in Figure 4.14 (compare to Figure 4.9 at 1000 Hz). The average attenuation is -8.8 dB for R=0.01, -7.2 dB for R=0.5, and +3.6 dB for R=0.9. These values are all improvements from those at 1000 Hz, but the difference is less than half a decibel. The trend of better sound attenuation with decreasing reflection coefficient is obeyed.

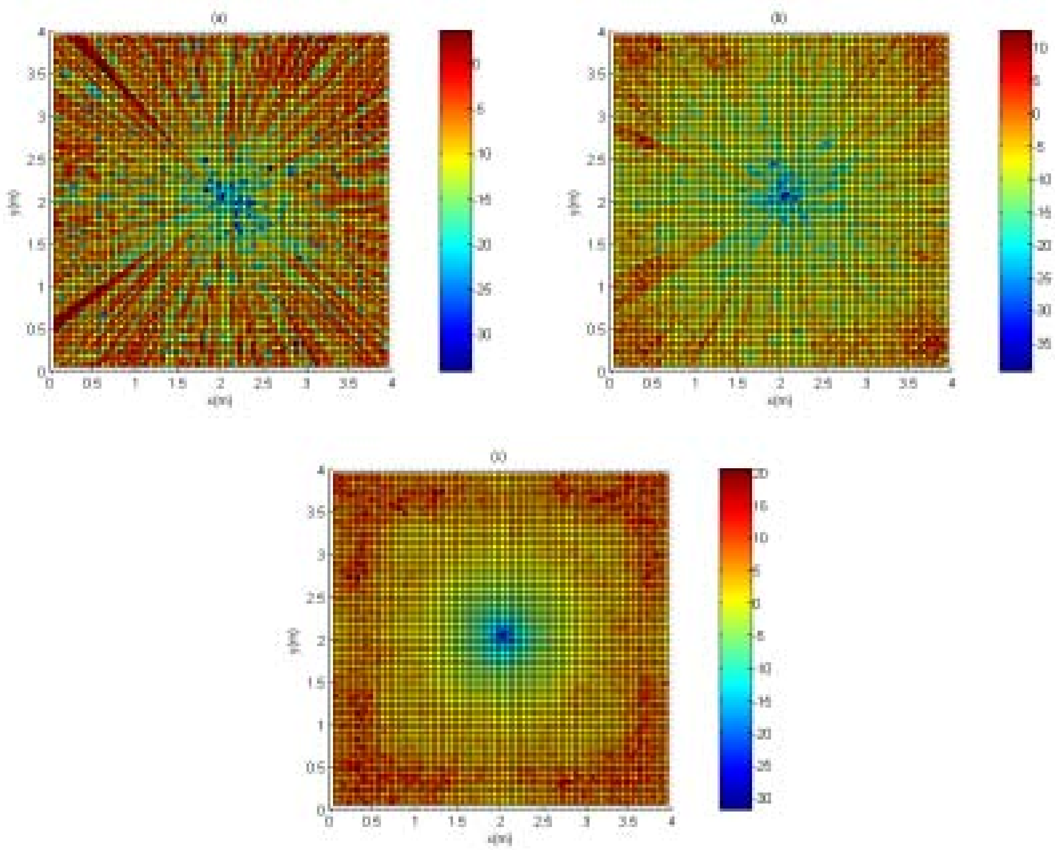

Figure 4.14 Predicted amplitude attenuation in dB for an empty room; the source is at (2,2): (a) R=0.01 (b) R=0.5 (c) R=0.9.

The results for the case of a hanging straight wall are shown in Figure 4.15. The average attenuation is -6.3 dB for *R*=0.01, -3.1 dB for *R*=0.5, and +6.4 dB for *R*=0.9. In the shadow zone, the average attenuation is -5.8 dB for *R*=0.01, -0.8 dB for *R*=0.5, and +10.4 dB for *R*=0.9. As in the empty-room predictions, the 250-Hz results are all better than the 1000-Hz results. This time, sound levels are slightly reduced in the *R*=0.5 case, rather than slightly increased.

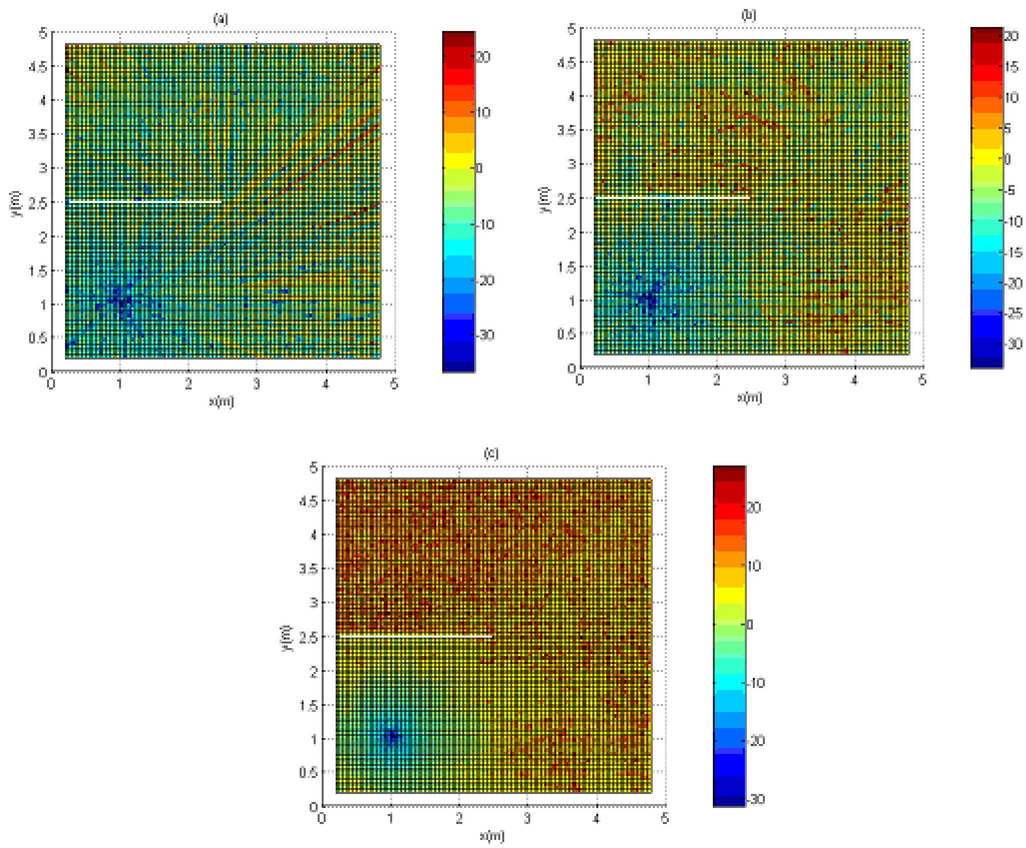

Figure 4.15 Predicted amplitude attenuation in dB for a room with a hanging straight wall; the source is at (1,1): (a) *R*=0.01 (b) *R*=0.5 (c) *R*=0.9.

The prediction results for the room with random scatterers are seen in Figure 4.16. In the fitting zone, the average attenuation is +2.3 dB for R=0.01, -3.1 dB for R=0.5, and +8.7 dB for R=0.9. As before, the 250-Hz attenuations are uniformly better than at 1000 Hz. Interestingly, the sound is reduced most at R=0.5 instead of at R=0.01, as for the 1000-Hz case with random fittings.

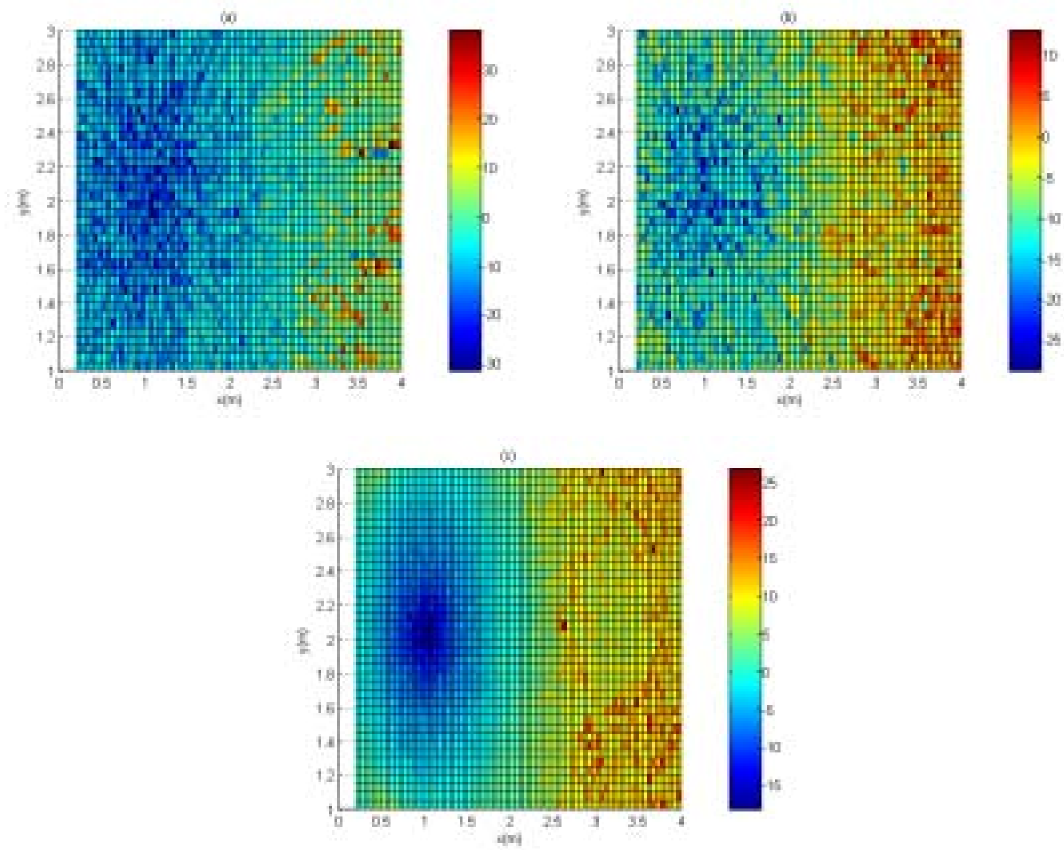

Figure 4.16 Predicted amplitude attenuation in dB for a room with random fittings; the source is at (1,2): (a) R=0.01 (b) R=0.5 (c) R=0.9.

In Figure 4.17, results for ANC prediction in the room with non-random fittings are shown. The average attenuation is -3.5 dB for *R*=0.01, -3.9 dB for *R*=0.5, and -2.0 dB for *R*=0.9. The 250-Hz attenuations are better than those at 1000 Hz except for *R*=0.5, which is surprising. The *R*=0.5 case also achieved more attenuation than *R*=0.01, as predicted when random scatterers were used. There is again a significant difference in the results between the cases of random and non-random fittings; the non-random method predicts greater attenuation. The average sound attenuations of all the above cases are summarized in Table 4.1.

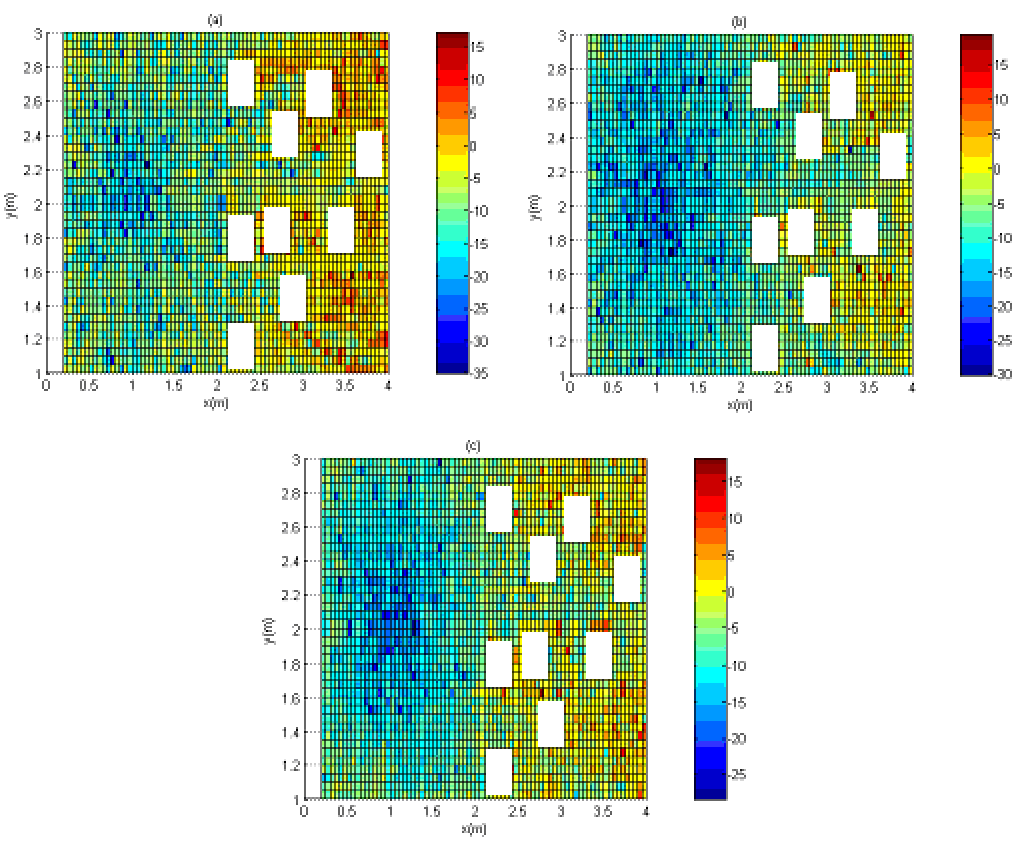

Figure 4.17 Predicted amplitude attenuation in dB for a room with non-random fittings; the source is at (1,2): (a) *R*=0.01 (b) *R*=0.5 (c) *R*=0.9.

Table 4.1 Predicted average sound-level attenuation (dB) obtained with a single-channel active control source in various room configurations.

		Configuration				
f (Hz)	*R*	Empty	Wall	Shadow zone behind wall	Random fittings	Non-random fittings
250	0.01	-8.8	-6.3	-5.8	+2.3	-3.5
250	0.5	-7.2	-3.1	-0.8	-3.1	-3.9
250	0.9	+3.6	+6.4	+10.4	+8.7	-2.0
1000	0.01	-8.4	-4.8	-1.4	+3.5	-3.8
1000	0.5	-6.9	-3.3	+0.36	-1.5	-3.5
1000	0.9	+3.8	+6.5	+10.6	+10.0	-1.8

4.4 Summary

In this chapter, we have applied the improved ray-tracing model to predict sound-pressure levels in rooms with diffracting objects. Two reflection coefficients (0.5 and 0.9) and two frequencies (250 Hz and 1000 Hz) were studied. Predicted phase wave fronts were less scattered at the lower frequency, and with the lower reflection coefficient. The lack of second-order diffraction was less evident in room predictions, because higher-order reflections allow rays to enter shadow zones. The model was also modified to include the secondary source of a single-channel ANC system. Predictions were made to study ANC effectiveness in the same room configurations. Active noise control was expected to perform better in cases with clearer phases, and this was confirmed in the results of ANC predictions. For rooms with multiple fittings, the representation of the fittings – either randomly using a fitting density, or non-randomly using several connected interior surfaces – strongly affects the predicted effectiveness of the ANC. The following chapter concludes the work and summarizes the results.

Chapter 5

Conclusion

5.1 Summary of Accomplishments

The objective of this work was to develop a model that predicts sound-pressure fields in amplitude and phase, in rooms with diffracting obstacles. This is essential for optimizing an active noise control system, so that low-frequency noise in industrial workrooms could be attenuated for the benefit of the room occupants. To achieve this objective, we performed both experiments and predictions to study the behaviour of sound in the presence of diffracting obstacles.

Measurements were performed in an anechoic chamber to study sound diffraction. A diffracting edge, a single block, and a random array of blocks were used to investigate phase changes due to first-order diffraction and multiple obstacles. We found that phase changes occur in front of obstacles, due to interference with reflected waves. Phase changes also occur behind obstacles, due to the larger source-to-receiver distances involved; the path length increased when the direct source-to-receiver path was blocked. Far behind an obstacle, in the shadow zone, phase varied linearly with distance. The fittings also created more peaks and dips in the amplitude results, because of interference effects. The experimental data were verified in comparison with theoretical solutions, and also with predicted results from the finite element model. In general, the agreement was good; the peaks and dips of the amplitude and phase plots occurred at the expected locations.

An existing ray-tracing prediction model was upgraded to include phase and deterministic first-order diffraction. Phase was implemented by considering the total distance traveled by a ray when it arrives at the receiver. Diffraction was implemented by redirecting rays that strike within $\lambda/2$ of an edge into the shadow zone behind the obstacle. The amplitude and phase of a ray are also modified by the diffraction coefficient as per the Uniform Geometric Theory of Diffraction. The ability of the algorithm to handle different types of edges and room geometries was tested extensively. Results for the experimental configurations were satisfactory; phase varied continuously between the direct and shadow zones, and realistic amplitude decay was predicted in the shadow zone. Inaccuracies were associated with the lack of both second-order diffraction and reflections near an edge.

Furthermore, the ray-tracing model was used to predict sound fields in non-anechoic rooms, to investigate the effect of wall reflections with diffraction on phase. We found that the phase became more scattered when the reflection coefficient of the walls increased. Phase was clearest close to the source, and scattered the most near the room boundaries, and within shadow regions. Moreover, lower frequencies have clearer wave fronts. These results imply that active noise control should be more effective for rooms with lower reverberation and lower frequencies of sound. This was verified by modifying the ray-tracing program to predict sound attenuation due to a single secondary control source. Thus a single-channel active control system was simulated, where by an out-of-phase secondary control source was co-located with the primary noise source to be controlled. Attenuation was indeed predicted, with greater effectiveness at a lower frequency and a lower reflection coefficient. This suggests that the ray-tracing model may be a viable tool for optimizing active noise control systems in the future.

5.2 Future Work

Although this work has been successful in predicting sound-pressure levels in shadow zones with phase, there is still room for improvement. Future work with the ray-tracing model could address some of the known problems and suggested changes discussed in the third chapter. Most notably, the implementation of higher-order diffraction, and making the code more efficient and user-friendly, would be welcome changes. On the topic of active noise control in rooms, the ray-tracing model in its current state requires the user to input secondary-source strengths, in magnitude and relative phase. It would be beneficial to combine the ray-tracing algorithm with the algorithm for calculating the strengths of the control sources [30] to automate this step.

Bibliography

[1] G. Wong. Measurement and Prediction of Low-Frequency Noise in Industrial Workrooms. M.A.Sc. Thesis, UBC Department of Mechanical Engineering, 2005.

[2] J. Guo. Active noise control in enclosed spaces. *Canadian Acoustics*, 27 (3), 1999.

[3] D. Li. Optimal active noise control in large rooms using a “locally global” control strategy. *Journal of the Acoustical Society of America*, 118 (6), 2005.

[4] H. Kuttruff. Acoustics, An Introduction. Taylor & Francis Group, New York, 2007.

[5] M. Hodgson. Course notes for Mech 405: Acoustics and Noise Control, University of British Columbia, 2006.

[6] P.M. Morse and K.U. Ingard. Theoretical Acoustics. Princeton University Press, 1968.

[7] R.D. Murch. An evaluation of ray tracing volume source formulation of wave scattering. *Journal of the Acoustical Society of America*, 96 (3), 1994.

[8] O. Falou, J.C. Kumaradas, and M.C. Kolios. Finite element modeling of acoustic wave scattering from fluid, rigid and elastic objects. *Canadian Acoustics*, 33 (3), 2005.

[9] V. Pulkki et al. Efficient representation of edge diffraction impulse responses. *Proceedings of the International Congress on Acoustics*, Madrid, Spain, 2007.

[10] M. A. Biot and I. Tolstoy. Formulation of wave propagation in infinite media by normal coordinates with an application to diffraction. *Journal of the Acoustical Society of America*, 29 (1), 1957.

[11] H. Medwin. Shadowing by finite noise barriers. *Journal of the Acoustical Society of America*, 69 (4), 1981.

[12] P. Svensson and R. Fred. An analytic secondary source model of edge diffraction impulse responses. *Journal of the Acoustical Society of America*, 106 (5), 1999.

[13] T. Kawai. Sound diffraction by a many sided barrier or pillar. *Journal of Sound and Vibration*, 79, 1981.

[14] M. Hodgson. Theoretical and Physical Models as Tools for the Study of Factory Sound Fields. PhD dissertation, *Institute of Sound and Vibration Research*, University of Southampton, 1983.

[15] K. Li and M. Hodgson. Improved methods for estimating fitting density in industrial workrooms. *Journal of Sound and Vibration*, 218, 1998.

[16] V. Valeau, et al. On the use of a diffusion equation for room acoustic prediction. *Journal of the Acoustical Society of America*, 119 (3), 2005.

[17] J. Keller. Geometrical theory of diffraction. *Journal of the Optical Society of America*, 52 (2), 1962.

[18] R. G. Kouyoumjian and P. H. Pathak. A Uniform geometrical theory of diffraction for an edge in a perfectly conducting surface. *Proceedings of the IEEE*, 62 (11), 1974.

[19] N. Tsingos. A Geometrical approach to modeling reflectance functions from diffracting surfaces. *Proceedings of the Eurographics Workshop on Rendering*, Brno, Czech Republic, 2000.

[20] N. Tsingos et al. Geometrical theory of diffraction for modeling acoustics in virtual environments. *SIGGRAPH*, 2001.

[21] V. Pulkki and T. Lokki. Visualization of edge diffraction. *Acoustics Research Letters Online*, 4 (4), 2003.

[22] M. Hodgson. When is diffuse-field theory applicable? *Applied Acoustics*, 49 (3), 1996.

[23] V. Valeau. Personal communication. 2007.

[24] A. M. Ondet and J. L. Barbry. Modeling of sound propagation in fitted workshops using ray tracing. *Journal of the Acoustical Society of America*, 85 (2), 1989.

[25] A. L'Esperance. Hybrid image/energy approach for acoustical prediction in industrial rooms. *Canadian Acoustics*, 28 (3), 2000.

[26] M. Hodgson and R. Orlowski. Acoustic scale modeling of factories, part 1: principles, instrumentation and techniques. *Journal of Sound and Vibration*, 113 (1), 1987.

[27] M. R. Stinson et al. Sound pickup in the presence of diffraction effects. *Canadian Acoustics*, 26 (3), 1998.

[28] U. M. Stephenson and P. Svensson. An improved energetic approach to diffraction based on the uncertainty principle. *Proceedings of the International Congress on Acoustics*, Madrid, Spain, 2007.

[29] M. Boirlaud. Simulations numériques en acoustiques des salles. Rapport de stage, Laboratoire d'Etudes Aérodynamiques, Université de Poitiers, 2007.

[30] J. Guo and J. Pan. Local or global control – the applicable active noise control strategy in enclosed environments. *Proceedings of the International Symposium on Active Control of Sound and Vibration*, Southampton, UK, 2002.